POTENTIAL FLOWS OF VISCOUS AND VISCOELASTIC FLUIDS

Daniel D. Joseph, Toshio Funada and Jing Wang

PREFACE

Potential flows of incompressible fluids are solutions of the Navier-Stokes equations which satisfy Laplace's equations. The Helmholtz decomposition says that every solution of the Navier-Stokes equations can be decomposed into a rotational part and an irrotational part satisfying Laplace's equation. The irrotational part is required to satisfy the boundary conditions; in general, the boundary conditions cannot be satisfied by the rotational velocity and they cannot be satisfied by the irrotational velocity; the rotational and irrotational velocities are both required and they are tightly coupled at the boundary. For example, the no-slip condition for Stokes flow over a sphere cannot be satisfied by the rotational velocity; harmonic functions which satisfy Laplace's equation subject to a Robin boundary condition in which the irrotational normal and tangential velocities enter in equal proportions are required.

The literature which focuses on the computation of layers of vorticity in flows which are elsewhere irrotational describes boundary layer solutions in the Helmholtz decomposed forms. These kind of solutions require small viscosity and, in the case gas liquid flows are said to give rise to weak viscous damping. It is true that viscous effects arising from these layers are weak but the main effects of viscosity in so many of these flows are purely irrotational and they are not weak.

The theory of purely irrotational flows of a viscous fluid is an approximate theory which works well especially in gas-liquid flows of liquids of high viscosity, at low Reynolds numbers. The theory of purely irrotational flows of a viscous fluid can be seen as a very successful competitor to the theory of purely irrotational flows of an inviscid fluid. We have come to regard every solution of free surface problems in an inviscid liquid as an opportunity for problems in an inviscid liquid as an opportunity for a new paper. There are hundreds of such opportunities which are still available.

The theory of irrotational flows of viscous and viscoelastic liquids which is developed here is embedded in a variety of fluid mechanics problems ranging from cavitation, capillary breakup and rupture, Rayleigh-Taylor and Kelvin-Helmholtz instabilities, irrotational Faraday waves on a viscous fluid, flow induced structure of particles in viscous and viscoelastic fluids, boundary layer theory for flow over rigid solids, rising bubbles and other topics. The theory of stability of free surface problems developed here is a great improvement of what was available previously and could be used as supplemental text in courses on hydrodynamic stability.

We have tried to assemble here all the literature bearing on the irrotational flow of viscous liquids. For sure, it is not a large literature but it is likely that despite an honest effort it is probable that we missed some good works.

We are happy to acknowledge the contributions of persons who have helped us. Terrence Liao made very important contributions to our early work on this subject in the early 1990's. More recently, Juan Carlos Padrino joined our group and has made truly outstanding contributions to problems described here. In a sense, Juan Carlos could be considered to be an author of this book and we are lucky that he came along. A subject like this which develops an unconvential point of view is badly in need of friends and critics. We were lucky to find such a friend and critic in Professor G.I. Barenblatt who understands this subject and its importance. We are also grateful to Professor K. Sreenivasan for his encouragement and help in recent years. The National Science Foundatiion has supported our work from the beginning.

We worked day and night on this research; Funada in his day and our night and Joseph and Wang in their day and his night. The whole effort was a great pleasure.

Contents

1

Introduction

The theory of potential flow is a topic in the study of fluid mechanics and is also a topic in mathematics. The mathematical theory treats properties of vector fields generated by gradients of a potential. The curl of a gradient vanishes. The local rotation of a vector field is proportional to its curl so that potential flows do not rotate as they deform. Potential flows are irrotational.

The mathematical theory of potentials goes back to the 18th century (see Kellogg 1929). This elegant theory has given rise to jewels of mathematical analysis, such as the theory of a complex variable. It is a well formed or "mature" theory meaning that the best research results have already been obtained. We are not going to add to the mathematical theory; our contributions are to the fluid mechanics theory focusing on effects of viscosity and viscoelasticity. Two centuries of research have focused exclusively on the motions of inviscid fluids. Among the 131,000,000 hits which come up under "potential flows" on Google search are mathematical studies of potential functions and studies of inviscid fluids. These studies can be extended to viscous fluids at small cost and great profit.

The fluid mechanics theory of potential flow goes back to Euler (1761) (see Truesdell 1954 § 36). The concept of viscosity was not known in Euler's time. The fluids he studied are driven by pressures and not by viscous stresses. The effects of viscous stresses were introduced by Navier (1822) and Stokes (1845). Stokes (1851) considered potential flow of a viscous fluid in an approximate sense but most later authors restrict their attention to "potential flow of an inviscid fluid." All the books on fluid mechanics and all courses in fluid mechanics have chapters on "potential flow of inviscid fluids" and none on the "potential flow of a viscous fluid."

An authoritative and readable exposition of irrotational flow theory and its applications can be found in Chapter 6 of the book on fluid dynamics by Batchelor (1967). He speaks of the role of the theory of flow of an inviscid fluid. He says

In this and the following chapter, various aspects of the flow of a fluid regarded as entirely inviscid (and incompressible) will be considered. The results presented are significant only inasmuch as they represent an approximation to the flow of a real fluid at large Reynolds number, and the limitations of each result must be regarded as important as the result itself.

In this book we consider irrotational flows of a viscous fluid. We are of the opinion that when considering irrotational solutions of the Navier-Stokes equations it is never necessary and typically not useful to put the viscosity to zero. This observation runs counter to the idea frequently expressed that potential flow is a topic which is useful only for inviscid fluids; many people think that the notion of a viscous potential flow is an oxymoron. Incorrect statements like "... irrotational flow implies inviscid flow but not the other way around" can be found in popular textbooks.

Irrotational flows of a viscous fluid scale with the Reynolds number as do rotational solutions of the Navier-Stokes equations generally. The solutions of the Navier-Stokes equations, rotational and irrotational, are thought to become independent of the Reynolds number at large Reynolds numbers. Unlike the theory of irrotational flows of inviscid fluids, the theory of irrotational flow of a viscous fluid can be considered as a description of flow at a finite Reynolds number.

Most of the classical theorems reviewed in Chapter 6 of Batchelor's 1967 book do not require that the fluid be inviscid. These theorems are as true for viscous potential flow as they are for inviscid potential flow. Kelvin's minimum energy theorem holds for the irrotational flow of a viscous fluid. The theory of the acceleration reaction leads to the concept of added mass; it follows from the analysis of unsteady irrotational flow. The theory applies to viscous and inviscid fluids alike.

It can be said that every theorem about potential flow of inviscid incompressible fluids applies equally to

viscous fluids in regions of irrotational flow. Jeffreys (1928) derived an equation (his (20)) which replaces the circulation theorem of classical (inviscid) hydrodynamics. When the fluid is homogeneous, Jeffreys' equation may be written as

$$\frac{\mathrm{d}C}{\mathrm{d}t} = -\frac{\mu}{\rho} \oint \mathrm{curl}\boldsymbol{\omega} \cdot \mathrm{d}\boldsymbol{l},$$ (1.0.1)

where

$$\boldsymbol{\omega} = \mathrm{curl}\boldsymbol{u} \quad \text{and} \quad C(t) = \oint \boldsymbol{u} \cdot \mathrm{d}\boldsymbol{l}$$

is the circulation round a closed material curve drawn in the fluid. This equation shows that

... the initial value of $\mathrm{d}C/\mathrm{d}t$ around a contour in a fluid originally moving irrotationally is zero, whether or not there is a moving solid within the contour. This at once provides an explain of the equality of the circulation about an aeroplane and that about the vortex left behind when it starts; for the circulation about a large contour that has never been cut by the moving solid or its wake remains zero, and therefore the circulations about contours obtained by subdividing it must also add up to zero. It also indicates why the motion is in general nearly irrotational except close to a solid of to fluid that has pass near one.

Saint-Venant (1869) interpreted the result of Lagrange 1781 about the invariance of circulation $\mathrm{d}C/\mathrm{d}t = 0$ to mean that

vorticity cannot be generated in the interior of a viscous incompressible fluid, subject to conservative extraneous force, but is necessarily diffused inward from the boundaries.

The circulation formula (1.0.1) is an important result in the theory of irrotational flows of a viscous fluid. A particle which is initially irrotational will remain irrotational in motions which do not enter into the vortical layers at the boundary.

1.1 Irrotational flow, Laplace's equation

A potential flow is a velocity field $\boldsymbol{u}(\phi)$ given by the gradient of a potential ϕ

$$\boldsymbol{u}(\phi) = \nabla\phi.$$ (1.1.1)

Potential flows have a zero curl

$$\mathrm{curl}\boldsymbol{u} = \mathrm{curl}\nabla\phi = 0.$$ (1.1.2)

Fields that are curl free, satisfying (1.1.2), are called irrotational.

Vector fields satisfying the equation

$$\mathrm{div}\boldsymbol{u} = 0$$ (1.1.3)

are said to be solenoidal. Solenoidal flows which are irrotational are harmonic; the potential satisfies Laplace's equation

$$\mathrm{div}\boldsymbol{u}(\phi) = \mathrm{div}\nabla\phi = \nabla^2\phi = 0.$$ (1.1.4)

The theory of irrotational flow needed in this book is given in many books; for example, Lamb (1932), Milne-Thomson (1960), Batchelor (1967), and Landau and Lifshitz (1987). No-slip cannot be enforced in irrotationoal flow. However, eliminating all the irrotational effects of viscosity by putting $\mu = 0$ to reconcile our desire to satisfy no-slip at the cost of real physics is like throwing out the baby with the bath water. This said, the reader can rely on the book by Batchelor and others for the results we need in our study of irrotational flow of viscous fluids.

1.2 Continuity equation, incompressible fluids, isochoric flow

The equation governing the evolution of the density ρ

$$\frac{d\rho}{dt} + \rho \text{div}\boldsymbol{u} = 0, \tag{1.2.1}$$

$$\frac{d\rho}{dt} = \frac{\partial \rho}{\partial t} + (\boldsymbol{u} \cdot \nabla)\rho$$

is called the continuity equation. It guarantees that the mass of a fluid element is conserved.

If the fluid is incompressible, then ρ is constant, and $\text{div}\boldsymbol{u} = 0$. Flows of compressible fluids for which $\text{div}\boldsymbol{u} = 0$ are called isochoric. Low Mach number flows are nearly isochoric. Incompressible and isochoric flows are solenoidal.

1.3 Euler's equations

Euler's equations of motion

$$\rho \frac{d\boldsymbol{u}}{dt} = -\nabla p + \rho \boldsymbol{g}, \tag{1.3.1}$$

$$\frac{d\boldsymbol{u}}{dt} = \frac{\partial \boldsymbol{u}}{\partial t} + (\boldsymbol{u} \cdot \nabla)\boldsymbol{u}$$

where $\boldsymbol{g}$ is a body force per unit mass. If ρ is constant and $\boldsymbol{g} = \nabla G$ has a force potential, then

$$-\nabla p + \rho \boldsymbol{g} = -\nabla \hat{p} \tag{1.3.2}$$

where $\hat{p} = p - \rho G$ can be called the pressure head. If $\boldsymbol{g}$ is gravity, then

$$G = \boldsymbol{g} \cdot \boldsymbol{x}.$$

To simplify the writing of equations we will put the body force to zero except in cases where it is important. If the fluid is compressible, then an additional relation, from thermodynamics, relating p to ρ will be required. Such a relation can be found for isentropic flow, or isothermal flow of a perfect gas. In such a system there are five unknowns p, ρ and $\boldsymbol{u}$ and five equations.

The effects of viscosity are absent in Euler's equations of motion. The effects of viscous stresses are absent in Euler's theory; the flows are driven by pressure. The Navier-Stokes equations reduce to Euler's equations when the fluid is inviscid.

1.4 Generation of vorticity in fluids governed by Euler's equations

The Euler equation (1.3.1) may be written as

$$\frac{\partial \boldsymbol{u}}{\partial t} - \boldsymbol{u} \times \boldsymbol{\omega} + \frac{1}{2}\nabla |\boldsymbol{u}|^2 = \boldsymbol{g} - \frac{\nabla p}{\rho} \tag{1.4.1}$$

where we have used the vector identity

$$(\boldsymbol{u} \cdot \nabla)\boldsymbol{u} = \frac{1}{2}\nabla |\boldsymbol{u}|^2 - \boldsymbol{u} \times \boldsymbol{\omega} \tag{1.4.2}$$

and

$$\boldsymbol{\omega} = \boldsymbol{\omega}[\boldsymbol{u}] = \text{curl}\boldsymbol{u}.$$

The vorticity equation can be obtained by forming the curl of (1.4.1)

$$\frac{\partial \boldsymbol{\omega}}{\partial t} + \boldsymbol{u} \cdot \nabla \boldsymbol{\omega} = \boldsymbol{\omega} \cdot \nabla \boldsymbol{u} - \text{curl}\frac{\nabla p}{\rho} + \text{curl}\boldsymbol{g}. \tag{1.4.3}$$

If $\text{curl}\dfrac{\nabla p}{\rho} = \nabla \times \left(\dfrac{1}{\rho}p'(\rho)\nabla\rho\right) = 0$ and $\text{curl}\boldsymbol{g} = 0$, then $\boldsymbol{\omega}[\boldsymbol{u}] = 0$; $\text{curl}\boldsymbol{g} = 0$ if $\boldsymbol{g}$ is given by a potential $\boldsymbol{g} = \nabla G$. Flows for which $\text{curl}\dfrac{\nabla p}{\rho} = 0$ are said to be barotropic. Barotropic flows governed by Euler's equation with conservative body forces $\boldsymbol{g} = \nabla G$, cannot generate vorticity. If the fluid is incompressible, then the flow is barotropic.

1.5 Perfect fluids, irrotational flow

Inviscid fluids which are also incompressible are called "perfect" or "ideal." Perfect fluids satisfy Euler's equations. Perfect fluids with conservative body forces give rise to a Bernoulli equation

$$\nabla \left\{ \rho \left[\frac{\partial \phi}{\partial t} + \frac{1}{2} |\nabla \phi|^2 \right] + p - G \right\} = 0$$

$$\rho \left[\frac{\partial \phi}{\partial t} + \frac{1}{2} |\nabla \phi|^2 \right] + p - G = f(t).$$

$$(1.5.1)$$

We may absorb the function $f(t)$ into the potential $\hat{\phi} = \phi + \int^t f(t) \, \mathrm{d}t$ without changing the velocity

$$\nabla \hat{\phi} = \nabla \left[\phi + \int^t f(t) \, \mathrm{d}t \right] = \nabla \phi = \boldsymbol{u}.$$

$$(1.5.2)$$

The Bernoulli equation relates p and ϕ before any problem is solved; actually curl$\boldsymbol{u} = 0$ is a constraint on solutions. The velocity $\boldsymbol{u}$ is determined by ϕ satisfying $\nabla^2 \phi = 0$ and the boundary conditions.

1.6 Boundary conditions for irrotational flow

Irrotational flows have a potential and if the flow is solenoidal the potential ϕ is harmonic, $\nabla^2 \phi = 0$. This book reveals the essential role of harmonic functions in the flow of incompressible viscous and viscoelastic fluids. All the books on partial differential equations have sections devoted to the mathematical analysis of Laplace equations. Laplace's equation may be solved for prescribed data on the boundary of the flow region including infinity for flows on unbounded domains. It can be solved for Dirichlet data in which values of ϕ are prescribed on the boundary or for Neuman data in which the normal component of $\nabla \phi$ is prescribed on the boundary. Almost any combination of Dirichlet and Neuman data all over the boundary will lead to unique solutions of Laplace's equation.

It is important that unique solutions can be obtained when only one condition is required for ϕ at each point on the boundary. The problem is over determined when two conditions are prescribed. We can solve the problem when Dirichlet conditions are prescribed or when Neuman conditions are prescribed but not when both are prescribed. In the case in which Neuman conditions are prescribed over the whole the boundary the solution is unique up to the addition of any constant. If the boundary condition is not specified at each point on the boundary, then the problem may be not over-determined when two conditions are prescribed.

This point can be forcefully made in the frame of fluid dynamics. Consider, for example, the irrotational streaming flow over a body. The velocity $\boldsymbol{U}$ at infinity in the direction $\boldsymbol{x}$ is given by the potential $\phi = \boldsymbol{U} \cdot \boldsymbol{x}$. The tangential component of velocity on the boundary S of the body is given by

$$u_S = \boldsymbol{e}_S \cdot \boldsymbol{u} = \boldsymbol{e}_S \cdot \nabla \phi \qquad (1.6.1)$$

where $\boldsymbol{e}_S$ is a unit lying entirely in S. The normal component of velocity on S is given by

$$u_n = \boldsymbol{n} \cdot \boldsymbol{u} = \boldsymbol{n} \cdot \nabla \phi \qquad (1.6.2)$$

where $\boldsymbol{n}$ is the unit normal pointing from body to fluid.

Laplace's equation for streaming flow can be solved if

$$\boldsymbol{e}_S \cdot \nabla \phi \quad \text{is prescribed on } S,$$

say,

$$\boldsymbol{e}_S \cdot \nabla \phi = 0 \quad \text{on } S \qquad (1.6.3)$$

or if

$$\boldsymbol{n} \cdot \nabla \phi \quad \text{is prescribed on } S,$$

say,

$$\boldsymbol{n} \cdot \nabla \phi = 0 \quad \text{on } S. \qquad (1.6.4)$$

It cannot be solved if $\boldsymbol{e}_S \cdot \nabla \phi = 0$ and $\boldsymbol{n} \cdot \nabla \phi = 0$ are simultaneously required on S.
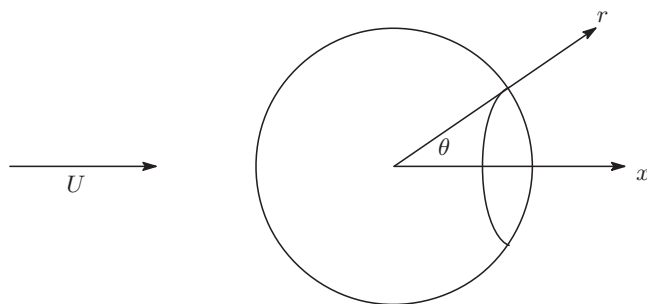
Fig. 1.1. Axisymmetric flow over a sphere of radius a. The flow depends on the radius r and the polar angle θ.

The prescription of the tangential velocity on S is a Dirichlet condition. If ϕ is prescribed on S the tangential derivatives can be computed, only one prescription of the tangential velocity is allowed because prescribing two independent tangential derivatives is not compatible with one ϕ.

The no-slip condition of viscous fluid mechanics requires that

$$u_S = 0 \text{ and } u_n = 0. \tag{1.6.5}$$

simultaneously on S. This condition cannot be satisfied by potential flow. In fact, these conditions cannot be satisfied by solutions of Euler's equations even when they are not irrotational.

The point of view which has been universally adopted by researchers and students of fluid mechanics for several centuries is that the normal component should be enforced so that the fluid does not penetrate the solid. The fluid must then slip at the boundary because there is no other choice. To reconcile this with no-slip, researchers put the viscosity to zero. The resolution of these difficulties lies in the fact that real flows have a non zero rotational velocity at boundaries generated by the no-slip condition. The no-slip condition usually cannot be satisfied by the rotational velocity alone; the irrotational velocity is also needed (see Chapter 4).

1.7 Streaming irrotational flow over a stationary sphere

A flow of speed U in the direction $x = r\cos\theta$ streams past a sphere of radius a (see figure 1.1). A solution ϕ of Laplace's equation $\nabla^2 \phi = 0$ in spherical polar coordinates is

$$\phi = Ur\cos\theta + \frac{c}{r^2}\cos\theta. \tag{1.7.1}$$

The normal and tangential components of the velocity at $r = a$ are, respectively

$$\frac{\partial \phi}{\partial r} = U\cos\theta - \frac{2c}{a^3}\cos\theta, \tag{1.7.2}$$

$$\frac{1}{a}\frac{\partial \phi}{\partial \theta} = -U\sin\theta - \frac{c}{a^3}\sin\theta. \tag{1.7.3}$$

If the normal velocity is prescribed to be zero on the sphere, then $c = Ua^3/2$ and

$$\phi_1 = U\left(r + \frac{a^3}{2r^2}\right)\cos\theta. \tag{1.7.4}$$

The corresponding tangential velocity is $-3U\sin\theta/2$. If the tangential velocity is prescribed to be zero on the sphere, then $c = -Ua^3$ and

$$\phi_2 = U\left(r - \frac{a^3}{r^2}\right)\cos\theta. \tag{1.7.5}$$

The corresponding normal velocity is $3U\cos\theta$.

The preceding analysis and uniqueness of solutions of Laplace's equation shows that the solution ϕ_1 with a zero normal velocity may be obtained by prescribing the non zero function $-\frac{3}{2}U\sin\theta$ for the tangential velocity. The solution ϕ_2 with a zero tangential velocity may be obtained by prescribing the non zero function $3U\cos\theta$ for the normal velocity.

More complicated conditions for harmonic solutions on rigid bodies are encountered in exact solutions of the

Navier-Stokes equations in which irrotational and rotational flows are tightly coupled at the boundary. The boundary conditions cannot be satisfied without irrotational flow and they cannot be satisfied by irrotational flow only (cf. equation (4.6.6)).

2
Historical notes

Potential flows of viscous fluids are an unconventional topic with a niche history assembled in a recent review article Joseph 2006.

2.1 Navier-Stokes equations

The history of Navier-Stokes equations begins with the 1822 memoir of Navier who derived equations for homogeneous incompressible fluids from a molecular argument. Using similar arguments, Poisson (1829) derived the equations for a compressible fluid. The continuum derivation of the Navier-Stokes equation is due to Saint Venant (1843) and Stokes (1845). In his (1847) paper Stokes wrote that

Let P_1, P_2, P_3 be the three normal, and T_1, T_2, T_3 the three tangential pressures in the direction of three rectangular planes parallel to the co-ordinate planes, and let D be the symbol of differentiation with respect to t when the particle and not the point of space remains the same. Then the general equations applicable to a heterogeneous fluid (the equations (10) of my former (1845) paper), are

$$\rho\left(\frac{\mathrm{D}u}{\mathrm{D}t} - X\right) + \frac{\mathrm{d}P_1}{\mathrm{d}x} + \frac{\mathrm{d}T_3}{\mathrm{d}y} + \frac{\mathrm{d}T_2}{\mathrm{d}z} = 0, \tag{132}$$

with the two other equations which may be written down from symmetry. The pressures P_1, T_1, etc. are given by the equations

$$P_1 = p - 2\mu\left(\frac{\mathrm{d}u}{\mathrm{d}x} - \delta\right), \quad T_1 = -\mu\left(\frac{\mathrm{d}v}{\mathrm{d}z} + \frac{\mathrm{d}w}{\mathrm{d}y}\right), \tag{133}$$

and four other similar equations. In these equations

$$3\delta = \frac{\mathrm{d}u}{\mathrm{d}x} + \frac{\mathrm{d}v}{\mathrm{d}y} + \frac{\mathrm{d}w}{\mathrm{d}z}. \tag{134}$$

The equations written by Stokes in his 1845 paper are the same ones we use today:

$$\rho\left(\frac{\mathrm{d}\boldsymbol{u}}{\mathrm{d}t} - \boldsymbol{X}\right) = \mathrm{div}\mathbf{T}, \tag{2.1.1}$$

where X is presumably a body force, which was not specified by Stokes, and

$$\mathbf{T} = \left(-p - \frac{2}{3}\mu\,\mathrm{div}\boldsymbol{u}\right)\mathbf{1} + 2\mu\mathbf{D}[\boldsymbol{u}], \tag{2.1.2}$$

$$\frac{\mathrm{d}\boldsymbol{u}}{\mathrm{d}t} = \frac{\partial\boldsymbol{u}}{\partial t} + (\boldsymbol{u}\cdot\nabla)\,\boldsymbol{u}, \tag{2.1.3}$$

$$\mathbf{D}[\boldsymbol{u}] = \frac{1}{2}\left[\nabla\boldsymbol{u} + \nabla\boldsymbol{u}^T\right], \tag{2.1.4}$$

$$\frac{\mathrm{d}\rho}{\mathrm{d}t} + \rho\,\mathrm{div}\boldsymbol{u} = 0. \tag{2.1.5}$$

Stokes assumed that the bulk viscosity $-\frac{2}{3}\mu\,\mathrm{div}\boldsymbol{u}$ is selected so that the deviatoric part of $\mathbf{T}$ vanishes and trace$\mathbf{T} = -3p$.

Inviscid fluids are fluids with zero viscosity. Viscous effects on the motion of fluids were not understood before the notion of viscosity was introduced by Navier in 1822. Perfect fluids, following the usage of Stokes

and other 19th century English mathematicians, are inviscid fluids which are also incompressible. Statements like Truesdell's 1954,

In 1781 Lagrange presented his celebrated velocity-potential theorem: if a velocity potential exists at one time in a motion of an inviscid incompressible fluid, subject to conservative extraneous force, it exists at all past and future times.

though perfectly correct, could not have been asserted by Lagrange, since the concept of an inviscid fluid was not available in 1781.

2.2 Stokes theory of potential flow of viscous fluid

The theory of potential flow of a viscous fluid was introduced by Stokes in 1851. All of his work on this topic is framed in terms of the effects of viscosity on the attenuation of small amplitude waves on a liquid-gas surface. Everything he said about this problem is cited below. The problem treated by Stokes was solved exactly,using the linearized Navier-Stokes equations, without assuming potential flow, by Lamb 1932.

Stokes discussion is divided into three parts discussed in §51, 52, 53.

(1) The dissipation method in which the decay of the energy of the wave is computed from the viscous dissipation integral where the dissipation is evaluated on potential flow (§51).

(2) The observation that potential flows satisfy the Navier-Stokes equations together with the notion that certain viscous stresses must be applied at the gas-liquid surface to maintain the wave in permanent form (§52).

(3) The observation that if the viscous stresses required to maintain the irrotational motion are relaxed, the work of those stresses is supplied at the expense of the energy of the irrotational flow (§53).

Lighthill 1978 discussed Stokes' ideas but he did not contribute more to the theory of irrotational motions of a viscous fluid. On page 234 he notes that

"Stokes ingenious idea was to recognize that the average value of the rate of working given by sinusoidal waves of wave number

$$2\mu \left[(\partial\phi/\partial x) \, \partial^2\phi/\partial x\partial z + (\partial\phi/\partial z) \, \partial^2\phi/\partial z^2 \right]_{z=0}$$

which is required to maintain the unattenuated irrotational motions of sinusoidal waves must exactly balance the rate at which the same waves when propagating freely would lose energy by internal dissipation."

Lamb 1932 gave an exact solution of the problem considered by Stokes in which vorticity and boundary layers are not neglected. Wang-Joseph 2006 (JFM 557, 145-165) did purely irrotational theories of Stokes problem which are in good agreement with Lamb's exact solution.

2.3 The dissipation method

51. By means of the expression given in Art. 49, for the loss of *vis viva* due to internal friction, we may readily obtain a very approximate solution of the problem: To determine the rate at which the motion subsides, in consequence of internal friction, in the case of a series of oscillatory waves propagated along the surface of a liquid. Let the vertical plane of xy be parallel to the plane of motion, and let y be measured vertically downwards from the mean surface; and for simplicity's sake suppose the depth of the fluid very great compared with the length of a wave, and the motion so small that the square of the velocity may be neglected. In the case of motion which we are considering, $udx + vdy$ is an exact differential $d\phi$ when friction is neglected, and

$$\phi = c\varepsilon^{-my} \sin\left(mx - nt\right), \tag{140}$$

where c, m, n are three constants, of which the last two are connected by a relation which it is not necessary to write down. We may continue to employ this equation as a near approximation when friction is taken into account, provided we suppose c, instead of being constant, to be parameter which varies slowly with the time. Let V be the *vis viva* of a given portion of the fluid at the end of the time t, then

$$V = \rho c^2 m^2 \iiint \varepsilon^{-2my} \mathrm{d}x\mathrm{d}y\mathrm{d}z. \tag{141}$$

But by means of the expression given in Art.49, we get for the loss of *vis viva* during the time $\mathrm{d}t$, observing that in the present case μ is constant, $w = 0$, $\delta = 0$, and $udx + vdy = \mathrm{d}\phi$, where ϕ is independent of z,

$$4\mu\mathrm{d}t \iiint \left\{ \left(\frac{\mathrm{d}^2\phi}{\mathrm{d}x^2}\right)^2 + \left(\frac{\mathrm{d}^2\phi}{\mathrm{d}y^2}\right)^2 + 2\left(\frac{\mathrm{d}^2\phi}{\mathrm{d}x\mathrm{d}y}\right)^2 \right\} \mathrm{d}x\mathrm{d}y\mathrm{d}z$$

8

which becomes, on substituting for ϕ its value,

$$8\mu c^2 m^4 \mathrm{d}t \iiint \varepsilon^{-2my}\mathrm{d}x\mathrm{d}y\mathrm{d}z.$$

But we get from (141) for the decrement of *vis viva* of the same mass arising from the variation of the parameter c

$$-2\rho m^2 c\frac{\mathrm{d}c}{\mathrm{d}t}\mathrm{d}t \iiint \varepsilon^{-2my}\mathrm{d}x\mathrm{d}y\mathrm{d}z.$$

Equating the two expressions for the decrement of *vis viva*, putting for m its value $2\pi\lambda^{-1}$, where λ is the length of a wave, replacing μ by $\mu'\rho$, integrating, and supposing c_0 to be the initial value of c, we get

$$c = c_0\varepsilon^{-\frac{16\pi^2\mu't}{\lambda^2}}.*$$

It will presently appear that the value of $\sqrt{\mu'}$ for water is about 0.0564, an inch and a second being the units of space and time. Suppose first that λ is two inches, and t ten seconds. Then $16\pi^2\mu't\lambda^{-2} = 1.256$, and $c: c_0:: 1 : 0.2848$, so that the height of the waves, which varies as c, is only about a quarter of what it was. Accordingly, the ripples excited on a small pool by a puff of wind rapidly subside when the exciting cause ceases to act.

Now suppose that λ is to fathoms or 2880 inches, and that t is 86400 seconds or a whole day. In this case $16\pi^2\mu't\lambda^{-2}$ is equal to only 0.005232, so that by the end of an entire day, in which time waves of this length would travel 574 English miles, the height would be diminished by little more than the one two hundredth part in consequence of friction. Accordingly, the long swells of the ocean are but little allayed by friction, and at last break on some shore situated at the distance of perhaps hundreds of miles from the region where they were first excited.

* In a footnote on page 624, Lamb notes that "Through an oversight in the original calculation the value $\lambda^2/16\pi^2\nu$ was too small by one half." The value 16 should be 8.

2.4 The distance a wave will travel before it decays by a certain amount

The observations made by Stokes about the distance a wave will travel before its amplitude decays by a given amount, point the way to a useful frame for the analysis of the effects of viscosity on wave propagation. Many studies of nonlinear irrotational waves can be found in the literature but the only study of the effects of viscosity on the decay of these waves known to us is due to M. Longuet-Higgins (1997) who used the dissipation method to determine the decay due to viscosity of irrotational steep capillary-gravity waves in deep water. He finds that the limiting rate of decay for small amplitude solitary waves are twice those for linear periodic waves computed by the dissipation method. The dissipation of very steep waves can be more than ten times more than linear waves due to the sharply increased curvature in wave troughs. He assumes that that the nonlinear wave maintains its steady form while decaying under the action of viscosity. The wave shape could change radically from its steady shape in very steep waves.

Stokes (1880) studied the motion of nonlinear irrotational gravity waves in two dimensions which are propagated with a constant velocity, and without change of form. This analysis led Stokes 1880 to the celebrated maximum wave whose asymptotic form gives rise to a pointed crest of angle $120°$. The effects of viscosity on such extreme waves has not been studied but they may be studied by the dissipation method or same potential flow theory used by Stokes (1851) for inviscid fluids with the caveat that the normal stress condition that p vanish on the free surface be replaced by the condition that

$$p + 2\mu\partial u_n/\partial n = 0$$

on the free surface with normal $\boldsymbol{n}$ where the velocity component $u_n = \partial\phi/\partial n$ is given by the potential.

3

Boundary conditions for viscous fluids

Boundary conditions for incompressible viscous fluids cannot usually be satisfied without contributions from potential flows (Joseph, Renardy 1991, § 1.2 (d)).

(1) No-slip conditions are required at the boundary S of a rigid solid:

$$\boldsymbol{u} = \boldsymbol{U} \quad \text{for } \boldsymbol{x} \in S, \tag{3.0.1}$$

where $\boldsymbol{U}$ is the velocity of the solid.

(2) At the interface S between two fluids, the fluid velocities are continuous, the shear stress is continuous and the stress is balanced by surface tension.

Now we shall express the condition just mentioned with equations. Let the position of the surface S as it moves through the surface be $F\left(\boldsymbol{x}\left(t\right), t\right) = 0$ where $\boldsymbol{x}\left(t\right) \in S$ for all t and $\dot{\boldsymbol{x}}\left(t\right) \in \boldsymbol{u}_S$ is the velocity of points of S. Since $F = 0$ is an identity in t, we have

$$\frac{\mathrm{d}F}{\mathrm{d}t} = \frac{\partial F}{\partial t} + \boldsymbol{u}_S \cdot \nabla F = 0; \tag{3.0.2}$$

in fact $\mathrm{d}^m F / \mathrm{d}t^m = 0$ for all m. Now, the normal $\boldsymbol{n}$ to S (figure 3.1) is $\boldsymbol{n} = \nabla F / \left|\nabla F\right|$; hence

$$\boldsymbol{u}_S \cdot \nabla F = \left(\boldsymbol{n} \cdot \boldsymbol{u}_S\right) \left|\nabla F\right|. \tag{3.0.3}$$

The tangential component of $\boldsymbol{u}_S$ is irrelevant and

$$\boldsymbol{n} \cdot \boldsymbol{u}_S = \boldsymbol{n} \cdot \boldsymbol{u}, \tag{3.0.4}$$

where $\boldsymbol{u}$ is the velocity of a material point on $\boldsymbol{x} \in S$.

We now set a convention for jumps in the value of variables as we cross S at $\boldsymbol{x}$. Define

$$[\![\bullet]\!] = \left(\bullet\right)_1 - \left(\bullet\right)_2,$$

where the subscript $\left(\bullet\right)_1$ means to evaluate $\left(\bullet\right)$ at $\boldsymbol{x}$ in the fluid 1; likewise for 2.

Combining (3.0.2), (3.0.3), and (3.0.4), we get the kinematic equation for the evolution of F

$$\frac{\mathrm{d}F}{\mathrm{d}t} = \frac{\partial F}{\partial t} + \boldsymbol{u} \cdot \nabla F = 0. \tag{3.0.5}$$

Since $\left[\!\!\left[\dfrac{\partial F}{\partial t}\right]\!\!\right] = 0$, we have

$$[\![\boldsymbol{u} \cdot \boldsymbol{n}]\!] = [\![\boldsymbol{u}]\!] \cdot \boldsymbol{n} = 0. \tag{3.0.6}$$
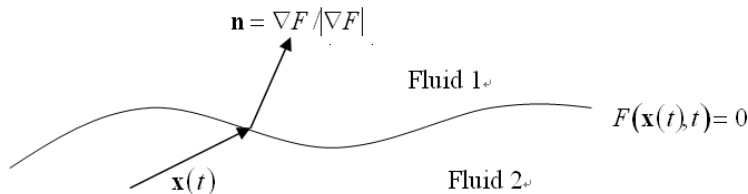
Fig. 3.1. Interface S between two fluids.

The normal component of velocity is continuous. If the tangential component of velocity is also continuous across S, we have

$$\boldsymbol{n} \times [[\boldsymbol{u}]] = 0 \quad \boldsymbol{x} \in S. \tag{3.0.7}$$

Turning now to the stress

$$\mathbf{T} = -p\mathbf{1} + 2\mu\mathbf{D}[\boldsymbol{u}], \tag{3.0.8}$$

$$T_{ij} = -p\delta_{ij} + \mu \left(\frac{\partial u_i}{\partial x_j} + \frac{\partial u_j}{\partial x_i} \right),$$

we express the continuity of the shear stress as

$$\boldsymbol{e}_S \cdot [[2\mu\mathbf{D}[\boldsymbol{u}]]] \cdot \boldsymbol{n} = 0, \tag{3.0.9}$$

where $\boldsymbol{e}_S$ is a unit vector tangent to S; $\boldsymbol{e}_S \cdot \nabla F = 0$.

The condition that the jump in the normal component of the stress is balanced by a surface tension force may be expressed as

$$\boldsymbol{n} \cdot [[\mathbf{T}]] \cdot \boldsymbol{n} = - [[p]] + 2\boldsymbol{n} \cdot [[\mu\mathbf{D}[\boldsymbol{u}]]] \cdot \boldsymbol{n} = 2H\gamma - \nabla_S\gamma, \tag{3.0.10}$$

where H is the mean curvature

$$2H = \frac{1}{R_1} + \frac{1}{R_2} \tag{3.0.11}$$

and R_1 and R_2 are principal radii of curvature. The surface gradient is

$$\nabla_S = \nabla - \boldsymbol{n}\left(\boldsymbol{n} \cdot \nabla\right). \tag{3.0.12}$$

The curvature $2H$ is determined by the surface gradient of the normal (see Joseph and Renardy, 1991)

$$2H = \nabla_S \cdot \boldsymbol{n}. \tag{3.0.13}$$

(3) Free surfaces. Free surfaces are two fluid interfaces for which one fluid is a dynamically inactive gas. The density of the gas is usually much less than the density of the liquid and the viscosity of the gas is usually much less than the viscosity of the liquid. In some cases we can put the viscosity and density of the gas to zero; then we have a liquid-vacuum interface. This procedure works well for problems of capillary instability and Rayleigh-Taylor instability. However, for Kelvin-Helmholtz instabilities the kinematic viscosity $\nu = \mu/\rho$ is important and ν for the liquid and gas are of comparable magnitude. The dynamic participation of the ambient is necessary for Kelvin-Helmholtz instability.

For free surface problems with a dynamically inactive ambient, no condition on the tangential velocity of the interface is required; the shear stress vanishes

$$2\mu\boldsymbol{e}_S \cdot \mathbf{D}\left[\boldsymbol{u}\right] \cdot \boldsymbol{n} = 0, \quad \boldsymbol{x} \in S \tag{3.0.14}$$

and the normal stress balance is

$$- p + 2\mu\boldsymbol{n} \cdot \mathbf{D}\left[\boldsymbol{u}\right] \cdot \boldsymbol{n} = 2H\gamma - \nabla_S\gamma \tag{3.0.15}$$

Sometimes the sign of the mean curvature is ambiguous (we could have assigned $\boldsymbol{n}$ from 2 to 1). A quick way to determine the sign is to look at the terms

$$- p = 2 \left(\frac{1}{R_1} + \frac{1}{R_2} \right) \gamma$$

making sure the pressure is higher inside the equivalent sphere.

Summarizing, the main equations on S are (3.0.5), (3.0.6), (3.0.7), (3.0.9), (3.0.10), (3.0.14), and (3.0.15). These equations are written for Cartesian, cylindrical, and spherical polar coordinates in Appendix A.

4

Helmholtz decomposition coupling rotational to irrotational flow

In this chapter we present the form of the Navier-Stokes equations implied by the Helmholtz decomposition in which the relation of the irrotational and rotational velocity fields is made explicit. The idea of self-equilibration of irrotational viscous stresses is introduced. The decomposition is constructed by first selecting the irrotational flow compatible with the flow boundaries and other prescribed conditions. The rotational component of velocity is then the difference between the solution of the Navier-Stokes equations and the selected irrotational flow. To satisfy the boundary conditions the irrotational field is required and it depends on the viscosity. Five unknown fields are determined by the decomposed form of the Navier-Stokes equations for an incompressible fluid; the rotational component of velocity, the pressure and the harmonic potential. These five fields may be readily identified in analytic solutions available in the literature. It is clear from these exact solutions that potential flow of a viscous fluid is required to satisfy prescribed conditions, like the no-slip condition at the boundary of a solid or continuity conditions across a two-fluid boundary. The decomposed form of the Navier-Stokes equations may be suitable for boundary layers because the target irrotational flow which is expected to appear in the limit, say at large Reynolds numbers, is an explicit to-be-determined field. It can be said that equations governing the Helmholtz decomposition describe the modification of irrotational flow due to vorticity but the analysis shows the two fields are coupled and cannot be completely determined independently.

4.1 Helmholtz decomposition

The Helmholtz decomposition theorem says that every smooth vector field $\boldsymbol{u}$, defined everywhere in space and vanishing at infinity together with its first derivatives can be decomposed into a rotational part $\boldsymbol{v}$ and an irrotational part $\nabla\phi$,

$$\boldsymbol{u} = \boldsymbol{v} + \nabla\phi, \tag{4.1.1}$$

where

$$\mathrm{div}\boldsymbol{u} = \mathrm{div}\boldsymbol{v} + \nabla^2\phi, \tag{4.1.2}$$

$$\mathrm{curl}\boldsymbol{u} = \mathrm{curl}\boldsymbol{v}. \tag{4.1.3}$$

This decomposition leads to the theory of the vector potential which is not followed here. The decomposition is unique on unbounded domains without boundaries and explicit formulas for the scalar and vector potentials are well known. A framework for embedding the study of potential flows of viscous fluids, in which no special flow assumptions are made, is suggested by this decomposition (Joseph 2006a, c). If the fields are solenoidal, then

$$\mathrm{div}\boldsymbol{u} = \mathrm{div}\boldsymbol{v} = 0 \text{ and } \nabla^2\phi = 0. \tag{4.1.4}$$

Since ϕ is harmonic, we have from (4.1.1) and (4.1.4) that

$$\nabla^2\boldsymbol{u} = \nabla^2\boldsymbol{v}. \tag{4.1.5}$$

The irrotational part of $\boldsymbol{u}$ is on the null space of the Laplacian but in special cases, like plane shear flow, $\nabla^2\boldsymbol{v} = 0$ but $\mathrm{curl}\boldsymbol{v} \neq 0$.

Unique decompositions are generated by solutions of the Navier-Stokes equation (4.2.1) in decomposed form (4.2.2) where the irrotational flows satisfy (4.1.1), (4.1.3), (4.1.4) and (4.1.5) and certain boundary conditions.

The boundary conditions for the irrotational flows have a heavy weight in all this. Simple examples of unique decomposition, taken from hydrodynamics, will be presented later.

The decomposition of the velocity into rotational and irrotational parts holds at each and every point and varies from point to point in the flow domain. Various possibilities for the balance of these parts at a fixed point and the distribution of these balances from point to point can be considered.

(i) The flow is purely irrotational or purely rotational. These two possibilities do occur as approximations but are not typical.

(ii) Typically the flow is mixed with rotational and irrotational components at each point.

4.2 Navier-Stokes equations for the decomposition

To study solutions of the Navier-Stokes equations, it is convenient to express the Navier-Stokes equations for an incompressible fluid

$$\rho \frac{\mathrm{d}\boldsymbol{u}}{\mathrm{d}t} = -\nabla p + \mu \nabla^2 \boldsymbol{u}, \tag{4.2.1}$$

in terms of the rotational and irrotational fields implied by the Helmholtz decomposition

$$\rho \frac{\partial \boldsymbol{v}}{\partial t} + \nabla \left\{ \rho \frac{\partial \phi}{\partial t} + \frac{\rho}{2} |\nabla \phi|^2 + p \right\} + \rho \mathrm{div} \left[\boldsymbol{v} \otimes \nabla \phi + \nabla \phi \otimes \boldsymbol{v} + \boldsymbol{v} \otimes \boldsymbol{v} \right] = \mu \nabla^2 \boldsymbol{v}, \tag{4.2.2}$$

or

$$\rho \frac{\partial v_i}{\partial t} + \frac{\partial}{\partial x_i} \left\{ \rho \frac{\partial \phi}{\partial t} + \frac{\rho}{2} |\nabla \phi|^2 + p \right\} + \rho \frac{\partial}{\partial x_j} \left(v_j \frac{\partial \phi}{\partial x_i} + v_i \frac{\partial \phi}{\partial x_j} + v_i v_j \right) = \mu \nabla^2 v_i,$$

satisfying (4.1.4).

To solve this problem in a domain Ω, say, when the velocity $\boldsymbol{u} = \boldsymbol{V}$ is prescribed on $\partial \Omega$, we would need to compute a solenoidal field $\boldsymbol{v}$ satisfying (4.2.2) and a harmonic function ϕ satisfying $\nabla^2 \phi = 0$ such that

$$\boldsymbol{v} + \nabla \phi = \boldsymbol{V} \text{ on } \partial \Omega.$$

Since this system of five equations in five unknowns is just the decomposed form of the four equations in four unknowns which define the Navier-Stokes system for $\boldsymbol{u}$, it ought to be possible to study this problem using exactly the same mathematical tools that are used to study the Navier-Stokes equations.

In the Navier-Stokes theory for incompressible fluid the solutions are decomposed into a space of gradients and its complement which is a space of solenoidal vectors. The gradient space is not, in general, solenoidal because the pressure is not solenoidal. If it were solenoidal, then $\nabla^2 p = 0$, but $\nabla^2 p = -\mathrm{div}\rho \boldsymbol{u} \cdot \nabla \boldsymbol{u}$ satisfies Poisson's equation.

It is not true that only the pressure is found on the gradient space. Indeed equation (4.2.2) gives rise to a Poisson's equation for the Bernoulli function, not just the pressure:

$$\nabla^2 \left[\rho \frac{\partial \phi}{\partial t} + \frac{\rho}{2} |\nabla \phi|^2 + p \right] = -\rho \frac{\partial^2}{\partial x_i \partial x_j} \left(v_j \frac{\partial \phi}{\partial x_i} + v_i \frac{\partial \phi}{\partial x_j} + v_i v_j \right).$$

In fact, there may be hidden irrotational terms on the right hand side of this equation.

The boundary condition for solutions of (4.2.1) is

$$\boldsymbol{u} - \boldsymbol{a} = 0 \text{ on } \partial \Omega,$$

where $\boldsymbol{a}$ is solenoidal field, $\boldsymbol{a} = \boldsymbol{V}$ on $\partial \Omega$. Hence,

$$\boldsymbol{v} - \boldsymbol{a} + \nabla \phi = 0 \tag{4.2.3}$$

The decomposition depends on the selection of the harmonic function ϕ; the traditional boundary condition

$$\boldsymbol{n} \cdot \boldsymbol{a} = \boldsymbol{n} \cdot \nabla \phi \text{ on } \partial \Omega \tag{4.2.4}$$

together with a Dirichlet condition at infinity when the region of flow is unbounded and a prescription of the value of the circulation in doubly connected regions, gives rise to a unique ϕ. Then the rotational flow must satisfy

$$\boldsymbol{v} \cdot \boldsymbol{n} = 0 \text{ and } \boldsymbol{e}_s \cdot (\boldsymbol{v} - \boldsymbol{a}) + \boldsymbol{e}_s \cdot \nabla \phi = 0 \tag{4.2.5}$$

on $\partial\Omega$. The $\boldsymbol{v}$ determined in this way is rotational and satisfies (4.1.3). However, $\boldsymbol{v}$ may contain other harmonic components.

Purely rotational flows $\boldsymbol{v}$ have no harmonic components. Purely rotational velocities can be identified in the exact solutions exhibited in the examples where the parts of the solution which are harmonic and the parts that are not are identified by inspection. Equation (4.6.6), in which the purely irrotational flow is identified by selecting a parameter α, is a good example. We have a certain freedom in selecting the harmonic functions used for the decomposition.

A more general formulation of the boundary condition generating the potential in the Helmholtz decomposition can be formed by replacing the Neumann condition (4.2.4) with a Robin condition

$$\alpha\phi + \beta\boldsymbol{n} \cdot \nabla\phi = \boldsymbol{a} \cdot \boldsymbol{n} \tag{4.2.6}$$

depending on two free parameters. The boundary conditions satisfied by the rotational velocity $\boldsymbol{v}$ are

$$\boldsymbol{v} \cdot \boldsymbol{n} + \boldsymbol{n} \cdot \nabla\phi = \boldsymbol{a} \cdot \boldsymbol{n}$$
$$\boldsymbol{v} \cdot \boldsymbol{e}_{\mathrm{s}} + \boldsymbol{e}_{\mathrm{s}} \cdot \nabla\phi = \boldsymbol{a} \cdot \boldsymbol{e}_{\mathrm{s}} \tag{4.2.7}$$

where ϕ is a harmonic function satisfying (4.2.6). The free parameters α and β can be determined to obtain an optimal result, where "optimal" is a concept that is in need of further elaboration. Ideally, we would like to determine α and β so that $\boldsymbol{v}$ is "purely rotational". The examples show that purely rotational flows exist in special cases. It remains to see if this concept makes sense in a general theory.

What is the value added to solutions of the Navier-Stokes equations (4.2.1) by solving them in the Helmholtz decomposed form† (4.2.2)? Certainly it is not easier to solve for five rather than four fields; if you cannot solve (4.2.1) then you certainly cannot solve (4.2.2). However, if the decomposed solution could be extracted from solutions of (4.2.1) or computed directly, then the form of the irrotational solution which is determined through coupling with the rotational solution and the changes in its distribution as the Reynolds number changes would be revealed. There is nothing approximate about this; it is the correct description of the role of irrotational solutions in the theory of the Navier-Stokes equations and it looks different and is different than the topic "potential flow of an inviscid fluid" which we all learned in school.

The form (4.2.2) of the Navier-Stokes equations may be well suited to the study of boundary layers of vorticity with irrotational flow of viscous fluid outside. It may be conjectured that in such layers $\boldsymbol{v} \neq 0$, whilst $\boldsymbol{v}$ is relatively small in the irrotational viscous flow outside. Rotational and irrotational flows are coupled in the mixed inertial term on the left of (4.2.2). The irrotational flow does not vanish in the boundary layer and the rotational flow though small probably, will not be zero in the irrotational viscous flow outside. This feature which is also in Prandtl's theory of boundary layers but that theory is not rigorous and the irrotational part is, so to say, inserted by hand and is not coupled to the rotational flow at the boundary. The coupling terms are of considerable interest and they should play strongly in the region of small vorticity at the edge of the boundary layer. The action of irrotational flow in the exact boundary layer solution of Hiemenz 1911 for steady two-dimensional flow toward a "stagnation point" at a rigid body (Batchelor 1967, pp. 286-288) and Hamel 1917 flow in diverging and converging channels in the Helmholtz decomposed form is discussed at the end of this chapter.

Effects on boundary layers on rigid solids arising from the viscosity of the fluid in the irrotational flow outside have been considered without the decomposition by Wang and Joseph 2006 a, b and by Padrino and Joseph 2006.

4.3 Self-equilibration of the irrotational viscous stress

The stress in a Newtonian incompressible fluid is given by

$$\mathbf{T} = -p\mathbf{1} + \mu\left(\nabla\boldsymbol{u} + \boldsymbol{u}^T\right) = -p\mathbf{1} + \mu\left(\nabla\boldsymbol{v} + \nabla\boldsymbol{v}^T\right) + 2\mu\nabla \otimes \nabla\phi.$$

Most flows have an irrotational viscous stress. The term $\mu\nabla^2\boldsymbol{v}$ in (4.2.2) arises from the rotational part of the viscous stress.

The irrotational viscous stress $\boldsymbol{\tau}_I = 2\mu\nabla \otimes \nabla\phi$ does not give rise to a force density term in (4.2.2). The

† A cultured lady asked a famous conductor of Baroque music if J.S. Bach was still composing. "No madame, he is decomposing."

divergence of $\boldsymbol{\tau}_I$ vanishes on each and every point in the domain V of flow. Even though an irrotational viscous stress exists, it does not produce a net force to drive motions. Moreover,

$$\int \mathrm{div}\boldsymbol{\tau}_I \mathrm{d}V = \oint \boldsymbol{n} \cdot \boldsymbol{\tau}_I \mathrm{d}S = 0. \tag{4.3.1}$$

The traction vectors $\boldsymbol{n} \cdot \boldsymbol{\tau}_I$ have no net resultant on each and every closed surface in the domain V of flow. We say that the irrotational viscous stresses, which do not drive motions, are self-equilibrated. Irrotational viscous stresses are not equilibrated at boundaries and they may produce forces there.

4.4 Dissipation function for the decomposed motion

The dissipation function evaluated on the decomposed field (4.1.1) sorts out into rotational, mixed and irrotational terms given by

$$\begin{aligned} \Phi &= \int_V 2\mu D_{ij}D_{ij}\mathrm{d}V \\ &= \int 2\mu D_{ij}\left[\boldsymbol{v}\right]D_{ij}\left[\boldsymbol{v}\right]\mathrm{d}V + 4\mu \int D_{ij}\left[\boldsymbol{v}\right]\frac{\partial^2 \phi}{\partial x_i \partial x_j}\mathrm{d}V + 2\mu \int \frac{\partial^2 \phi}{\partial x_i \partial x_j}\frac{\partial^2 \phi}{\partial x_i \partial x_j}\mathrm{d}V. \end{aligned} \tag{4.4.1}$$

Most flows have an irrotational viscous dissipation. In regions V' where $\boldsymbol{v}$ is small, we have approximately that

$$\mathbf{T} = -p\mathbf{1} + 2\mu \nabla \otimes \nabla \phi, \tag{4.4.2}$$

and

$$\Phi = 2\mu \int_{V'} \frac{\partial^2 \phi}{\partial x_i \partial x_j}\frac{\partial^2 \phi}{\partial x_i \partial x_j}\mathrm{d}V. \tag{4.4.3}$$

Equation (4.4.3) has been widely used to study viscous effects in irrotational flows since Stokes 1851.

4.5 Irrotational flow and boundary conditions

How is the irrotational flow determined? It frequently happens that the rotational motion cannot satisfy the boundary conditions; this well known problem is associated with difficulties in forming boundary conditions for the vorticity. The potential ϕ is a harmonic function which can be selected so that the values of the sum of the rotational and irrotational fields can be chosen to balance prescribed conditions at the boundary. The allowed irrotational fields can be selected from harmonic functions that enter into the purely irrotational solution of the same problem on the same domain. A very important property of potential flow arises from the fact that irrotational viscous stresses do not give rise to irrotational viscous forces in the equations (4.2.2) of motion. The interior values of the rotational velocity are coupled to the irrotational motion through Bernoulli terms evaluated on the potential and inertial terms which couple the irrotational and rotational fields. The dependence of the irrotational field on viscosity can be generated by the boundary conditions.

4.6 Examples from hydrodynamics

4.6.1 Poiseuille flow

A simple example which serves as a paradigm for the relation of the irrotational and rotational components of velocity in all the solutions of the Navier-Stokes equations, is plane Poiseuille flow

$$\left.\begin{aligned} \boldsymbol{u} &= \left[-\frac{P'}{2\mu}\left(b^2 - y^2\right),\ 0,\ 0\right], \\ \mathrm{curl}\boldsymbol{u} &= \left[0,\ 0,\ -\frac{P'y}{\mu}\right], \\ \boldsymbol{v} &= \left[\frac{P'}{2\mu}y^2,\ 0,\ 0\right], \\ \nabla\phi &= \left[-\frac{P'}{2\mu}b^2,\ 0,\ 0\right]. \end{aligned}\right\} \tag{4.6.1}$$

The rotational flow is a constrained field and cannot satisfy the no-slip boundary condition. To satisfy the no-slip condition we add the irrotational flow

$$\frac{\partial \phi}{\partial x} = -\frac{P'}{2\mu} b^2.$$

The irrotational component is for uniform and unidirectional flow chosen so that $\boldsymbol{u} = 0$ at the boundary.

4.6.2 Flow between rotating cylinders

$$\left.\begin{array}{l}
\boldsymbol{u} = \boldsymbol{e}_\theta u\,(r), \\[4pt]
\boldsymbol{u} = \boldsymbol{e}_\theta \Omega_a a \text{ at } r = a, \\[4pt]
\boldsymbol{u} = \boldsymbol{e}_\theta \Omega_a b \text{ at } r = b, \\[4pt]
u\,(r) = Ar + \dfrac{B}{r}, \\[8pt]
A = -\dfrac{a^2 \Omega_a - b^2 \Omega_b}{b^2 - a^2}, \\[8pt]
B = \dfrac{(\Omega_a - \Omega_b)\,a^2 b^2}{b^2 - a^2}, \\[8pt]
\boldsymbol{v} = \boldsymbol{e}_\theta Ar, \\[8pt]
\dfrac{1}{r}\dfrac{\partial \phi}{\partial \theta} = \dfrac{B}{r}.
\end{array}\right\} \tag{4.6.2}$$

The irrotational flow with $\boldsymbol{v} = 0$ is an exact solution of the Navier-Stokes equations with no-slip at boundaries.

4.6.3 Stokes flow around a sphere of radius a in a uniform stream U

This axisymmetric flow, described with spherical polar coordinates (r, θ, φ), is independent of φ. The velocity components can be obtained from a stream function $\psi\,(r, \theta)$ such that

$$\boldsymbol{u} = (u_r,\ u_\theta) = \frac{1}{r \sin \theta}\left(\frac{1}{r}\frac{\partial \psi}{\partial \theta},\ -\frac{\partial \psi}{\partial r}\right). \tag{4.6.3}$$

The stream function can be divided into rotational and irrotational parts

$$\psi = \psi_v + \psi_p, \quad \nabla^2 \psi_p = 0, \tag{4.6.4}$$

where ψ_p is the conjugate harmonic function. The potential ϕ corresponding to ψ_p is given by

$$\phi = \left(-\frac{A}{2r^2} + Cr\right) 2\cos \theta$$

where the parameters A and C are selected to satisfy the boundary conditions on $\boldsymbol{u}$.

The Helmholtz decomposition of the solution of the problem of slow streaming motion over a stationary

16

sphere is given by

$$
\left.
\begin{aligned}
&\boldsymbol{u} = (u_r,\ u_\theta) = \left(v_r + \frac{\partial \phi}{\partial r},\ v_\theta + \frac{1}{r}\frac{\partial \phi}{\partial \theta} \right), \\
&u_r = U\left[1 - \frac{3a}{2r} + \frac{1}{2}\left(\frac{a}{r}\right)^3 \right]\cos\theta, \\
&u_\theta = -U\left[1 - \frac{3a}{4r} - \frac{1}{4}\left(\frac{a}{r}\right)^3 \right]\sin\theta, \\
&\mathrm{curl}\boldsymbol{u} = U\left[0,\ 0,\ -\frac{3a}{2r^2}\sin\theta \right], \\
&v_r = -\frac{3}{2}\frac{a}{r}U\cos\theta, \\
&v_\theta = \frac{3}{4}\frac{a}{r}U\sin\theta, \\
&\phi = U\left[r - \frac{1}{4}\frac{a^3}{r^2} \right]\cos\theta, \\
&p - p_\infty = -\frac{3}{2}\frac{a}{r^2}\mu U\cos\theta.
\end{aligned}
\right\}
\tag{4.6.5}
$$

The potential for flow over a sphere is

$$
\phi = U\left[r - \frac{\alpha}{4}\frac{a^3}{r^2} \right]\cos\theta.
\tag{4.6.6}
$$

The normal component of velocity vanishes when $\alpha = -2$ and the tangential component vanishes when $\alpha = 4$. In the present case, to satisfy the no-slip condition, we take $\alpha = 1$. Both the rotational and irrotational components of velocity are required to satisfy the no-slip condition.

4.6.4 Streaming motion past an ellipsoid (Lamb 1932, pp. 604-605)

The problem of the steady translation of an ellipsoid in a viscous liquid was solved by Lamb 1932 in terms of the gravitational-potential Ω of the solid and another harmonic function χ corresponding to the case in which $\nabla^2\chi = 0$, finite at infinity with $\chi = 1$ for the internal space. Citing Lamb

If the fluid be streaming past the ellipsoid, regarded as fixed, with the general velocity U in the direction of x, we assume

$$
u = A\frac{\partial^2 \Omega}{\partial x^2} + B\left(x\frac{\partial \chi}{\partial x} - \chi \right) + U, \quad v = A\frac{\partial^2 \Omega}{\partial x \partial y} + Bx\frac{\partial \chi}{\partial y}, \quad w = A\frac{\partial^2 \Omega}{\partial x \partial z} + Bx\frac{\partial \chi}{\partial z}.
$$

These satisfy the equation of continuity, in virtue of the relations

$$
\nabla^2\Omega = 0, \quad \nabla^2\chi = 0;
$$

and they evidently make $u = U$, $v = 0, w = 0$ at infinity. Again, they make

$$
\nabla^2 u = 2B\frac{\partial^2 \chi}{\partial x^2}, \quad \nabla^2 v = 2B\frac{\partial^2 \chi}{\partial x \partial y}, \quad \nabla^2 w = 2B\frac{\partial^2 \chi}{\partial x \partial z}.
$$

We note next that $\nabla^2 \boldsymbol{v} = \nabla^2 \boldsymbol{u}$; the irrotational part of $\boldsymbol{u}$ is on the null space of the Laplacian. It follows that the rotational velocity is associated with χ and is given by the terms proportional to B. The irrotational velocity is given by

$$
\nabla\phi = \nabla\left(A\frac{\partial \Omega}{\partial x} \right).
$$

The vorticity is given by

$$
\boldsymbol{\omega} = -\boldsymbol{e}_y\left(2B\frac{\partial \chi}{\partial z} \right) + \boldsymbol{e}_z\left(2B\frac{\partial \chi}{\partial y} \right).
$$

4.6.5 Hadamard-Rybyshinsky solution for streaming flow past a liquid sphere

As in the flow around a solid sphere, this problem is posed in spherical coordinates with a stream function and potential function related by (4.6.3), (4.6.4) and (4.6.5). The stream function is given by

$$\psi = f(r)\sin^2\theta, \tag{4.6.7}$$

$$f(r) = \frac{A}{r} + Br + Cr^2 + Dr^4. \tag{4.6.8}$$

The irrotational part of (4.6.7) is the part that satisfies $\nabla^2\psi_p = 0$. From this it follows that

$$\psi_p = \left(\frac{A}{r} + Cr^2\right)\sin^2\theta, \tag{4.6.9}$$

$$\psi_v = \left(Br + Dr^4\right)\sin^2\theta. \tag{4.6.10}$$

The potential ϕ corresponding to ψ_p is given by (4.6.5).

The solution of this problem is determined by continuity conditions at $r = a$. The inner solution for $r < a$ is designated by $\bar{\boldsymbol{u}}$, $\bar{\boldsymbol{v}}$, $\bar{\phi}$, $\bar{\psi}$, $\bar{p}$, $\bar{\mu}$, $\bar{\rho}$.

The normal component of velocity

$$v_r + \frac{\partial\phi}{\partial r} = \bar{v}_r + \frac{\partial\bar{\phi}}{\partial r} \tag{4.6.11}$$

is continuous at $r = a$. The normal stress balance is approximated by a static balance in which the jump of pressure is balanced by surface tension so large that the drop is approximately spherical. The shear stress

$$\mu\boldsymbol{e}_\theta \cdot \left[\nabla\boldsymbol{v} + \nabla\boldsymbol{v}^T + 2\nabla\otimes\nabla\phi\right]\cdot\boldsymbol{e}_r = \bar{\mu}\boldsymbol{e}_\theta \cdot \left[\nabla\bar{\boldsymbol{v}} + \nabla\bar{\boldsymbol{v}}^T + 2\nabla\otimes\nabla\bar{\phi}\right]\cdot\boldsymbol{e}_r. \tag{4.6.12}$$

The coefficients A, B, C, D are determined by the condition that $\boldsymbol{u} = U\boldsymbol{e}_x$ as $r \to \infty$ and the continuity conditions (4.6.11) and (4.6.12). We find that when $r \leq a$,

$$\bar{f}(r) = \frac{\mu}{\mu + \bar{\mu}}\frac{1}{4}\frac{U}{a^2}\left(r^4 - a^2 r^2\right), \tag{4.6.13}$$

where the r^2 term is associated with irrotational flow and when $r \geq a$,

$$f(r) = \frac{1}{2}U\left(r^2 - ar\right) + \frac{\bar{\mu}}{\bar{\mu} + \mu}\frac{1}{4}U\left(\frac{a^3}{r} - ar\right), \tag{4.6.14}$$

where the r^2 and $\dfrac{a^2}{r}$ terms are irrotational.

4.6.6 Axisymmetric steady flow around a spherical gas bubble at finite Reynolds numbers

This problem is like the Hadamard-Rybyshinski problem, with the internal motion of the gas neglected, but inertia cannot be neglected. The coupling conditions reduce to

$$v_r + \frac{\partial\phi}{\partial r} = 0 \tag{4.6.15}$$

and

$$\boldsymbol{e}_\theta \cdot \left[\nabla\boldsymbol{v} + \nabla\boldsymbol{v}^T + 2\nabla\otimes\nabla\phi\right]\cdot\mathbf{e}_r = 0. \tag{4.6.16}$$

There is no flow across the interface at $r = a$ and the shear stress vanishes there.

The equations of motion are the r and θ components of (4.1.1) with time derivative zero. Since Levich 1949 it has been assumed that at moderately large Reynolds numbers, the flow in the liquid is almost purely irrotational with a small vorticity layer where $\boldsymbol{v} \neq 0$ in the liquid near $r = a$. The details of the flow in the vorticity layer, the thickness of the layer, the presence and variation of viscous pressure contribution all are unknown.

It may be assumed that the irrotational flow in the liquid outside the sphere can be expressed as a series of spherical harmonics. The problem then is to determine the participation coefficients of the different harmonics, the pressure distribution and the rotational velocity $\boldsymbol{v}$ satisfying the continuity conditions (4.6.15) and (4.6.16). The determination of the participation coefficients may be less efficient than a purely numerical simulation of Laplace's equation outside a sphere subject to boundary conditions on the sphere which are coupled to the rotational flow. This important problem has not yet been solved.

18

4.6.7 Viscous decay of free gravity waves (Lamb 1932, § 349)

Flows which depend on only two space variables such as plane flows or axisymmetric flows admit a stream function. Such flows may be decomposed into a stream function and potential function. Lamb calculated an exact solution of the problem of the viscous decay of free gravity waves as a free surface problem of this type. He decomposes the solution into a stream function ψ and potential function ϕ and the solution is given by

$$u = \frac{\partial \phi}{\partial x} + \frac{\partial \psi}{\partial y}, \quad v = \frac{\partial \phi}{\partial y} - \frac{\partial \psi}{\partial x}, \quad \frac{p}{\rho} = -\frac{\partial \phi}{\partial t} - gy, \tag{4.6.17}$$

where

$$\nabla^2 \phi = 0, \quad \frac{\partial \psi}{\partial t} = \nu \nabla^2 \psi. \tag{4.6.18}$$

This decomposition is a Helmholtz decomposition; it can be said that Lamb solved this problem in the Helmholtz formulation

Wang and Joseph (2006a) constructed a purely irrotational solution of this problem which is in very good agreement with the exact solution. The potential in the Lamb solution is not the same as the potential in the purely irrotational solution because they satisfy different boundary conditions. It is worth noting that viscous potential flow rather than inviscid potential flow is required to satisfy boundary conditions. The common idea that the viscosity should be put to zero to satisfy boundary conditions is deeply flawed. It is also worth noting that viscous component of the pressure does not arise in the boundary layer for vorticity in the exact solution; the pressure is given by (4.6.17)

4.6.8 Oseen flow (Milne-Thomson, pp. 696-698, Lamb 1932, pp. 608-616)

Steady streaming flow of velocity U of an incompressible fluid over a solid sphere of radius a which is symmetric about the x axis satisfies

$$U \frac{\partial \boldsymbol{u}}{\partial x} = -\frac{1}{\rho} \nabla p + \nu \nabla^2 \boldsymbol{u}, \tag{4.6.19}$$

where $\text{div}\,\boldsymbol{u} = 0$ and $U = 2k\nu$ (for convenience). The inertial terms in this approximation are linearized but not zero. The equations of motion in decomposed form are

$$\nabla \left[U \frac{\partial \phi}{\partial x} + \frac{p}{\rho} \right] + U \frac{\partial \boldsymbol{v}}{\partial x} = \nu \nabla^2 \boldsymbol{v}. \tag{4.6.20}$$

Since $\text{div}\,\boldsymbol{v} = 0$ and ϕ is harmonic, $\nabla^2 p = 0$ and $U \frac{\partial \text{curl}\boldsymbol{v}}{\partial x} = \nu \nabla^2 \text{curl}\boldsymbol{v}$. The rotational velocity is determined by a function χ

$$\begin{aligned} \boldsymbol{v} &= \frac{1}{2k} \nabla \chi - \boldsymbol{e}_x \chi, \\ \chi &= \frac{a_0}{r} \exp\left[-kr \left(1 - \cos\theta \right) \right]. \end{aligned} \tag{4.6.21}$$

The potential ϕ is governed by the Laplace equation $\nabla^2 \phi = 0$, for which the solution is given by

$$\phi = Ux + \frac{b_0}{r} + b_1 \frac{\partial}{\partial x} \left(\frac{1}{r} \right) + \ldots = Ur \cos\theta + \frac{b_0}{r} + b_1 \frac{-1}{r^2} \cos\theta + \ldots,$$

where Ux is the uniform velocity term. Using these, the velocity $u = (u_r, u_\theta)$ is expressed as

$$u_r = \frac{\partial \phi}{\partial r} + \frac{1}{2k} \frac{\partial \chi}{\partial r} - \cos\theta \chi, \quad u_\theta = \frac{1}{r} \frac{\partial \phi}{\partial \theta} + \frac{1}{2k} \frac{1}{r} \frac{\partial \chi}{\partial \theta} + \sin\theta \chi.$$

These should be zero at the sphere surface ($r = a$) to give;

$$b_0 = -\frac{a_0}{2k} = -\frac{3Ua}{4k} = -\frac{3a\nu}{2}, \quad a_0 = \frac{3Ua}{2}, \quad b_1 = \frac{Ua^3}{4}.$$

The higher order terms in the potential vanish.

To summarize, the decomposition of the velocity into rotational and irrotational components are

$$
\left.
\begin{aligned}
\boldsymbol{u} &= (u_r,\ u_\theta) = \left(v_r + \frac{\partial \phi}{\partial r},\ v_\theta + \frac{1}{r}\frac{\partial \phi}{\partial \theta} \right), \\
\operatorname{curl}\boldsymbol{u} &= \operatorname{curl}\boldsymbol{v}, \\
v_r &= \frac{1}{2k}\frac{\partial \chi}{\partial r} - \chi \cos\theta, \\
v_\theta &= \frac{1}{2kr}\frac{\partial \chi}{\partial \theta} + \chi \sin\theta, \\
\phi &= Ux - \frac{3Ua}{4kr} - \frac{Ua^3}{4r^2}\cos\theta.
\end{aligned}
\right\}
\tag{4.6.22}
$$

4.6.9 Flows near internal stagnation points in viscous incompressible fluids

The fluid velocity relative to uniform motion or rest vanishes at points of stagnation. These points occur frequently even in turbulent flow. When the flow is purely irrotational, the velocity potential ϕ can be expanded near the origin as a Taylor series

$$
\phi = \phi_0 + a_i x_i + \frac{1}{2} a_{ij} x_i x_j + O\left(x_i x_i^3 \right),
\tag{4.6.23}
$$

where the tensor a_{ij} is symmetric. At the stagnation point $\nabla \phi = 0$, hence $a_i = 0$; and since $\nabla^2 \phi = 0$ everywhere, we have $a_{ii} = 0$. The velocity is

$$
\frac{\partial \phi}{\partial x_i} = a_{ij} x_j
\tag{4.6.24}
$$

at leading order. The velocity components along the principal axes (x, y, z) of the tensor a_{ij} are

$$
u = ax, \quad v = by, \quad w = -(a+b)z,
\tag{4.6.25}
$$

where a and b are unknown constants relating to the flow field. Irrotational stagnation points in the plane are saddle points, centers are stagnation points around which the fluid rotates. Saddle points and centers are embedded in vortex arrays.

Taylor vortex flow (TVF) is a two-dimensional (x, y) array of counter-rotating vortices (figure 4.1) whose vorticity decays in time due to viscous diffusion $(\partial_t \omega = \nu \nabla^2 \omega)$. TVF is an exact solution of the time-dependent, incompressible Navier-Stokes equations (Taylor 1923). The instantaneous velocity components are:

$$
\begin{aligned}
\partial_y \psi = u_1(x, y, t) &= -\omega_0 \frac{k_y}{k^2} \cos(k_x x) \sin(k_y y) \exp\left(-\nu k^2 t\right), \\
-\partial_x \psi = u_2(x, y, t) &= \omega_0 \frac{k_x}{k^2} \sin(k_x x) \cos(k_y y) \exp\left(-\nu k^2 t\right),
\end{aligned}
\tag{4.6.26}
$$

where

$$
\psi = \frac{\omega_0}{k^2} \cos(k_x x) \cos(k_y y) \exp\left(-\nu k^2 t\right),
\tag{4.6.27}
$$

and

$$
\nabla^2 \psi = -k^2 \psi = \omega = \partial_y u_1 - \partial_x u_2.
\tag{4.6.28}
$$

$\omega(x, y, t)$ is the vorticity and ω_0 is the initial maximum vorticity, k_x and k_y are the wave numbers in the x and y directions, and $k^2 = k_x^2 + k_y^2$.

The vorticity vanishes at saddle points (X, Y). After expanding the solution in power series centered on a generic stagnation point we find that

$$
u_1(X, Y, t) = \frac{\omega_0 k_y k_x}{k^2} X + \alpha_1 X^3 + \beta_1 X Y^2 + ...,
\tag{4.6.29}
$$

$$
u_2(X, Y, t) = -\frac{\omega_0 k_y k_x}{k^2} Y + \alpha_2 Y^3 + \beta_2 Y X^2 + ...
\tag{4.6.30}
$$

The vorticity vanishes at $(X, Y) = (0,\ 0)$ and appears first at second order

$$
\omega(X, Y, t) = -\omega_0 k_x k_y XY \exp\left(-\nu k^2 t\right) + ...
\tag{4.6.31}
$$

20
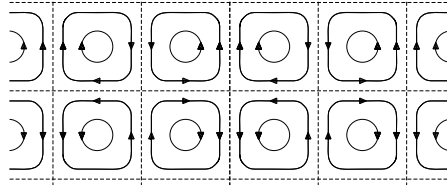
Fig. 4.1. (after Taylor 1923) Streamlines for system of eddies dying down under the action of viscosity. The streamlines are iso-vorticity lines; the vorticity vanishes on the border of the cells.

The Helmholtz decomposition of the local solution near $(X, Y) = (0, 0)$ is

$$u_1 = \frac{\partial \phi}{\partial X} + v_1, \quad u_2 = \frac{\partial \phi}{\partial Y} + v_2, \tag{4.6.32}$$

where

$$\left(\frac{\partial \phi}{\partial X}, \ \frac{\partial \phi}{\partial Y} \right) = \frac{\omega_0 k_y k_x}{k^2} \left(X, \ -Y \right), \tag{4.6.33}$$

and

$$(v_1, \ v_2) = \left(\alpha_1 X^3 + \beta_1 XY^2 + ..., \ \alpha_2 Y^3 + \beta_2 Y X^2 + ... \right). \tag{4.6.34}$$

This solution is generally valid in eddy systems which are segregated into quadrants near the stagnation point as in figure 4.1.

4.6.10 Hiemenz 1911 boundary layer solution for two-dimensional flow toward a "stagnation point" at a rigid boundary

Stagnation points on solid bodies are very important since the pressures at such points can be very high. But stagnation point flow cannot persist all the way to the boundary because of the no-slip condition. Hiemenz looked for a boundary layer solution of the Navier-Stokes equations vanishing at $y = 0$ which tends to stagnation point flow for large y expressed as

$$\boldsymbol{u} = (u, v), \tag{4.6.35}$$

$$\omega \left(\boldsymbol{u} \right) \boldsymbol{e}_z = \text{curl} \boldsymbol{u}.$$

The motion in the outer region is irrotational flow near a stagnation point at a plane boundary. The flow in the irrotational region is described by the stream function,

$$\psi = kxy,$$

where x and y are rectlinear co-ordinates parallel and normal to the boundary (see figure 4.2), with the corresponding velocity distribution

$$u = kx, \quad v = -ky. \tag{4.6.36}$$

k is a positive constant which, in the case of a stagnation point on a body fixed in a stream, must be proportional to the speed of the stream.

The next step is to determine the distribution of vorticity in the thin layer near the boundary from the equation

$$u \frac{\partial \omega}{\partial x} + v \frac{\partial \omega}{\partial y} = \nu \left(\frac{\partial^2 \omega}{\partial x^2} + \frac{\partial^2 \omega}{\partial y^2} \right), \tag{4.6.37}$$

together with boundary conditions that $u = 0$ and $v = 0$ at $y = 0$ and that the flow tends to the form (4.6.36) at the outer edge of the layer. Hiemenz found such a solution in the form

$$\psi = xf \left(y \right), \tag{4.6.38}$$

21
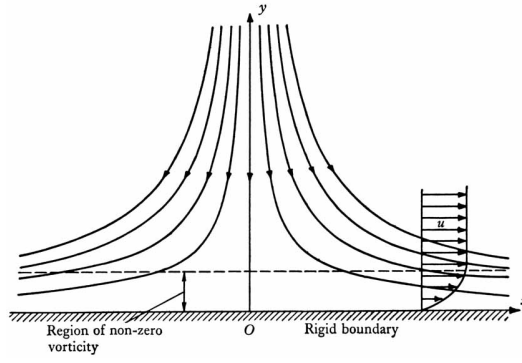
Fig. 4.2. Steady two-dimensional flow toward a 'stagnation point' at a rigid boundary.

corresponding to

$$u = xf'(y), \quad v = -f(y),$$

and

$$\omega = \frac{\partial v}{\partial x} - \frac{\partial u}{\partial y} = -xf''(y),$$

where $f(y)$ is an unknown function and primes denote differentiation with respect to y satisfying

$$-f'f'' + ff''' + \nu f^{iv} = 0,$$

and the boundary conditions

$$f = f' = 0 \text{ at } y = 0,$$

$$f \to ky \text{ as } y \to \infty.$$

Hiemenz 1911 showed that this system could be computed numerically and that it had a boundary layer structure in the limit of small ν (figure 4.2).

Alternatively, we may decompose the solution relative to a stagnation point in the whole space. To satisfy the no-slip condition the x component of stagnation point flow on $y = 0$ must be put to zero by an equal and opposite rotational velocity. For the decomposed motion, we have

$$\omega(\boldsymbol{u}) = \omega(\boldsymbol{v}), \tag{4.6.39}$$

$$\boldsymbol{u} = (u, \ v) = \left(v_x + \frac{\partial \phi}{\partial x}, \ v_y + \frac{\partial \phi}{\partial y} \right) = (v_x + kx, \ v_y - ky).$$

Instead of (4.6.37) we have the vorticity equation in the Helmholtz decomposed form

$$(v_x + kx)\frac{\partial \omega(\boldsymbol{v})}{\partial x} + (v_y - ky)\frac{\partial \omega(\boldsymbol{v})}{\partial y} = \nu \nabla^2 \omega(\boldsymbol{v}). \tag{4.6.40}$$

The solution of this problem is given by $\psi = xF(y)$ where $F(y) = f - ky$, $F(0) = 0$ and $F'(0) = -k$.

Analysis of a three dimensional stagnation point in the axisymmetric case was given by Homann (1936).

4.6.11 Jeffrey-Hamel flow in diverging and converging channels (Batchelor 1967, 294-302, Landau and Lifshitz 1987, 76-81)

The problem is to determine the steady flow between two plane walls meeting at angle α shown in figure 4.3 (a). Batchelor's discussion of this problem is framed in terms of the solutions $\boldsymbol{u} = (v_r, v_z, v_\varphi) = (v[r, \varphi], 0, 0)$ of the Navier-Stokes equations (4.2.1). The continuity equation $\dfrac{\partial rv}{\partial r} = 0$ shows that

$$v = \tilde{v}(\varphi)/r. \tag{4.6.41}$$

The function $\tilde{v}(\varphi)$ is determined by an involved but straightforward nonlinear analysis leading to the cartoons shown in figure 4.3 and figure 4.4.

22
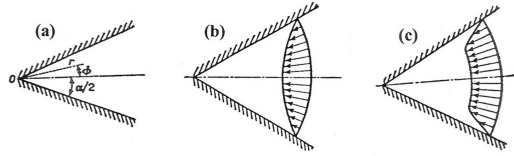
Fig. 4.3. Hamel sink flow. (a) flow channel, (b) irrotational sink flow, (c) sink flow with rotational boundary layer.
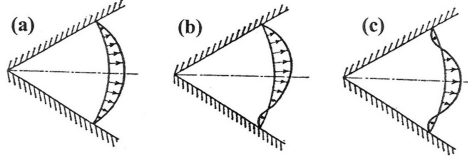
Fig. 4.4. Hamel source flow.(a) irrotational source flow (b) asymmetric rotational flow, (c) symmetric rotational flow.

We next consider the Helmholtz decomposition (4.1.1) of Hamel flow. Equation (4.6.41) shows that the only irrotational flow allowed in this decomposition is source or sink flow $\phi = C \log r$, where C is to be determined from the condition that

$$\tilde{v}(\varphi) + C = 0 \text{ at } \varphi = \pm\alpha.$$

The rotational field $\tilde{v}(\varphi)$ and constant C can be uniquely determined by an analysis like that given by Batchelor.

4.6.12 An irrotational Stokes flow

An extreme example of an irrotational flow at finite Reynolds numbers is an irrotational flow at zero Reynolds number. Such an example has been given by F.A.Morrison (1970) who proves that under very general conditions such as a uniform zeta potential, the slip-driven electro-osmotic flow about a charged particle is irrotational and the velocity field is proportional to the electric field disturbance relative to the imposed field. The interaction between the charged particle and the irrotational flow was considered. Morrison showed that the viscous stresses due to the irrotational flow do not give rise to a drag or torque on the particle. This result applies to particles of any shape provided that the flow is irrotational and the forces and torques are computed from viscous stresses computed on the irrotational flow. Morrison's result can be said to be more paradoxical than D'Alemberts' because the viscosity and viscous dissipation are not zero. The calculation of forces using the irrotational shear stress usually gives rise to erroneous results. A consequence of Morrison's uncorrected calculation of forces and torques is that the particle translates with the Smoluchowski velocity independent of its size, orientation, or presence of other particles and does not rotate. In this book we show Morrison's result is only valid for Stokes flows, since in the presence of inertia the torque-free condition is ruined. So inertia here actually interrupts the irrotationality.

Yariv and Brenner (2003, 2004) showed that if the zeta potential is non uniform, the flow can be decomposed to a potential part and a rotational part, as in the Helmholtz decomposition discussed in Chapter 4.

4.6.13 Lighthill's approach

A form of the Helmholtz decomposition depending on the law of Biot-Savart was considered by Lighthill. He notes that Lamb (1932 chapter vii) has shown that for *any* given solenoidal distribution of vorticity ω outside the body surface whose motion is prescribed , one and only one solenoidal velocity exists, tending to zero at infinity and with zero normal relative velocity at the solid surface. We have

$$\boldsymbol{v}_0 = \int \frac{\boldsymbol{\omega} \times \boldsymbol{r}}{4\pi r^3} \mathrm{d}\Omega \tag{4.6.42}$$

where the integration is over the whole vorticity field and $\boldsymbol{r}$ is the position vector relative to the volume element $\mathrm{d}\Omega$. In general, $\boldsymbol{v}_0$ does not satisfy the boundary condition for $\boldsymbol{v}$. However, the difference $\boldsymbol{v} - \boldsymbol{v}_0$ must be

irrotational (since curl$\boldsymbol{v}_0 = \boldsymbol{\omega}$), and hence equal to gradϕ for some potential ϕ. On the body surface

$$\frac{\partial \phi}{\partial n} = v_n - v_{0n} = v_{\omega n} - v_{0n} \tag{4.6.43}$$

which is fixed, and also grad $\phi \to 0$ at infinity. Modulo an additive constant, just one ϕ satisfies these conditions. Lighthill notes that the formulation (4.6.42-4.6.43) gives rise to a tangential velocity at the surface which may not satisfy the no-slip condition. In fact, the Biot-Savart velocity will not in general satisfy the no-slip condition. The spurious slip velocity may be viewed as a vortex sheet on the surface of the body. In order to enforce the no-slip boundary condition the vortex sheet is distributed diffusively into the flow, transferring the vortex sheet into an equivalent vortex layer by means of a vorticity flux. The no-slip condition therefore determines the vorticity flux, which is the strength of the spurious vortex sheet divided by the time increment. This construction of Lighthill's is the basis for numerical constructions of Chorin (1973) to slightly viscous flow and Chorin (1978) to the boundary layer equations.

Lighthill's Biot-Savart decomposition is the same as our PDE formulation (4.22) – (4.24) with ϕ determined by the normal component of the prescribed data and the rotational velocity $\boldsymbol{v}$ generated by solutions of (4.22) with the caveat that ϕ is determined by the boundary conditions (4.24) which guarantee no-slip. We feel that our formulation has left open the question of "purely rotational" flows which possibly may be addressed by a better choice for generating the irrotational flow in the decomposition.

We have emphasized that irrotational functions are needed to satisfy the no-slip condition, the boundary conditions for the rotational component need not be restricted to solenoidal vectors with zero normal component as is required by Lamb's theorem. The example of Stokes flow over a sphere is instructive since, for this example, everything is definite and cannot be manipulated. The rotational component is purely rotational; it has no irrotational part and it gives rise to the vorticity. It does not have a zero normal component as is required for the Biot-Savart approach. The irrotational components are required to satisfy the boundary condition. The irrotational flow does not have a zero normal component, rather the irrotational flow satisfies a Robin condition in which a linear combination of the tangential and normal components have equal weight.

4.6.14 Conclusion

The Helmholtz decomposition gives rise to an exact theory of potential flow in the frame of the Navier-Stokes equations in which rotational and irrotational fields are tightly coupled and both fields depend on viscosity. This kind of theory leads to boundary layers of vorticity in asymptotic limits but the fields are always coupled. The exact theory is different than purely irrotational theories of the effect of viscosity which can lead to excellent but always approximate results.

Finally, we note that the decomposition (4.1.1) through (4.1.5) does not depend on dynamics and may be applied to non- Newtonian fluids. Irrotational motions of non-Newtonian fluids are surely important but the coupling of rotational and irrotational fields has not been studied or even identified as a subject worthy of study.

5

Harmonic functions which give rise to vorticity

The rotational component of the velocity in Stokes flow is generated by products of powers and harmonic functions. This is yet another way in which potential flow enters into the fluid mechanics of viscous fluids. The simplest case is for plane flow in two dimensions. Here we may satisfy the continuity equation

$$\frac{\partial u}{\partial x} + \frac{\partial v}{\partial y} = 0 \tag{5.0.1}$$

with a stream function

$$[u, \ v] = \left[\frac{\partial \psi}{\partial y}, \ -\frac{\partial \psi}{\partial x} \right]. \tag{5.0.2}$$

The vorticity

$$\omega = \boldsymbol{e}_z \cdot \mathrm{curl} \boldsymbol{u} = \frac{\partial v}{\partial x} - \frac{\partial u}{\partial y} = -\nabla^2 \psi \tag{5.0.3}$$

For irrotational flow, $\omega = 0$ and $\psi = \psi_I$ is harmonic

$$\nabla^2 \psi_I = 0. \tag{5.0.4}$$

The Stokes equations for steady plane flow are

$$\left.\begin{aligned} \mu \nabla^2 u &= \frac{\partial p}{\partial x}, \\ \mu \nabla^2 v &= \frac{\partial p}{\partial y}. \end{aligned}\right\} \tag{5.0.5}$$

Hence

$$\mu \nabla^2 \left(\frac{\partial v}{\partial x} - \frac{\partial u}{\partial y} \right) = \mu \nabla^2 \omega = 0. \tag{5.0.6}$$

The vorticity is a harmonic function.

Suppose that H is an arbitrary harmonic function and

$$\boldsymbol{r} = \boldsymbol{e}_x x + \boldsymbol{e}_y y \tag{5.0.7}$$

Then

$$\nabla^2 \left(\boldsymbol{r} H \right) = 2 \nabla H \tag{5.0.8}$$

Hence, the function

$$\psi = \psi_I + x H_1 + y H_2, \tag{5.0.9}$$

where H_1 and H_2 are harmonic, satisfies

$$\omega = 2 \frac{\partial H_1}{\partial x} + 2 \frac{\partial H_2}{\partial y} \tag{5.0.10}$$

where $\nabla^2 \omega = 0$ and

$$\psi_I, \ H_1, \ H_2 \tag{5.0.11}$$

are selected to satisfy boundary conditions.

H. Lamb 1932 developed a general solution (§ 335 and 336) of Stokes equation in terms of spherical harmonics. Lamb's arguments are very cumbersome. Prof. H. Weinberger has developed a much simpler approach to this problem which leads to Lamb's result and is given below

The main tool is the identity

$$(1 + r\partial/\partial r)\,\boldsymbol{v} = \operatorname{grad}(\boldsymbol{r}\cdot\boldsymbol{v}) - \boldsymbol{r}\times\operatorname{curl}\boldsymbol{v}, \tag{5.0.12}$$

which holds for all vector fields, and is essentially Equation (5) of Article 335.

As in article 335, we will first look at the case of constant pressure. In this case

$$\operatorname{curl}(\operatorname{curl}\boldsymbol{u}) = 0,$$

and of course $\operatorname{div}(\operatorname{curl}\boldsymbol{u}) = 0$, so that $\operatorname{curl}\boldsymbol{u}$ is the gradient of some harmonic function m. As Lamb points out, the function $l := \mathbf{r}\cdot\boldsymbol{u}$ is also harmonic. Thus, (5.0.12) with $\boldsymbol{v} = \boldsymbol{u}$ shows that

$$(1 + r\partial/\partial r)\,\boldsymbol{u} = \operatorname{grad}l - \boldsymbol{r}\times\operatorname{grad}m. \tag{5.0.13}$$

We note that if ϕ is a solution of the equation

$$(r\partial/\partial r)\,\phi = l \tag{5.0.14}$$

then

$$\operatorname{grad}l = (1 + r\partial/\partial r)\operatorname{grad}\phi \tag{5.0.15}$$

Similarly, we see that if

$$(1 + r\partial/\partial r)\,\psi = m, \tag{5.0.16}$$

then

$$\boldsymbol{r}\times\operatorname{grad}m = (1 + r\partial/\partial r)\,\boldsymbol{r}\times\operatorname{grad}\psi. \tag{5.0.17}$$

By substituting (5.0.15) and (5.0.17) into (5.0.13), we see that

$$\boldsymbol{u} = \operatorname{grad}\phi - \boldsymbol{r}\times\operatorname{grad}\psi + \mathbf{w}\,(\Omega)\,/r, \tag{5.0.18}$$

where $\mathbf{w}$ is an arbitrary vector-valued function of the angle variables in spherical coordinates. We shall now show that we can choose the solution ϕ (5.0.14) to be harmonic. By taking the Laplacian of both sides of (5.0.14), we see that

$$(2 + r\partial/\partial r)\left(\nabla^2\phi\right) = 0.$$

This shows that if $\nabla^2\phi$ is zero at one point, it is zero on the radial line from the origin through this point. On the other hand, if we apply the operator $(1 + r\partial/\partial r)\,\psi$ to both sides of (5.0.14), we see that

$$r^2\nabla^2\phi = (1 + r\partial/\partial r)\,l + \Delta_\Omega\psi,$$

where Δ_Ω is the surface Laplacian on the unit sphere. We can make $\nabla^2\phi = 0$ on a spherical surface $r = r_0$ by setting the right-hand side equal to zero and solving the resulting equation for $\phi\,(r_0, \Omega)$. This can easily be done if the intersection of the flow domain with the sphere $r = r_0$ has a non trivial boundary. If it is the whole sphere, this problem can be solved if and only if the integral of $(1 + r\partial/\partial r)\,l$ over the whole sphere is zero. Because only the gradient of l appears in (5.0.14), we can add a constant to l to make this true. Thus, we can assume without loss of generality that the solution ϕ of (5.0.14) is harmonic. In the same way, we arrive at the conclusion that ψ can be taken to be harmonic.

By taking the Laplacian and divergence of both sides of (5.0.18), we see that $\mathbf{w}{=}0$. Thus we have shown that the velocity of any Stokes flow with constant pressure can be written in the form

$$\boldsymbol{u} = \operatorname{grad}\phi - \boldsymbol{r}\times\operatorname{grad}\psi, \tag{5.0.19}$$

where ϕ and ψ are harmonic. It is easily verified that for any harmonic ϕ and ψ this formula gives the velocity of a steady Stokes flow. This is the most general class of velocity fields which are self-equilibrating in the sense that they produce no body force.

The decomposition (5.0.19) of the velocity of a steady Stokes flow with constant pressure is unique. However, while this decomposition may be useful for domains which are nice in spherical coordinates, it is probably not very useful for dealing with domains with other symmetries of no symmetries.

In order to obtain a steady Stokes flow with variable pressure, it is only necessary to obtain one such solution for a prescribed pressure. Once this is done, the general solution can be obtained by adding the solution (5.0.19) which corresponds to zero pressure. Following Lamb, we seek a solution in the form

$$\boldsymbol{u} = \operatorname{grad}\Lambda - H\boldsymbol{r},$$

where H is harmonic, but Λ is only biharmonic. The condition $\operatorname{div}\boldsymbol{u} = 0$ leads to the equation

$$\nabla^2\Lambda = (3 + r\partial/\partial r)\,H. \tag{5.0.20}$$

26

Then the condition $\nabla^2 \boldsymbol{u} = \mathrm{grad}\, p$ leads to

$$\mathrm{grad}\,(3 + r\partial/\partial r)\, H - 2\mathrm{grad}\, H = \mathrm{grad}\, p,$$

or

$$(1 + r\partial/\partial r)\, H = p. \tag{5.0.21}$$

We again choose the harmonic solution of this equation. One still needs to find a solution Λ of (5.0.20). We seek this solution in the form

$$\Lambda = r^2 Q,$$

where Q is harmonic. Then the equation (5.0.20) becomes

$$(6 + 4r\partial/\partial r)\, Q = (3 + r\partial/\partial r)\, H. \tag{5.0.22}$$

As with the other equations, one can show that this one has a harmonic solution Q. We thus have the solution

$$\boldsymbol{u} = \mathrm{grad}\,(r^2 Q) - H\boldsymbol{r} \tag{5.0.23}$$

with the harmonic functions Q and H defined above in terms of the pressure p. It is easily verified that for any harmonic function H one can construct a harmonic function Q by solving (5.0.22), and that then (5.0.23) gives the velocity of a steady Stokes flow. By adding the right-hand side of (5.0.19), we obtain a representation

$$\boldsymbol{u} = \mathrm{grad}\,\phi - \boldsymbol{r} \times \mathrm{grad}\,\psi + \mathrm{grad}\,(r^2 Q) - H\boldsymbol{r} \tag{5.0.24}$$

of all steady Stokes flow in terms of three arbitrary harmonic functions.

The representations just derived show that velocity of Stokes flow may be decomposed into an irrotational part and a rotational part which is given by a composition of powers and harmonic functions. This is a Helmholtz decomposition with an additional feature which promotes the importance of harmonic functions in representing the rotational velocity.

The examples from hydrodynamics discussed in Chapter 4 exhibit all the features specified in the representations in this chapter. The examples show that the irrotational and rotational components of velocity are required to satisfy the boundary conditions.

The rotational velocity of Poiseuille flow given by (4.6.1) is yH where $H = -p'y/\mu$ is harmonic. The rotational velocity (4.6.2) between rotating cylinders is proportional to r, which is r^2 times the irrotational velocity proportional to $1/r$. The rotational velocity for Stokes flow around a sphere given in (4.6.6) is proportional to $1/r$ which is r^2 times the irrotational velocity proportional to $1/r^3$. The rotational velocity for streaming flow past an ellipsoid is given by $x\nabla\chi$ when χ is harmonic. The flow over a liquid sphere associated with (4.6.13) and (4.6.14) is like the flow over a solid sphere; the rotational velocity is proportional to r^2 times the irrotational velocity.

The idea that the rotational velocity can be replaced by products of powers and harmonic functions applies to many flows which are not Stokes flow.

6

Radial motions of a spherical gas bubble in a viscous liquid

The problem of radial motion of a gas bubble in a liquid was first studied by Rayleigh 1917. The expanding bubble can be framed as a cavitation result induced by an underwater explosion. The contracting bubble can be viewed as the collapse of a cavitation bubble. Since the motion is purely radial, vorticity is not guaranteed and the effects of the viscosity of the liquid can be determined by potential flow. This problem was also considered by Batchelor 1967 (p. 479) but, as in Rayleigh's work, with viscosity and surface tension neglected. Viscosity μ and surface tension γ effects can be introduced into this problem without approximation because the motion is purely radial and irrotational. Though Plesset 1949 introduced a variable driving pressure and surface tension, the effects of surface tension were also introduced and the effects of viscosity were first introduced by Poritsky 1951. The viscous terms were introduced by Poritsky 1951 and not by Plesset 1949. For this reason, we call equation (6.0.7) the Rayleigh-Poritsky equation rather than the Rayleigh-Plesset equation.

The Rayleigh-Poritsky equation arises from the normal stress balance. The velocity

$$u = R^2 \dot{R}/r^2 \tag{6.0.1}$$

is purely radial, R is the radius of the bubble $\dot{R} = \mathrm{d}R/\mathrm{d}t$ and $u = \dot{R}$ when $r = R$. This is a potential flow

$$\phi = -R^2 \dot{R} \frac{1}{r}. \tag{6.0.2}$$

The pressure in the liquid is given by the Bernoulli equation (6.0.3)

$$\frac{p - p_\infty}{\rho} = -\frac{\partial \phi}{\partial t} - \frac{1}{2}u^2 = \frac{2R\dot{R}^2 + R^2\ddot{R}}{r} - \frac{1}{2}\frac{R^4\dot{R}^2}{r^4} \tag{6.0.3}$$

where p_∞ is the uniform pressure far from the bubble. At $r = R$, (6.0.3) reduces to

$$\rho \left(R\ddot{R} + \frac{3}{2}\dot{R}^2 \right) = p - p_\infty \tag{6.0.4}$$

The normal stress balance at $r = R$ is

$$\frac{2\gamma}{R} = T_{rr}(l) - T_{rr}(g). \tag{6.0.5}$$

where γ is the tension, l is for the liquid, g is for the gas and $T_{rr}(g) = -p_b$ where p_b is bubble pressure and

$$T_{rr}(l) = -p + 2\mu\frac{\partial u}{\partial r} \tag{6.0.6}$$

Combining now (6.0.4) and (6.0.6) with (6.0.1), we get

$$\frac{2\gamma}{R} = p_b - p_\infty - \rho\left(R\ddot{R} + \frac{3}{2}\dot{R}^2\right) - 4\mu\frac{\dot{R}}{R}. \tag{6.0.7}$$

Equation (6.0.7) is an evolution equation for the bubble radius $R(t)$. This equation is always called the Rayleigh-Plesset equation but Plesset did not present or discuss this equation which is given as (62) in the 1951 paper of Poritsky. It is well known when γ and μ are neglected, that equation (6.0.7) can be formulated as an energy equation

$$\frac{\mathrm{d}}{\mathrm{d}t}KE = (p_b - p_\infty)\dot{V}$$

where

$$KE = \frac{1}{2} \int_R^\infty \rho \left(\frac{\partial \phi}{\partial r} \right)^2 4\pi r^2 \mathrm{d}r$$

and

$$\dot{V} = \frac{\mathrm{d}}{\mathrm{d}t} \left(\frac{4}{3} \pi R^3 \right).$$

The equation

$$(p_b - p_\infty) \, \dot{V} = \frac{\mathrm{d}KE}{\mathrm{d}t} + D + 2\gamma \frac{\dot{V}}{R} \tag{6.0.8}$$

where the dissipation

$$D = 2\mu \int_R^\infty \frac{\partial^2 \phi}{\partial x_i \partial x_j} \frac{\partial^2 \phi}{\partial x_i \partial x_j} 4\pi r^2 \mathrm{d}r = 16\pi \mu^2 R \dot{R}^2$$

follows from (6.0.7) after multiplication by $\dot{V}$.

The last term of (6.0.7) is from the viscous normal stress. This term converts to the viscous dissipation in the energy balance.

Rayleigh's analysis and its extensions to viscous and surface tension effects have applications to problems of cavitation, bubble collapse and underwater explosions. For these applications the study of stability is important. Taylor 1950 showed that an interface is unstable when the light fluid is accelerated towards the dense fluid as is explained in §9.1 and 9.2. The corresponding problem for a spherical interface was first discussed by Binnie 1953 who considered the collapse of vapor bubbles; his analysis is said to be flawed (see Plesset, 1954). The stability problem of this time dependent problem is very complicated; normal modes cannot be used. An initial value problem must be solved, disturbances cannot be restricted to radial symmetry. Simplifying features are lost. Results by Birkhoff 1954 and Plesset 1954 are stated with many qualifiers and require special assumptions. The problem of stability of a spherical gas bubble in an inviscid liquid was considered by Birkhoff 1954 who reduced the problem to the study of perturbations of the free surface expressed by Legendre polynomials

$$r = b(t) + \sum_{n=1}^\infty b_n(t) P_n(\cos \varphi).$$

He derives coupled ODE's for $b(t)$ and $b_n(t)$ and from the study of these equations. He finds stability during expansion, and instability during collapse. Birkhoff's result is surprising. Collapsing bubbles for which the dense fluid is being accelerated toward the lighter vapor are unstable.

Birkhoff's result neglects the effects of viscosity. It would be of interest to see the effects of viscosity using irrotational theories.

7

Rise velocity of a spherical cap bubble

The theory of viscous potential flow (Joseph 2005) was applied to the problem of finding the rise velocity U of a spherical cap bubble (Davies and Taylor 1950, Batchelor 1967). The rise velocity is given by

$$\frac{U}{\sqrt{gD}} = -\frac{8}{3}\frac{\nu\,(1+8s)}{\sqrt{gD^3}} + \frac{\sqrt{2}}{3}\left[1 - 2s - \frac{16s\sigma}{\rho gD^2} + \frac{32\nu^2}{gD^3}\,(1+8s)^2\right]^{1/2}$$

where $R = D/2$ is the radius of the cap, ρ and ν are the density and kinematic viscosity of the liquid, σ is surface tension and $s = r''(0)/D$ is the deviation of the free surface

$$r(\theta) = R + \frac{1}{2}r''(0)\theta^2 = R\left(1 + s\theta^2\right)$$

from perfect sphericity $r(\theta) = R$ near the stagnation point $\theta = 0$. The bubble nose is more pointed when $s < 0$ and blunted when $s > 0$. A more pointed bubble increases the rise velocity; the blunter bubble rises slower.

The Davies-Taylor 1950 result

$$U = \frac{\sqrt{2}}{3}\sqrt{gD}$$

arises when all other effects vanish; if s alone is zero,

$$\frac{U}{\sqrt{gD}} = -\frac{8}{3}\frac{\nu}{\sqrt{gD^3}} + \frac{\sqrt{2}}{3}\left[1 + \frac{32\nu^2}{gD^3}\right]^{1/2} \tag{7.0.1}$$

showing that viscosity slows the rise velocity. Equation (7.0.1) gives rise to a hyperbolic drag law

$$C_D = 6 + 32/R_e$$

which agrees with data on the rise velocity of spherical cap bubbles given by Bhaga and Weber 1981.

7.1 Analysis

The spherical cap bubble (figure 7.1) arises in the motion of large gas bubbles which take a lenticular shape. The analysis of the rise velocity of these bubbles which was given by Davies and Taylor 1950 is unusual since it is not computed from a balance of the drag and buoyant weight as it is for spherical gas bubbles (Levich 1949; Moore 1959, 1963; Taylor and Acrivos 1964; Miksis, Vanden-Broeck and Keller 1982; Ryskin and Leal 1984). Batchelor 1967 notes that "The remarkable feature of (the Davies-Taylor analysis) is that the speed of movement of the bubble is derived in terms of the bubble shape without any need for consideration of the mechanism of the retarding force which balances the effect of the buoyancy force on a bubble in steady motion."

The analysis of Davies & Taylor of the rise velocity of a spherical cap bubble is based on potential flow of an inviscid fluid. Here, we extend this analysis to viscous fluids with surface tension. The surface tension effects enter only when the axisymmetric bubble is not spherical. The analysis of the irrotational effects of viscosity is clear but the analysis of surface tension is *ad hoc* since the deviation-from-sphericity-parameter s is not calculated and its back influence to the potential is unknown. These defects are removed in the analysis of the rise velocity of an ellipsoidal bubble in chapter 8.

The velocity field on the gas bubble and the liquid is derived from a potential $\boldsymbol{u} = \nabla\phi$, $\nabla^2\phi = 0$. The velocity at $z = \infty$ is $-U$ (against z) and $\boldsymbol{g} = -\boldsymbol{e}_z g$. For steady flow

$$\rho\boldsymbol{u}\cdot\nabla\boldsymbol{u} = -\nabla p - \rho\boldsymbol{e}_z g = -\nabla\Gamma, \tag{7.1.1}$$
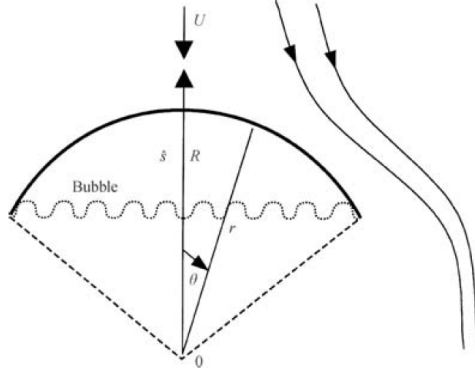
Fig. 7.1. Spherical cap bubble. The rising bubble is viewed in a frame in which the bubble is stationary. The origin of z increasing is at the stagnation point $\hat{s}$. The surface of the cap is given by $z = -h(r,\theta) = -(R - r(\theta)\cos\theta)$. The cap is strictly spherical if $r(\theta) = R$ is constant.

where

$$\Gamma = p + \rho g z.$$

Equation (7.1.1) may be integrated, since $\boldsymbol{u} \cdot \nabla \boldsymbol{u} = \nabla |\boldsymbol{u}|^2/2$, giving rise to a Bernoulli function in the liquid

$$\frac{\rho |\mathbf{u}|^2}{2} + \Gamma = \frac{\rho U^2}{2}, \tag{7.1.2}$$

and in the gas

$$\frac{\rho_G |\boldsymbol{u}|^2}{2} + \Gamma_G = C_G, \tag{7.1.3}$$

where C_G is an unknown constant.

We turn next to the normal stress balance

$$-[\![p]\!] + 2[\![\mu \boldsymbol{n} \cdot \mathbf{D}[\boldsymbol{u}] \cdot \boldsymbol{n}]\!] + \frac{2\sigma}{r(\theta)} = 0, \tag{7.1.4}$$

where

$$[\![\cdot]\!] = (\cdot)_G - (\cdot)_L$$

is evaluated on the free surface $r(\theta) = R\left(1 + s\theta^2\right)$, σ is surface tension, μ is viscosity and

$$\boldsymbol{n} \cdot \mathbf{D}[\boldsymbol{u}] \cdot \boldsymbol{n} = \frac{\partial u_n}{\partial n} \tag{7.1.5}$$

is the normal component of the rate of strain. Using (7.1.1), (7.1.4) and (7.1.5) we obtain

$$-[\![\Gamma]\!] - [\![\rho]\!]\, gh + 2\left[\!\left[\mu \frac{\partial u_n}{\partial n}\right]\!\right] + \frac{2\sigma}{r} = 0 \tag{7.1.6}$$

where $-h$ is the value of z on the free surface.

Following Davies and Taylor 1950, we assume that $\boldsymbol{u}$ may be approximated near the stagnation point on the bubble, which is nearly spherical, by the potential for the sphere; thus

$$\phi = -Ur\cos\theta\left(1 + \frac{R^3}{2r^3}\right) \tag{7.1.7}$$

for the liquid. The form of ϕ in the gas will not be needed. From (7.1.7) we compute

$$u_r = \frac{\partial \phi}{\partial r} = -U\left(1 - \frac{R^3}{r^3}\right)\cos\theta, \tag{7.1.8}$$

$$u_\theta = \frac{1}{r}\frac{\partial \phi}{\partial \theta} = U\sin\theta\left(1 + \frac{R^3}{2r^3}\right), \tag{7.1.9}$$

$$\frac{\partial u_n}{\partial n} = \frac{\partial u_r}{\partial r} = -\frac{3UR^3}{r^4}\cos\theta \tag{7.1.10}$$

31

The functions (7.1.8), (7.1.9) and (7.1.10) enter into the normal stress balance at $r = R\left(1 + s\theta^2\right)$. This balance is to be satisfied near the stagnation point, for small θ, neglecting terms that go to zero faster than θ^2. At the free surface,

$$u_r = -U\left\{1 - \frac{1}{\left(1 + s\theta^2\right)^3}\right\} = -3Us\theta^2, \quad u_\theta = \frac{3}{2}U\theta,$$

$$\frac{\partial u_n}{\partial n} = -\frac{3U\left(1 - \frac{\theta^2}{2}\right)}{R\left(1 + s\theta^2\right)^4} = -\frac{3U}{R}\left\{1 - \left(4s + \frac{1}{2}\right)\theta^2\right\}, \tag{7.1.11}$$

$$u_r^2 = 0, \tag{7.1.12}$$

$$u_\theta^2 = \frac{9}{4}U^2\theta^2, \tag{7.1.13}$$

$$h = R - r\cos\theta = R - R\left(1 + s\theta^2\right)\left(1 - \frac{\theta^2}{2}\right) = R\left(\frac{1}{2} - s\right)\theta^2. \tag{7.1.14}$$

The motion of the gas in the bubble is not known but it enters into (7.1.6) as the coefficient of ρ_G and μ_G, which are small relative to the corresponding liquid terms. Evaluating (7.1.2) and (7.1.3) on the free surface, with gas motion zero, we obtain

$$\Gamma = -\frac{9}{8}\rho U^2\theta^2 + \rho\frac{U^2}{2}, \tag{7.1.15}$$

$$\Gamma_G = C_G. \tag{7.1.16}$$

Using (7.1.11) through (7.1.16), we may rewrite (7.1.6) as

$$\begin{aligned}
0 &= -C_G + \Gamma + \rho gh - 2\mu\frac{\partial u_r}{\partial r} + \frac{2\sigma}{r} \\
&= -C_G + \frac{\rho U^2}{2} - \frac{9}{8}\rho U^2\theta^2 + \rho gR\left(\frac{1}{2} - s\right)\theta^2 \\
&\quad + \frac{6\mu U}{R}\left\{1 - \left(4s + \frac{1}{2}\right)\theta^2\right\} + \frac{2\sigma}{R}\left(1 - s\theta^2\right).
\end{aligned} \tag{7.1.17}$$

The constant terms vanish:

$$C_G = \frac{\rho U^2}{2} + \frac{6\mu U}{R} + \frac{2\sigma}{R}. \tag{7.1.18}$$

The coefficient of θ^2 also vanishes:

$$\frac{9}{8}\rho U^2 + \frac{3\mu U}{R} + \frac{24\mu Us}{R} = \rho g\frac{R}{2} - s\left(\rho gR + \frac{2\sigma}{R}\right). \tag{7.1.19}$$

Surface tension, which balances the static pressure difference in a sphere or spherical cap, enters the formula for the velocity only when the axisymmetric cap is not spherical. When the spherical cap is perfectly spherical, as in the case treated by Davies and Taylor 1950, $s = 0$ and

$$U = -\frac{4}{3}\frac{\nu}{R} + \sqrt{\frac{4}{9}gR + \frac{16}{9}\frac{\nu^2}{R^2}}. \tag{7.1.20}$$

Equation (7.1.20) shows the viscosity slows the rise velocity; when the viscosity is much larger than gravity

$$U = \frac{1}{6}\frac{gR^2}{\nu}. \tag{7.1.21}$$

which is the velocity of a rising sphere computed by Moore 1959 from viscous potential flow balancing the drag with the buoyant weight.

The general solution of (7.1.19) with $D = 2R$ is

$$\frac{U}{\sqrt{gD}} = -\frac{8}{3}\frac{\nu\left(1 + 8s\right)}{\sqrt{gD^3}} + \frac{\sqrt{2}}{3}\left[1 - 2s - \frac{16s\sigma}{\rho gD^2} + \frac{32\nu^2}{gD^3}\left(1 + 8s\right)^2\right]^{1/2}. \tag{7.1.22}$$

32

It is convenient to write (7.1.22) in a dimensionless form

$$Fr = -\frac{8\,(1+8s)}{3\Re_G} + \frac{\sqrt{2}}{3}\left[1 - 2s - \frac{16s}{E\ddot{o}} + \frac{32}{\Re_G^2}\left(1+8s\right)^2\right]^{1/2},\tag{7.1.23}$$

where

$$Fr = \frac{U}{\sqrt{gD}} \qquad \text{Froude number,}$$

$$\Re_G = \frac{\sqrt{gD^3}}{\nu} \qquad \text{gravity Reynolds number,}$$

$$E\ddot{o} = \frac{\rho g D^2}{\sigma} \qquad \text{Eötvös number.}$$

These three parameters are the only ones that enter into correlations for the rise velocity of long bubbles in round pipes (Wallis 1969, Viana, Pardo, Yänez, Trallero and Joseph 2002).

It is of interest to consider different effects entering into the formula for the rise velocity U given by (7.1.22). The Davies and Taylor formula

$$U = \frac{\sqrt{2}}{3}\sqrt{gD}\tag{7.1.24}$$

arises from (7.1.22) when $\nu = \sigma = s = 0$. Recall that $s = r''(0)/D$ represents the difference from an undeformed spherical cap. When $s = 0$ the cap is exactly spherical; when $s < 0$ the nose of the cap is more pointed than the spherical cap and when $s > 0$ the nose is blunter than a sphere. The Davies-Taylor formula (7.1.24) arising from (7.1.22) in the asymptotic limit for large values of $\Re_G$ and $E\ddot{o}$

$$U = \frac{\sqrt{2}}{3}\left(1 - 2s\right)\sqrt{gD}\tag{7.1.25}$$

holds only when $s = 0$.

Unfortunately the analysis does not give the value of s; the shape of the nose is given when U is known, or if s is known then U is predicted. A more satisfying result would need to relax the assumption that the velocity potential (7.1.7) does not change when the spherical cap is not exactly spherical. This kind of perturbation analysis requires global data and is well beyond what can at present be obtained by analysis. A formula (8.2.39) for an ellipsoidal bubble, replacing (7.1.23), was derived by Funada et al 2004 and in §8.2.

7.2 Experiments

A review of experiments on the rise of spherical cap bubbles prior to 1973 together with an excellent collection of photographs can be found in the paper by Wegener and Parlange 1973. Reviews treating rising bubbles of all types were presented by Harper 1972 and Bhaga and Webber 1981.

The comparison of the prediction (7.1.23) of the rise velocity of a sperical cap bubble arising from the application of viscous potential flow is unambiguous when the deviation s from sphericity vanishes. There are two cases in which $s = 0$; according to the analysis of Davies and Taylor 1950, the spherical cap which arises for large bubbles is one case; the other case includes the rise of small bubbles, or bubbles with large surface tension, which was considered by Levich 1949, and Moore 1959 and 1963. In the first the sphericity arises from dynamics alone and the effects of surface tension on the spherical cap is negligible. In the case of small bubbles, or bubbles moving very slowly, surface tension can be important in keeping the bubble spherical, but the effect then of surface tension is absorbed totally by the pressure drop $[[p]] = 2\sigma/R$, as in (7.1.18), and does not enter the dynamics. The effects of surface tension on the rise velocity are associated with the deviation from sphericity; it is a shape effect since the net force and moment on a smooth bubble due to surface forces are zero (Hesla, Huang and Joseph 1993).

An efficient description of the effects affecting the deformation and rise velocity of gas bubbles in stagnant liquids can be carried out in terms of dimensionless parameters. The formulas (7.1.23) expresses a functional relation between three parameters: the Froude number, the gravity Reynolds number $\Re_G$ and the Eötvös number $E\ddot{o}$; these three parameters completely describe the rise velocity of Taylor bubbles, which are long gas bubbles capped by a spherical cap rising in tubes filled with stagnant liquid which were discussed in the Davies-Taylor paper. Viana, Pardo, Yänez, Trallero and Joseph, 2002 correlated all the published data, 262 experiments, on

the rise velocity, Fr, of Taylor bubbles in round pipes with a highly accurate rational fraction of power of the parameters $\Re_G$ and $E\ddot{o}$; a graph of the data processed by them is shown in figure 7.2.

Other parameters are frequently used for the description of the rise velocity; these are

$$\left.\begin{array}{rcll} C_D & = & \dfrac{4}{3}\dfrac{gd_e}{U^2} & \text{drag coefficient,} \\[2mm] R_e & = & \dfrac{Ud_e}{\nu} & \text{Reynolds number,} \\[2mm] W & = & \dfrac{\rho U^2 d_e}{\sigma} & \text{Weber number,} \\[2mm] M & = & \dfrac{g\mu^4}{\rho\sigma^3} & \text{Morton number.} \end{array}\right\} \tag{7.2.1}$$
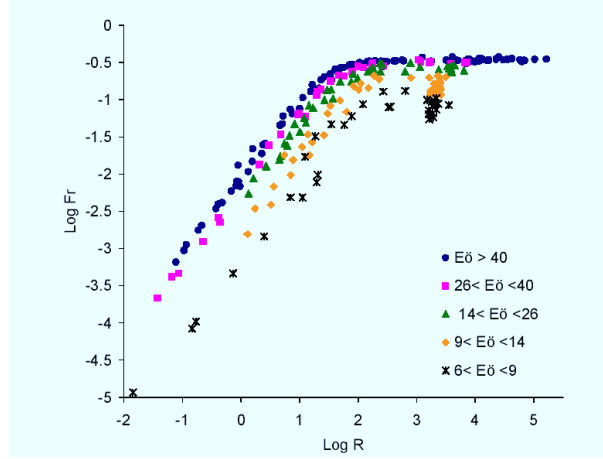
Fig. 7.2. (After Viana et al. 2002). Rise velocity Fr vs. $Log\Re_G$ for different Eötvös numbers for all published experiments on the rise velocity of Taylor bubbles in round pipes. The rise velocity is independent of $E\ddot{o}$ when $E\ddot{o} > 40$. //Note that this figure is ./8/fig3-3.eps. The title of the x axis needs to be fixed (Log R_G). //

The choice of effective diameter is important; two choices are made here: $d_e = D$ where d_e is the sphere diameter or the diameter of the spherical cap, $d_e = \bar{d}$, where $\bar{d}$ is volume equivalent diameter defined by $V = \dfrac{\pi}{6}\bar{d}^3$, and Reynolds numbers by $R_e = \dfrac{UD}{\nu}$, $\bar{R}_e = \dfrac{U\bar{d}}{\nu}$ based on D and $\bar{d}$. Any pair of independent dimensionless parameters determine all the others in steady flow; as in (7.1.23), a dimensionless parameter involving U may be expressed in terms of two other independent parameters.

It is convenient to compare the theory developed here with experiments in which the surface tension, or parameters in which the surface tension is a factor, affect the rise velocity and those for which these parameters are not important; for example, according to figure 7.2, Fr is a function of $\Re_G$ alone when $E\ddot{o} > 40$.

In the case of a spherical cap bubble, limitations on the bubble size arise from several sources and restrict the values of the parameters which may be observed. Grace, Wairegi and Brophy 1978 reported the maximum volume of air in bubbles that remain intact in five different liquids in a wide tank but did not identify which of the five were spherical cap. Batchelor 1987 looked at these data in terms of a stability theory which limits the maximum size bubbles. A numerical study by Bolton-Stone, Robinson and Blake 1995 suggests that spherical cap bubbles arise only when the Eötvös number based on an equivalent spherical radius is less than about 32. For higher values of $E\ddot{o}$ an unstable toroidal bubble is formed before breakup.

Harper 1972 makes a distinction between high- and low-Morton-number (M) liquids. He characterizes the high-M liquids as those for which C_D decreases monotonically with $\bar{R}_e$ as in figure 7.3, and the low-M liquids as those for which C_D vs. $\bar{R}_e$ has a minimum. Bhaga and Weber 1981 identify this critical value as $M = 4 \times 10^{-3}$; a low-M liquid response is identified by the solid circle data points in figure 7.3.

The monotonic curve through the high-M open symbol points in figure 7.3 is described by an empirical formula

$$\bar{C}_D = \left[(2.67)^{0.9} + \left(16/\bar{R}_e\right)^{0.9}\right]^{1/0.9} \tag{7.2.2}$$

34
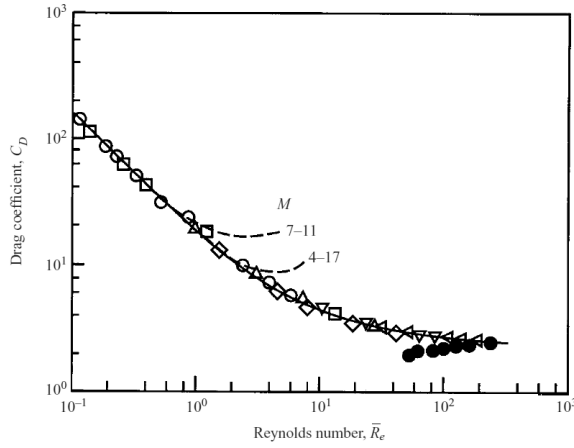
Fig. 7.3. (After figure 7 in Bhaga & Weber 1981.) $\bar{C}_D$ $(= 4g\bar{d}/U^2)$ vs. $\bar{R}_e$ $(= U\bar{d}/\nu)$. Taylor & Acrivos 1964 (- - -); $\bar{C}_D$ given by (7.2.2) (—); $M = 1.64 \times 10^{-3}$ ($\bullet$).

in which $\bar{C}_D$ is determined by $\bar{R}_e$ alone. The shapes of the bubbles change from spheres to spherical cap bubbles as $\bar{R}_e$ increases; since $\bar{C}_D$ and $\bar{R}_e$ are defined here using the volume equivalent diameter $\bar{d}$, which decreases from the sphere diameter D at low $\bar{R}_e$ to a value $\bar{d} < D$ for a spherical cap bubble which can be estimated from the results of Davies and Taylor 1950 and those given here.

Consider the case in which the deviation from sphericity $s = 0$. In this case equation (7.1.20) holds. We may rewrite this equation as a drag relation

$$C_D = 6 + 32/R_e, \tag{7.2.3}$$

where $C_D = \dfrac{4}{3}\dfrac{gD}{U^3}$, $R_e = \dfrac{UD}{\nu}$ and $D = 2R$ is the diameter of the spherical cap. The large-R_e limit of (7.2.3), $C_D = 6$ is the value of drag coefficient which was established in the brilliant experiments by Davies and Taylor 1950. The asymptotic large-$\bar{R}_e$ limit of (7.2.2) is $\bar{C}_D = 2.67$. These two limits should be the same, hence

$$\frac{\bar{C}_D}{C_D} = \frac{2.67}{6} = \frac{\bar{d}}{D}.$$

If this limit is a spherical cap bubble the volume equivalent diameter is

$$\bar{d} = 0.445D \tag{7.2.4}$$

of the spherical cap diameter $d = 2R$. The ratio of the volume of the spherical cap bubble to the volume of a sphere of radius $R = D/2$ is

$$\bar{V} = \frac{\bar{d}^3 V}{D^3} = 0.0881. \tag{7.2.5}$$

The volume of the spherical cap bubble in this computation is a little less than $1/10$ the value of the volume of the sphere from which it is cut.

In comparing (7.2.2) and (7.2.3) we must convert $\bar{R}_e$ to R_e and though this cannot be done generally, it can be done empirically for the limiting case of large R_e for which $R_e = 0.445\bar{R}_e$. In figure 7.4 we compare the empirical relation (7.2.2) to a rescaled plot of (7.2.3)

$$\tilde{C}_D = 0.445\left(6 + \frac{32}{R_e}\right). \tag{7.2.6}$$

The agreement between (7.2.6) and (7.2.2) is spectacular but possibly misleading since the relation between $\bar{d}$ and D is not generally known.

A direct comparison of (7.2.3) with numerical results is tentative because the spherical cap bubble limit is beyond the capabilities of the numerical methods which have been applied to the problem. The calculations of Ryskin and Leal 1984 seem reliable and they work well for Weber and Reynolds numbers at which the spheres are greatly distorted. Their figure 1 is a plot of $\bar{C}_D$ vs. $\bar{W}$ with $\bar{R}_e$ as a parameter which is in agreement with

35
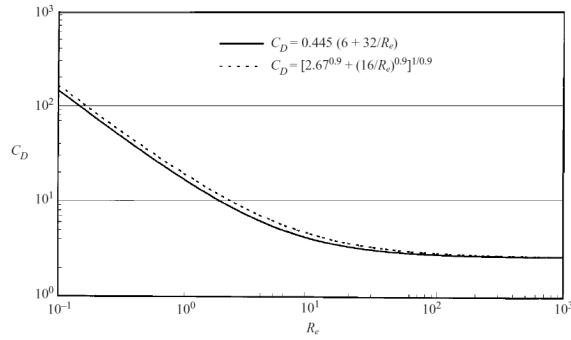
Fig. 7.4. Comparison of the empirical drag law (7.2.2) with the theoretical drag law (7.2.6) scaled by the factor 0.445 required to match the data in figure 7.3 with the experiments of Davies & Taylor (1950) at large R_e.

(7.2.2) for $\bar{R}_e < 20$. The empirical formula could not be tested for the large values of W for which the cap bubbles arise but the $\bar{R}_e$ variation for smaller values of $\bar{W}$ is also consistent with (7.2.2).

The comparison of theory and experiment for the case when the deviation s from sphericity is not zero is complicated. In this case the curvature of the nose of the bubble is different from the spherical radius R used in our calculations and those of Davies and Taylor. We have already noted that the analysis leading to s neglects some of the changes in the potential function which arise from the change in the shape of the domain. The computation or measurement of s will not be undertaken here but the comparison mode in figures 1 and 2 of the paper by Miksis *et al* 1982 for distorted bubbles in lenticular shape, but far from spherical caps, may point the way.

7.3 Conclusions

Viscous potential flow is as a potential flow solution of the Navier-Stokes equations in which the vorticity vanishes and no-slip conditions at interface are not enforced. This solution does not require that the viscosity be put to zero and it is not a good idea to put it to zero. Using this theory, we extended the analysis of Davies and Taylor 1950 of the spherical cap bubble to include effects of viscosity, surface tension and the deviation of the bubble nose from sphericity. The result of these analyses are then expressed by the rise velocity formula (7.1.22) and the drag formula (7.2.3). These formulae are in good agreement with experiments of Bhaga and Weber 1981 at the high Morton numbers for which the cap bubbles arise, with the caveat that the conversion of the spherical radius to an effective volume equivalent radius is ambiguous. The possible effects of vorticity boundary layers on the rise velocity have not been analyzed here; it is not possible to use the same methods that work for spherical gas bubbles and it is unlikely that the results of such an analysis would greatly improve the agreement between theory and experiments documented here.

36

8

Ellipsoidal model of the rise of a Taylor bubble in a round tube

The rise velocity of long gas bubbles (Taylor bubbles) in round tubes is modeled by an ovary ellipsoidal cap bubble rising in an irrotational flow of a viscous liquid. The analysis leads to an expression for the rise velocity which depends on the aspect ratio of the model ellipsoid and the Reynolds and Eötvös numbers. The aspect ratio of the best ellipsoid is selected to give the same rise velocity as the Taylor bubble at given values of the Eötvös and Reynolds numbers. The analysis leads to a prediction of the shape of the ovary ellipsoid which rises with same velocity as the Taylor bubble.

8.1 Introduction

The correlations given by Viana *et al.* (2003) convert all the published data on the normalized rise velocity $F_r = U/(gD)^{1/2}$ into analytic expressions for the Froude velocity versus buoyancy Reynolds number, $R_G = \left(D^3 g \left(\rho_l - \rho_g\right) \rho_l\right)^{1/2}/\mu$ for fixed ranges of the Eötvös number, $E_o = g\rho_l D^2/\sigma$ where D is the pipe diameter, ρ_l, ρ_g and σ are densities and surface tension. Their plots give rise to power laws in E_o; the composition of these separate power laws emerge as bi-power laws for two separate flow regions for large and small buoyancy Reynolds. For large R_G (> 200) they find that

$$F_r = 0.34/\left(1 + 3805/E_o^{3.06}\right)^{0.58}. \tag{8.1.1}$$

For small R_G (< 10) they find

$$F_r = \frac{9.494 \times 10^{-3}}{\left(1 + 6197/E_o^{2.561}\right)^{0.5793}} R_G^{1.026}. \tag{8.1.2}$$

The flat region for high buoyancy Reynolds number and sloped region for low buoyancy Reynolds number is separated by a transition region ($10 < R_G < 200$) which they describe by fitting the data to a logistic dose curve. Repeated application of logistic dose curves lead to a composition of rational fractions of rational fractions of power laws. This leads to the following universal correlation:

$$F_r = \frac{0.34/\left(1 + 3805/E_o^{3.06}\right)^{0.58}}{\left(1 + \left(\dfrac{R_G}{31.08}\left(1 + \dfrac{778.76}{E_o^{1.96}}\right)^{-0.49}\right)^{-1.45\left(1 + \frac{7.22 \times 10^{13}}{E_o^{9.93}}\right)^{0.094}}\right)^{0.71\left(1 + \frac{7.22 \times 10^{13}}{E_o^{9.93}}\right)^{-0.094}}}. \tag{8.1.3}$$

The performance of the universal correlation (8.1.3) is evaluated in figure 8.1 where the values predicted by (8.1.3) are compared to the experiments. Almost all of the values fall within the 20% error line and most of the data is within 10% of predicted values.

The formula (8.1.3) solves the problem of the rise velocity of Taylor bubbles in round pipes. This formula arises from processing data and not from flow fundamentals; one might say that the problem of the rise velocity has been solved without understanding.
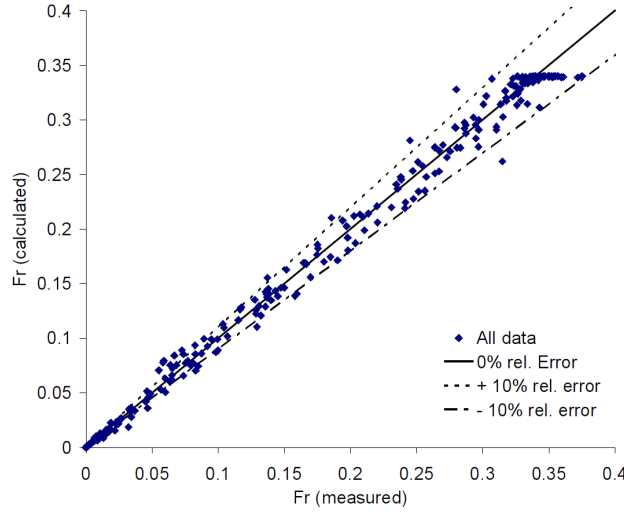
Fig. 8.1. F_r predicted from (8.1.3) vs. experimental data ($E_o > 6$).

8.1.1 Unexplained and paradoxical features

The teaching of fluid mechanics would lead one to believe that a bubble rising steadily in a liquid is in a balance of buoyant weight and drag. It is natural to think that the buoyant weight is proportional to the volume of gas, but the accurate formula (8.1.3) does not depend on the length of the bubble; this requires explanation.

Even the theoretical results are mysterious. The rise velocity U of the spherical cap bubble at high Reynolds number is accurately determined from a potential flow analysis of motion in an inviscid fluid by Davies & Taylor (1950) and in a viscous fluid by Joseph (2003a). Analysis of the rise velocity of Taylor bubbles in inviscid fluids based on shape of the bubble nose was given first by Dumitrescue (1943) and then by Davies & Taylor (1950).

In the analysis of Joseph (2003), given in chapter 7, it was assumed that the bubble nose shape was given by

$$r(\theta) = R\left(1 + s\theta^2\right), \tag{8.1.4}$$

where $s = r''(0)/2R$ is the deviation of the free surface from perfect sphericity.

The dependence of (8.1.4) on terms proportional to s is incomplete because the potential solution for a sphere and the curvature for a sphere were not perturbed. A complete formula (8.2.39) replacing (8.1.4) is derived in section 8.2.

The Davies-Taylor 1950 result arises when all other effects vanish; if s alone is zero,

$$\frac{U}{\sqrt{gD}} = -\frac{8}{3}\frac{\nu}{\sqrt{gD^3}} + \frac{\sqrt{2}}{3}\left[1 + \frac{32\nu^2}{gD^3}\right]^{1/2} \tag{8.1.5}$$

showing that viscosity slows the rise velocity. Equation (8.1.5) gives rise to a hyperbolic drag law

$$C_D = 6 + 32/R \tag{8.1.6}$$

which agrees with data on the rise of spherical cap bubbles given by Bhaga & Weber (1981).

It is unusual that the drag on the cap bubble plays no role in the analysis leading to (8.1.5). Batchelor (1967) notes that

That retarding force is evidently independent of Reynolds number, and the rate of dissipation of mechanical energy is independent of viscosity, implying that stresses due to turbulent transfer of momentum are controlling the flow pattern in the wake of the bubble.

This citation raises another anomalous feature about the rise of cap bubbles and Taylor bubbles relating to the wake. An examination of rise velocity from Bhaga & Weber (1981) and the study of Taylor bubbles in Viana *et al.* (2003) do not support the idea of turbulent transfer. The wake may be very turbulent as is true in water or apparently smooth and laminar as is true for bubbles rising in viscous oils but this feature does not enter into any of the formulas for the rise velocity, empirical as in (8.1.3) or theoretical as in (8.1.5).

A related paradoxical property is that the Taylor bubble rise velocity does not depend on how the gas is

38
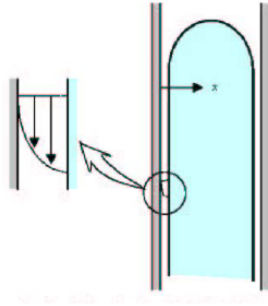
Fig. 8.2. Drainage at the wall of a rising Taylor bubble. If U is added to this system the wall moves and the bubble is stationary.

introduced into the pipe. In the Davies-Taylor experiments the bubble column is open to the gas. In other experiments the gas is injected into a column whose bottom is closed.

It can be said, despite successes, a good understanding of the fluid mechanics of the rise of cap bubbles and Taylor bubbles is not yet available.

8.1.2 Drainage

Many of the paradoxical features of the rise of Taylor bubbles can be explained by drainage in figure 8.2. The liquid at the wall drains under gravity with no pressure gradient. If the liquid is put into motion by a pressure gradient the gas bubble will deform and the film flow will not be governed by (8.1.7); the drain equation is

$$\frac{\mu}{r}\frac{\mathrm{d}}{\mathrm{d}r}\left(r\frac{\mathrm{d}u}{\mathrm{d}r}\right) = \rho_l g \tag{8.1.7}$$

subject to no slip at the wall and no shear at the bubble surface.

It can be argued that the cylindrical part of the long bubble is effectively not displacing liquid since the pressure does not vary along the cylinder. In this case buoyant volume entering into the equation *buoyancy = drag* would be the vaguely defined hemisphere poking into the liquid at top. The source of drag is unclear; since shear stresses do not enter the drag ought to be determined by the vertical projections of normal stresses all around the bubble. This kind of analysis has not appeared in the literature. A different kind of analysis, depending on the shape of the bubble and sidewall drainage has been applied. This kind of analysis leads ultimately to a formula for the rise velocity of the bubble nose. Apparently the shape of the bubble nose is an index of the underlying drag balance.

8.1.3 Brown's 1965 analysis of drainage

Brown (1965) put forward a model of the rise velocity of large gas bubbles in tubes. A similar model was given by Batchelor (1967). There are two elements for this model.

(1) The rise velocity is assumed to be given by $C\sqrt{gR_\delta}$ where C (= 0.494) is an empirical constant and $R_\delta = R - \delta$ is the bubble radius, R is the tube radius and δ is the unknown film thickness.

(2) It is assumed that the fluid drains in a falling film of constant thickness δ. The film thickness is determined by conserving mass: the liquid displaced by the rising bubble must balance the liquid draining at the wall.

After equating two different expressions for the rise velocity arising from (1) and (2), Brown finds that

$$U = 0.35V\sqrt{1 - \frac{2\left(\sqrt{1+\psi}-1\right)}{\psi}} \tag{8.1.8}$$

where

$$\psi = \left(14.5\Re^2\right)^{1/3}, \quad \Re = VD/\nu, \quad V = \sqrt{gD}. \tag{8.1.9}$$

The expression for the rise velocity (8.1.8) does not account for effects of surface tension which are negligible
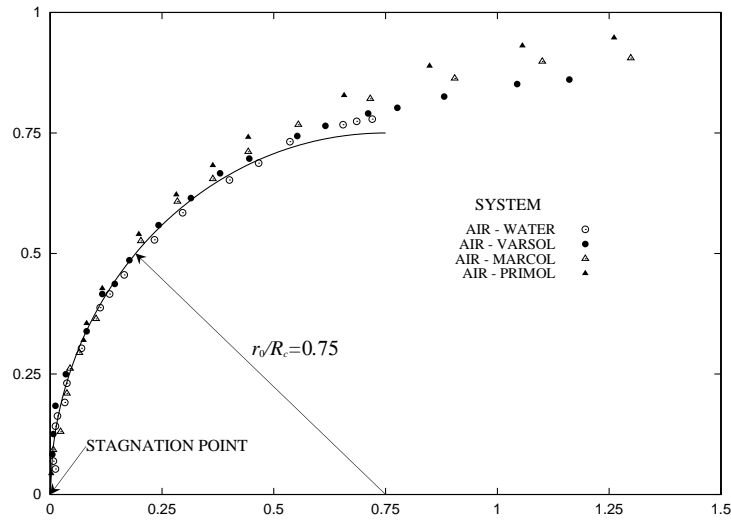
Fig. 8.3. (After Brown 1965). The profile of the cap of Taylor bubbles. The nose region is spherical with a radius r_0. For all the fluids, $r_0/R_c = 0.75$. The viscosities of water, varsol, marcol, and primol apparently are 0.977, 0.942, 19.42 and 142.3 mPa s respectively.

when the bubble radius is large. The expression is in moderately good agreement with data, but not nearly as good as the correlation formula (8.1.3).

The rise velocity $\sqrt{gR_\delta}$ is still determined by the bubble shape, but that shape is altered by drainage.

8.1.4 Viscous potential flow

We have already mentioned that the correlation formula (8.1.3) accurately predicts the rise velocity and further improvement cannot be expected from modeling. Our understanding of the fluid mechanics under way is however far from complete. When surface tension is neglected the formula (8.1.5) extends the results of Dumitrescue (1943) and Davies & Taylor (1950) from inviscid fluids to viscous fluids by assuming that the cap of the bubble remains spherical, even at finite Reynolds number. The same extension to include the effects of viscosity in the formula for the rise velocity based on potential flow at the nose should be possible for Taylor bubbles if the nose remains spherical in viscous fluids. Brown says that figure 8.3 (note that he used R_c for $R - \delta$, which is R_δ in our nomenclature.)

"... indicates that although the cavity shapes are different in the transition region, they are remarkably similar in the nose region. The second interesting fact ... is that the frontal radius of the cavity in normalized coordinates ($R_c = R - \delta$) which is the same for all liquids, is 0.75, the same value as was obtained in the analysis of bubbles in inviscid liquids."

The scatter in the data plotted in figure 8.3 and the data in the transition can be fit even better by the cap of an ovary ellipsoid which is nearly spherical (figure 8.9) arising from the analysis given in section 8.2.

The effect of surface tension is to retard the rise velocity of Taylor bubbles in round tubes. The universal correlation (8.1.3) shows that the rise velocity decreases as the Eötvös number $E_o = g\rho_l D^2/\sigma$ decreases, for ever smaller values of D^2/σ. In fact these kinds of bubbles, with large tensions in small tubes, do not rise; they stick in the pipe preventing draining. If the radius of a stagnant bubble $R = 2\sigma/\Delta p$ with the same pressure difference Δp as in the Taylor bubble, is larger than the tube radius, it will plug the pipe. White & Beardmore (1962) said that the bubble will not rise when $E_o < 4$. This can be compared with the values 3.36 given by Hattori (1935), 3.37 given by Bretherton (1961), 5.8 given by Barr (1926), and 4 given by Gibson (1913).

A very convincing set of experiments showing the effect of drainage is reported for "Taylor bubbles in miniaturized circular and noncircular channels" by Bi & Zhao (2001). They showed that for triangular and rectangular channels, elongated bubbles always rose upward even though the hydraulic diameter of the tube was as small as 0.866 mm, whereas in circular tubes the bubble motion stopped when $d \leq 2.9$ mm. They did not offer an explanation but the reason is that surface tension cannot close the sharp corners where drainage can occur.
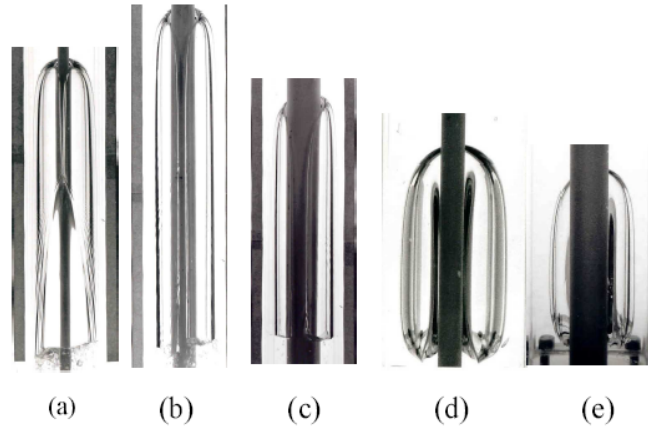
Fig. 8.4. Photographs (unpublished, courtesy of F.Viana & R.Pardo) of Taylor bubbles rising in concentric annular space of 76.2 mm inside diameter pipe and different rod diameter (ID) filled with different viscous liquids: a) Water (1 mPa s, 997 kg/m^3), ID=12.7 mm; b) Water, ID=25.4 mm; c) Water, ID=38.1 mm; d) Silicone oil (1300 mPa s, 970 kg/m^3), ID=12.7 mm; e) Silicone oil (1300 mPa s, 970 kg/m^3), ID=25.4 mm. The gas bubbles do not wrap all the way around the inner cylinder; a channel is opened for liquid drainage.
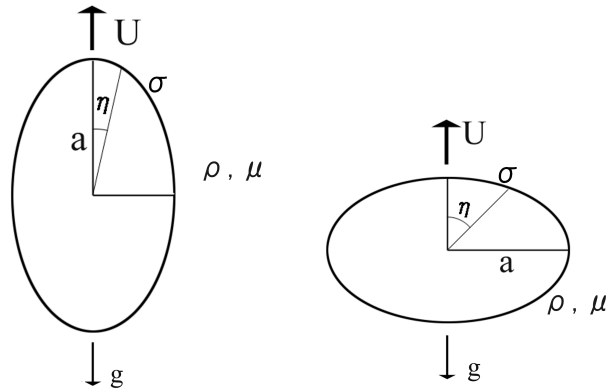
Fig. 8.5. An ellipsoid bubble moving with a uniform velocity U in the z direction of Cartesian coordinates (x, y, z). An ovary ellipsoid is depicted in the left-hand side and a planetary ellipsoid is in the right-hand side, which are of the major semiaxis a, the minor semiaxis b, the aspect ratio $e = c/a$, $c^2 = a^2 - b^2$, and in a liquid (water) of density ρ, viscosity μ, with the surface tension σ at the surface given by $\xi = \xi_0$ and under the acceleration due to gravity g.

8.2 Ellipsoidal bubbles

Grace & Harrison (1967) studied rise of ellipsoidal bubble in an inviscid liquid. They sought to explain the influence of bubble shape on the rise velocity and concluded that elliptical cap and ovary ellipsoidal bubbles rise faster than the corresponding circular-cap and spherical-cap bubbles. They cited experimental data which they claim support their results. They say that "... bubbles take up elliptical shapes if they enclose a surface (e.g. a rod)." This statement is not correct because bubbles rising in the presence of a central rod are usually not axisymmetric as can be seen in figure 8.4.

In this chapter we shall obtain expressions for the rise velocity of ovary and planetary ellipsoids. The ovary ellipsoid looks more like a long bubble than a planetary ellipsoid (figure 8.5). There is no way that the planetary ellipsoid can be fit to the data given by Viana *et al.* (2003), but the ovary ellipsoid can be made to fit Viana's data with one shape parameter for all cases. This is very surprising, since the Taylor bubble is not thought to be ellipsoidal and the dynamics of these bubbles is controlled by sidewall drainage which is entirely neglected in the following potential flow analysis of the rise of ellipsoidal bubbles in a viscous liquid.

Ovary and planetary ellipsoidal bubbles are shown in figure 8.5. We will be led by the analysis to cases in which the ovary ellipsoids are nearly spherical with $D = 2a$.

For axisymmetric flows of incompressible fluid around the ellipsoid of revolution, we can have the stream function and the velocity potential, then we have the solution which satisfies the kinematic condition at the surface of the bubble and the normal stress balance there which contains the viscous normal stress based on viscous potential flow.

8.2.1 Ovary ellipsoid

In an ellipsoidal frame (ξ, η, φ) on the ovary ellipsoid bubble moving with a uniform velocity U in a liquid, we have the stream function ψ and the velocity potential ϕ for axisymmetric flow

$$\psi = \frac{1}{2} U c^2 \sin^2 \eta \left[\sinh^2 \xi - \frac{b^2}{a^2 K} \left(\cosh \xi + \sinh^2 \xi \ln \tanh \frac{\xi}{2} \right) \right], \tag{8.2.1}$$

$$\phi = U c \cos \eta \left[\cosh \xi - \frac{b^2}{a^2 K} \left(1 + \cosh \xi \ln \tanh \frac{\xi}{2} \right) \right], \tag{8.2.2}$$

with $c^2 = a^2 - b^2$, $e = c/a$ and K:

$$\begin{aligned} K &= e^2 \left[\frac{a}{c} + \frac{b^2}{c^2} \ln \frac{a+b-c}{a+b+c} \right] = \frac{1}{\cosh \xi_0} + \tanh^2 \xi_0 \ln \tanh \xi_0/2 \\ &= e + \left(1 - e^2 \right) \tanh^{-1}(e). \end{aligned} \tag{8.2.3}$$

(In this case, we take $z = c \cosh \xi \cos \eta$, $\varpi = c \sinh \xi \sin \eta$, $x = \varpi \cos \varphi$ and $y = \varpi \sin \varphi$; $a = c \cosh \xi_0$ and $b = c \sinh \xi_0$.) The stream function (8.2.1) has been derived based on the article in §16.57 of Milne-Thomson's book (Milne-Thomson (1996)). The velocity $\boldsymbol{u} = (u_\xi, u_\eta)$ is expressed as

$$\begin{aligned} u_\xi &= -\frac{1}{J} \frac{\partial \phi}{\partial \xi} = -\frac{1}{\varpi J} \frac{\partial \psi}{\partial \eta} \\ &= -\frac{Uc}{J} \cos \eta \left[\sinh \xi - \frac{b^2}{a^2 K} \left(\coth \xi + \sinh \xi \ln \tanh \xi/2 \right) \right], \end{aligned} \tag{8.2.4}$$

$$\begin{aligned} u_\eta &= -\frac{1}{J} \frac{\partial \phi}{\partial \eta} = \frac{1}{J \varpi} \frac{\partial \psi}{\partial \xi} = \frac{Uc}{J} \sin \eta \left[\cosh \xi - \frac{b^2}{a^2 K} \left(1 + \cosh \xi \ln \tanh \xi/2 \right) \right] \\ &\equiv \frac{Uc \sin \eta}{J} f_1(\xi), \end{aligned} \tag{8.2.5}$$

$$\begin{aligned} \frac{1}{J} \frac{\partial u_\xi}{\partial \xi} &= -\frac{1}{J^2} \frac{\partial^2 \phi}{\partial \xi^2} + \frac{1}{J^3} \frac{\partial J}{\partial \xi} \frac{\partial \phi}{\partial \xi} \\ &= -\frac{Uc}{J^2} \cos \eta \left[\cosh \xi - \frac{b^2}{a^2 K} \left(1 - \frac{1}{\sinh^2 \xi} + \cosh \xi \ln \tanh \xi/2 \right) \right] - \frac{u_\xi}{J^2} \frac{\partial J}{\partial \xi} \\ &= -\frac{Uc \cos \eta}{J^2} f_2(\xi) - \frac{u_\xi}{J^2} \frac{\partial J}{\partial \xi}, \end{aligned} \tag{8.2.6}$$

$$\begin{aligned} \left(\frac{1}{J} \frac{\partial u_\xi}{\partial \xi} \right)_{\xi_0} &= -Uc \cos \eta \left[\frac{1}{J^2} \left[\cosh \xi - \frac{b^2}{a^2 K} \left(1 - \frac{1}{\sinh^2 \xi} + \cosh \xi \ln \tanh \xi/2 \right) \right] \right]_{\xi_0} \\ &\equiv -\frac{Uc \cos \eta}{J_0^2} f_2(\xi_0), \end{aligned} \tag{8.2.7}$$

with

$$\left. \begin{aligned} J^2 &= c^2 \sinh^2 \xi + c^2 \sin^2 \eta, \quad J_0 = (J)_{\xi_0}, \\ f_1(\xi_0) &= \cosh \xi_0 - \frac{b^2}{a^2 K} \left(1 + \cosh \xi_0 \ln \tanh \xi_0/2 \right) = \frac{e^2}{e + (1-e^2) \tanh^{-1}(e)} = f_1(e), \\ f_2(\xi_0) &= \cosh \xi_0 - \frac{b^2}{a^2 K} \left(1 - \frac{1}{\sinh^2 \xi_0} + \cosh \xi_0 \ln \tanh \xi_0/2 \right) = f_2(e) = 2 f_1(e). \end{aligned} \right\} \tag{8.2.8}$$

Following Joseph (2003a), Bernoulli function is given by his (1.2) and (1.3):

$$\frac{\rho |\boldsymbol{u}|^2}{2} + \Gamma = \frac{\rho U^2}{2}, \quad \frac{\rho_G |\boldsymbol{u}|^2}{2} + \Gamma_G = C_G. \tag{8.2.9}$$

42

Put $\rho_G |\boldsymbol{u}|^2 = 0$ in the gas. Then $\Gamma_G = C_G$ is constant. Boundary conditions at the surface of the ellipsoid (where $\xi = \xi_0$) are the kinematic condition and the normal stress balance

$$u_\xi = 0, \quad -[[\Gamma]] - [[\rho]]\, gh + [[2\mu \boldsymbol{n} \cdot \mathbf{D}[\boldsymbol{u}]]] \cdot \boldsymbol{n} = -\sigma \boldsymbol{\nabla} \cdot \boldsymbol{n}, \tag{8.2.10}$$

where $\Gamma = p + \rho gh$ as in Joseph 2003, the normal viscous stress $2\mu \boldsymbol{n} \cdot \mathbf{D}[\boldsymbol{u}] \cdot \boldsymbol{n}$ and the normal vector $\boldsymbol{n}$ satisfy the following relations:

$$[[\Gamma]] = \Gamma_G - \Gamma = C_G - \frac{\rho}{2}U^2 + \frac{\rho}{2}|\boldsymbol{u}|^2 = C_G - \frac{\rho}{2}U^2 + \frac{\rho}{2}(u_\eta)^2_{\xi_0}, \tag{8.2.11}$$

$$[[2\mu \boldsymbol{n} \cdot \mathbf{D}[\boldsymbol{u}]]] \cdot \boldsymbol{n} = -2\mu \left(\frac{1}{J}\frac{\partial u_\xi}{\partial \xi} + u_\eta \frac{c^2}{J^3}\cos\eta\sin\eta \right)_{\xi_0}, \tag{8.2.12}$$

$$\boldsymbol{\nabla} \cdot \boldsymbol{n} = \frac{\coth\xi_0}{J_0^3}\left(J_0^2 + c^2 \sinh^2\xi_0 \right). \tag{8.2.13}$$

The normal stress balance is then expressed as

$$-C_G + \frac{\rho}{2}U^2 - \frac{\rho}{2}(u_\eta)^2_{\xi_0} + \rho gh - 2\mu \left(\frac{1}{J}\frac{\partial u_\xi}{\partial \xi} + u_\eta \frac{c^2}{J^3}\cos\eta\sin\eta \right)_{\xi_0} = -\sigma \boldsymbol{\nabla} \cdot \boldsymbol{n}, \tag{8.2.14}$$

where the distance from the top of the ellipsoid bubble is

$$h = a\left(1 - \cos\eta\right) = c \cosh\xi_0 \left(1 - \cos\eta\right). \tag{8.2.15}$$

For small η, we have

$$\left. \begin{aligned}
J_0 &= c \sinh\xi_0 \left(1 + \frac{\eta^2}{2\sinh^2\xi_0} + O(\eta^4) \right), \\
h &= c \cosh\xi_0 \left[\frac{1}{2}\eta^2 + O(\eta^4) \right], \\
(u_\eta)_{\xi_0} &= \frac{U f_1(\xi_0)}{\sinh\xi_0}\left[\eta + O(\eta^3) \right], \\
\left(\frac{1}{J}\frac{\partial u_\xi}{\partial \xi} \right)_{\xi_0} &= -\frac{U f_2(\xi_0)}{c\sinh^2\xi_0}\left[1 - \left(\frac{1}{2} + \frac{1}{\sinh^2\xi_0} \right)\eta^2 + O(\eta^4) \right], \\
\boldsymbol{\nabla} \cdot \boldsymbol{n} &= \frac{2\cosh\xi_0}{c\sinh^2\xi_0}\left(1 - \frac{\eta^2}{\sinh^2\xi_0} + O(\eta^4) \right).
\end{aligned} \right\} \tag{8.2.16}$$

Substitution of (8.2.16) into the normal stress balance (8.2.14) leads to a formula for the ovary bubble:

$$-C_G + \frac{\rho}{2}U^2 - \frac{\rho}{2}(u_\eta)^2_{\xi_0} + \rho gh - 2\mu \left(\frac{1}{J}\frac{\partial u_\xi}{\partial \xi} + u_\eta \frac{c^2}{J^3}\cos\eta\sin\eta \right)_{\xi_0}$$
$$= -\sigma \frac{2\cosh\xi_0}{c\sinh^2\xi_0}\left(1 - \frac{\eta^2}{\sinh^2\xi_0} \right). \tag{8.2.17}$$

Thus, we have C_G in $O(1)$

$$C_G = \frac{\rho}{2}U^2 + \frac{2\mu U f_2(\xi_0)}{c\sinh^2\xi_0} + \sigma \frac{2\cosh\xi_0}{c\sinh^2\xi_0}, \tag{8.2.18}$$

and the following relation in $O(\eta^2)$

$$-\frac{\rho}{2}\frac{U^2 f_1^2(\xi_0)}{\sinh^2\xi_0} + \frac{\rho gc}{2}\cosh\xi_0 - \frac{2\mu U}{c\sinh^2\xi_0}\left[f_2(\xi_0)\left(\frac{1}{2} + \frac{1}{\sinh^2\xi_0} \right) + \frac{f_1(\xi_0)}{\sinh^2\xi_0} \right]$$
$$= \sigma \frac{2\cosh\xi_0}{c\sinh^4\xi_0}. \tag{8.2.19}$$

43

8.2.2 Planetary ellipsoid

In an ellipsoidal frame (ξ, η, φ) on the planetary ellipsoid bubble moving with a uniform velocity U in a liquid, we have the stream function ψ and the velocity potential ϕ for axisymmetric flow

$$\psi = \frac{1}{2}Uc^2 \sin^2 \eta \left[\cosh^2 \xi - \frac{\sinh \xi - \cosh^2 \xi \cot^{-1} \sinh \xi}{e\sqrt{1-e^2} - \sin^{-1} e} \right], \tag{8.2.20}$$

$$\phi = Uc \cos \eta \left[\sinh \xi - \frac{1 - \sinh \xi \cot^{-1} \sinh \xi}{e\sqrt{1-e^2} - \sin^{-1} e} \right], \tag{8.2.21}$$

where $c^2 = a^2 - b^2$ and $e = c/a$. (In this case, we take $z = c \sinh \xi \cos \eta$, $\varpi = c \cosh \xi \sin \eta$, $x = \varpi \cos \varphi$ and $y = \varpi \sin \varphi$; $a = c \cosh \xi_0$ and $b = c \sinh \xi_0$.) The velocity $\boldsymbol{u} = (u_\xi, u_\eta)$ is given by

$$u_\xi = -\frac{1}{J}\frac{\partial \phi}{\partial \xi} = -\frac{Uc}{J}\cos \eta \left[\cosh \xi - \frac{\tanh \xi - \cosh \xi \cot^{-1} \sinh \xi}{e\sqrt{1-e^2} - \sin^{-1} e} \right], \tag{8.2.22}$$

$$u_\eta = -\frac{1}{J}\frac{\partial \phi}{\partial \eta} = \frac{Uc}{J}\sin \eta \left[\sinh \xi - \frac{1 - \sinh \xi \cot^{-1} \sinh \xi}{e\sqrt{1-e^2} - \sin^{-1} e} \right] \equiv \frac{Uc \sin \eta}{J} f_1(\xi), \tag{8.2.23}$$

$$\begin{aligned}
\frac{1}{J}\frac{\partial u_\xi}{\partial \xi} &= -\frac{1}{J^2}\frac{\partial^2 \phi}{\partial \xi^2} + \frac{1}{J^3}\frac{\partial J}{\partial \xi}\frac{\partial \phi}{\partial \xi} \\
&= -\frac{Uc}{J^2}\cos \eta \left[\sinh \xi - \frac{1 + 1/\cosh^2 \xi - \sinh \xi \cot^{-1} \sinh \xi}{e\sqrt{1-e^2} - \sin^{-1} e} \right] - \frac{u_\xi}{J^2}\frac{\partial J}{\partial \xi} \\
&= -\frac{Uc \cos \eta}{J^2} f_2(\xi) - \frac{u_\xi}{J^2}\frac{\partial J}{\partial \xi},
\end{aligned} \tag{8.2.24}$$

$$\begin{aligned}
\left(\frac{1}{J}\frac{\partial u_\xi}{\partial \xi} \right)_{\xi_0} &= -Uc \cos \eta \left[\frac{1}{J^2}\left[\sinh \xi - \frac{1 + 1/\cosh^2 \xi - \sinh \xi \cot^{-1} \sinh \xi}{e\sqrt{1-e^2} - \sin^{-1} e} \right] \right]_{\xi_0} \\
&\equiv -\frac{Uc \cos \eta}{J_0^2} f_2(\xi_0),
\end{aligned} \tag{8.2.25}$$

with

$$\left. \begin{aligned}
J^2 = c^2 \sinh^2 \xi + c^2 \cos^2 \eta, \quad & J_0 = (J)_{\xi_0}, \\
f_1(\xi_0) = \sinh \xi_0 - \frac{1 - \sinh \xi_0 \cot^{-1} \sinh \xi_0}{e\sqrt{1-e^2} - \sin^{-1} e} &= \frac{-e^2}{e\sqrt{1-e^2} - \sin^{-1}(e)} = f_1(e), \\
f_2(\xi_0) = \sinh \xi_0 - \frac{1 + 1/\cosh^2 \xi_0 - \sinh \xi_0 \cot^{-1} \sinh \xi_0}{e\sqrt{1-e^2} - \sin^{-1} e} &= f_2(e) = 2f_1(e).
\end{aligned} \right\} \tag{8.2.26}$$

Boundary conditions at the surface of the ellipsoid (where $\xi = \xi_0$) are the kinematic condition and the normal stress balance

$$\left. \begin{aligned}
u_\xi = 0, \\
-C_G + \frac{\rho}{2}U^2 - \frac{\rho}{2}u_\eta^2 + \rho g h - 2\mu \left(\frac{1}{J}\frac{\partial u_\xi}{\partial \xi} - u_\eta \frac{c^2}{J^3}\cos \eta \sin \eta \right) = -\sigma \boldsymbol{\nabla} \cdot \boldsymbol{n},
\end{aligned} \right\} \tag{8.2.27}$$

where the distance from the top of the ellipsoid bubble and $\boldsymbol{\nabla} \cdot \boldsymbol{n}$ are given, respectively, by

$$h = b(1 - \cos \eta) = c \sinh \xi_0 (1 - \cos \eta), \quad \boldsymbol{\nabla} \cdot \boldsymbol{n} = \frac{\tanh \xi_0}{J_0^3} \left(J_0^2 + c^2 \cosh^2 \xi_0 \right). \tag{8.2.28}$$

44

For small η, we have

$$
\left.
\begin{aligned}
J_0 &= c \cosh \xi_0 \left(1 - \frac{\eta^2}{2 \cosh^2 \xi_0} + O(\eta^4) \right), \\
h &= c \sinh \xi_0 \left[\frac{1}{2} \eta^2 + O(\eta^4) \right], \\
(u_\eta)_{\xi_0} &= \frac{U f_1(\xi_0)}{\cosh \xi_0} \left[\eta + O(\eta^3) \right], \\
\left(\frac{1}{J} \frac{\partial u_\xi}{\partial \xi} \right)_{\xi_0} &= -\frac{U f_2(\xi_0)}{c \cosh^2 \xi_0} \left[1 - \left(\frac{1}{2} - \frac{1}{\cosh^2 \xi_0} \right) \eta^2 + O(\eta^4) \right], \\
\boldsymbol{\nabla} \cdot \boldsymbol{n} &= \frac{2 \sinh \xi_0}{c \cosh^2 \xi_0} \left(1 + \frac{\eta^2}{\cosh^2 \xi_0} + O(\eta^4) \right).
\end{aligned}
\right\}
\tag{8.2.29}
$$

Substitution of these into the normal stress balance leads to a formula for the planetary bubble:

$$
- C_G + \frac{\rho}{2} U^2 - \frac{\rho}{2} (u_\eta)_{\xi_0}^2 + \rho g h - 2\mu \left(\frac{1}{J} \frac{\partial u_\xi}{\partial \xi} - u_\eta \frac{c^2}{J^3} \cos \eta \sin \eta \right)_{\xi_0}
$$
$$
= -\sigma \frac{2 \sinh \xi_0}{c \cosh^2 \xi_0} \left(1 + \frac{\eta^2}{\cosh^2 \xi_0} \right). \tag{8.2.30}
$$

Thus we have C_G in $O(1)$

$$
C_G = \frac{\rho}{2} U^2 + \frac{2\mu U f_2(\xi_0)}{c \cosh^2 \xi_0} + \sigma \frac{2 \sinh \xi_0}{c \cosh^2 \xi_0}, \tag{8.2.31}
$$

and the following relation in $O(\eta^2)$

$$
-\frac{\rho}{2} \frac{U^2 f_1^2(\xi_0)}{\cosh^2 \xi_0} + \frac{\rho g c}{2} \sinh \xi_0 - \frac{2\mu U}{c \cosh^2 \xi_0} \left[f_2(\xi_0) \left(\frac{1}{2} - \frac{1}{\cosh^2 \xi_0} \right) - \frac{f_1(\xi_0)}{\cosh^2 \xi_0} \right]
$$
$$
= -\sigma \frac{2 \sinh \xi_0}{c \cosh^4 \xi_0}. \tag{8.2.32}
$$

8.2.3 Dimensionless rise velocity

By taking the major axis $D = 2a$ as a representative length scale, $\sqrt{gD}$ as a velocity scale, $D/\sqrt{gD}$ as a time scale, the parameters involved in the expanded solution of dimensionless form are

Froude number: $F_r = \dfrac{U}{\sqrt{gD}}$,   Gravity Reynolds number: $R_G = \dfrac{\sqrt{gD^3}}{\nu}$,

Eötvös number: $E_o = \dfrac{\rho g D^2}{\sigma}$,   aspect ratio: $e = \dfrac{c}{a} = \dfrac{1}{\cosh \xi_0}$.

In terms of these, the formula for the rise velocity of the ovary ellipsoid (which is now denoted by F_r) is given by (8.2.33) and that of the planetary ellipsoid is given by (8.2.34):

$$
- F_r^2 e^2 f_1^2(e) + \frac{1}{2} \left(1 - e^2 \right) - \frac{8 F_r}{R_G} e \left[f_2(e) \left(\frac{1}{2} + \frac{e^2}{1 - e^2} \right) + \frac{e^2 f_1(e)}{1 - e^2} \right]
$$
$$
= \frac{8}{E_o} \frac{e^2}{1 - e^2}, \tag{8.2.33}
$$

$$
- F_r^2 e^2 f_1^2(e) + \frac{1}{2} \sqrt{1 - e^2} - \frac{8 F_r}{R_G} e \left[f_2(e) \left(\frac{1}{2} - e^2 \right) - e^2 f_1(e) \right]
$$
$$
= -\frac{8}{E_o} e^2 \sqrt{1 - e^2}. \tag{8.2.34}
$$

In these equations, the first term in the left hand side denotes the kinetic energy due to the inertia (the pressure), the second is the gravity potential, the third is the normal viscous stress and the right hand side denotes the surface tension. The quadratic equations in F_r, (8.2.33) and (8.2.34), lead to the formula of the spherical bubble in the limit of $e \to 0$ ($\xi_0 \to \infty$ with a fixed).

The aspect ratio (or shape parameter) e is to be selected for a best fit to the experiment of Viana *et al.* There is no way that the formula (8.2.34) for the planetary ellipsoid can be made to fit the data; for example,

the dependence on an increase of E_o is such as to reduce the rise velocity whereas an increase, compatible with (8.2.33), is observed. We shall now confine our attention to the formula (8.2.33).

The formula (8.2.33) goes to the following equation in the limit $R_G \to \infty$:

$$F_{r\infty} = \frac{1}{ef_1(e)} \sqrt{\frac{1}{2}(1-e^2) - \frac{8}{E_o}\frac{e^2}{1-e^2}}. \tag{8.2.35}$$

For small R_G, the formula (8.2.33) may be approximated by a linear equation in F_r/R_G to give the solution:

$$F_r = \frac{(1-e^2)^2 - 16e^2/E_o}{f_2(e)(1+e^2) + 2e^2 f_1(e)} \frac{R_G}{8e}, \tag{8.2.36}$$

whence $F_r \to 0$ as $R_G \to 0$.

When $F_r = 0$, (8.2.33) is reduced to the equation:

$$E_o = 16\frac{e^2}{(1-e^2)^2}. \tag{8.2.37}$$

If we put $E_o = 4$ as noted in section 8.1.4, we have $e = 0.41$, thus $0.41 \le e < 1$ for $4 \le E_o$, which means that the bubble may be an ovary ellipsoid. It is noted here that (8.2.37) gives $F_{r\infty} = 0$ in (8.2.35) and $F_r = 0$ in (8.2.36), which leads to the condition that $E_o \ge 16e^2/(1-e^2)^2$ for a positive or zero solution F_r to the quadratic equation (8.2.33).

In the limit $e \to 0$ equation (8.2.33) describes the rise velocity of a perturbed spherical cap bubble. To obtain this perturbation formula we note that

$$\left. \begin{array}{c} \dfrac{c}{a} = \dfrac{1}{\cosh \xi_0} = e, \quad \dfrac{b}{c} = \sinh \xi_0 = \dfrac{\sqrt{1-e^2}}{e} \\[2mm] ef_1(e) = \dfrac{1}{2}ef_2(e) \sim \dfrac{3}{2}\left(1 - \dfrac{1}{5}e^2 - \dfrac{8}{175}e^4 + \cdots\right). \end{array} \right\} \tag{8.2.38}$$

After inserting these expressions into (8.2.33) retaining terms proportional to e^2, we find that

$$\frac{9}{4}F_r^2 + \frac{12F_r}{R_G} - \frac{1}{2} = e^2\left\{\frac{8}{E_o} + \frac{1}{2} - \frac{9}{10}F_r^2 + \frac{168}{5}\frac{F_r}{R_G}\right\}. \tag{8.2.39}$$

The leading order terms on the left were obtained by Joseph but the perturbation terms on the right are different. The curvature s in equation (8.1.4) is related to the aspect ratio by

$$s = -e^2/2(1-e^2), \tag{8.2.40}$$

whence, to leading order, we find that $e^2 = -2s$.

8.3 Comparison of theory and experiment

Viana *et al.* (2003) made experiments of Taylor bubbles as shown in figure 8.6. Their data may be expressed as a functional relationship between three parameters F_r, E_o and R_G as in equations (8.1.1, 8.1.2, 8.1.3).

In figure 8.7, we have plotted data F_r versus R_G for 12 values of E_o. It is important to note what was done with this data by Viana *et al.* (2003) and what we do with it here. Viana *et al.* (2003) identified a slope region for small $R_G < 10$, a flat region for $R_G > 200$ and a transition between. The flat region and the slope region give rise to power laws which were merged into the transition region using a logistic dose curve. This type of fitting was discussed briefly in §8.1 and extensively by Viana *et al.* (2003).

Here, in figure 8.7, we plot F_r versus R_G data for 12 values of E_o but we fit this data with the analytic expression (8.2.33) for an ovary ellipsoid rather than to power laws. The aspect ratio $e(E_o)$ is a fitting parameter and is listed in table 8.1, in which $e_o = e(E_o)$ is the value of e in (8.2.33) selected as the value which most closely fit the data of Viana *et al.* (2003) for the 12 cases in figure 8.7. This software also gives the value $F_{r\infty}$ in (8.2.35) and it leads to the correlation

$$e_o = E_o^{0.0866}/0.357 \tag{8.3.1}$$

where the deviation in given by $\delta e = e - e_o$. The success of this procedure is impressive.

The processing of data for table 8.1 is represented graphically in figure 8.8.

Table 8.1 shows that e_o is a very weak function of $E_o \geq 15$ with data tending to a value $e_o = 0.6$ corresponding to an ellipsoid with

$$b \cong 0.8a \qquad (8.3.2)$$

which like the true Taylor bubble has an almost spherical cap (see figure 8.9).
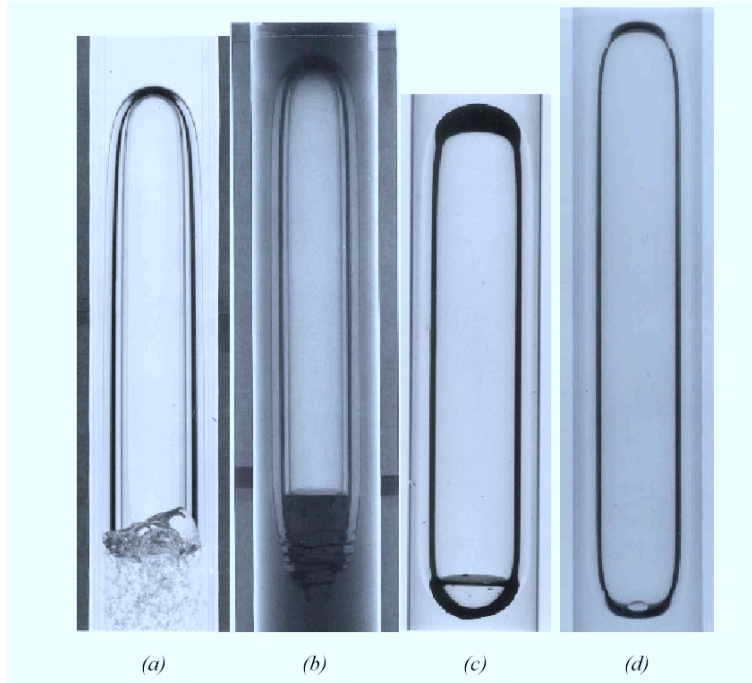
Fig. 8.6. Photographs of Taylor bubbles rising through 76.2 mm inside diameter pipe filled with different viscosity liquids. This figure is quoted from Viana *et al.* (2003).

Table 8.1. *Selection of $e(E_o)$ for 12 cases of E_o. The deviation is given by $\delta e = e - e_o$ with (8.3.1) and $F_{r\infty}$ is computed by (8.2.35).*

E_o	e	δe	$F_{r\infty}$	$\log F_{r\infty}$	Figure 8.7
6	0.471243	−0.042313	0.06391207	−1.194417	(a)
10	0.536543	−0.000228	0.128435	−0.891313	(b)
11	0.538667	−0.002551	0.170713	−0.767732	(c)
13	0.547626	−0.001474	0.209595	−0.678617	(d)
15	0.555870	−0.000073	0.233737	−0.631272	(a)
17	0.563567	0.001559	0.250282	−0.601570	(b)
17.5	0.567265	0.003855	0.250587	−0.601040	(c)
19	0.568630	0.003855	0.265555	−0.575845	(d)
22	0.571912	−0.002768	0.286857	−0.542334	(a)
25	0.580741	−0.000333	0.295449	−0.529518	(b)
27	0.583492	−0.001466	0.302880	−0.518728	(c)
35	0.593930	−0.004315	0.322398	−0.491607	(d)

8.4 Comparison of theory and correlations

The processing of data on the rise velocity of Taylor bubbles in tubes of stagnant liquids by Viana *et al.* (2003) leads to the correlation formula (8.1.3) with small errors described by figure 8.1. We may then propose that the rise velocity is accurately described by (8.1.3); however the shape of the bubble nose is not predicted.

The theory of the rise of ovary ellipsoidal gas bubbles in viscous liquids leads to a rigorous prediction of the aspect ratio of the ovary ellipsoid which rises with exactly the same velocity F_r at given values of E_o and R_G as the Taylor bubble. The value of e is determined by simultaneous for e of (8.2.33) and (8.1.3) for given values of F_r, R_G and E_o (figure 8.10).

A slightly simpler solution can be written out for $R_G > 200$ in which case (8.1.3) is replaced with the simpler formula:

$$F_r = 0.34/\left(1 + 3805/E_o^{3.06}\right)^{0.58},$$ (8.4.1)

48

(a)

(b)
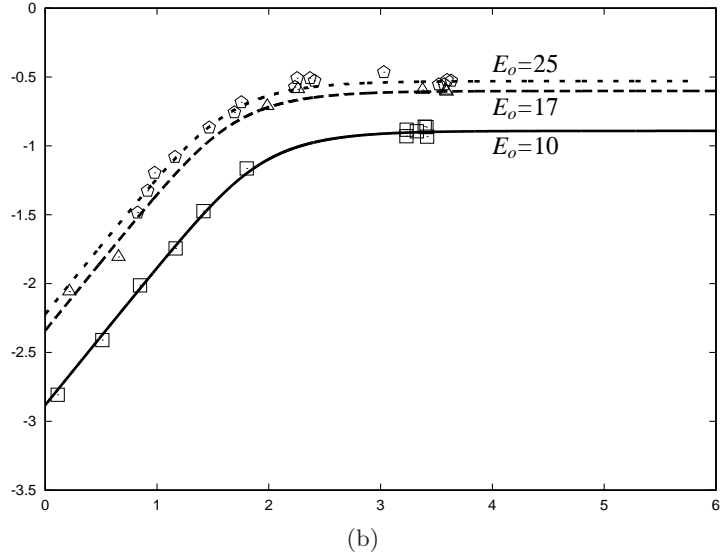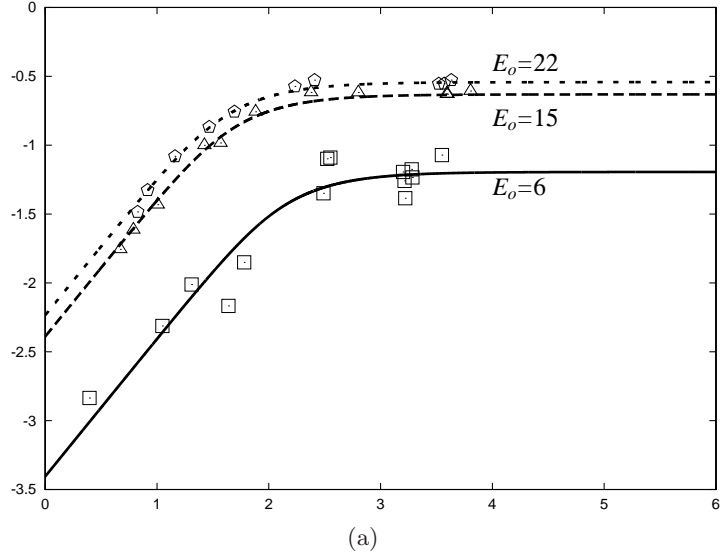
which is to be solved simultaneously with (8.2.33) in the limit $R_G \to \infty$:

$$\frac{-F_r^2 e^6}{\left[e + (1 - e^2) \tanh^{-1}(e)\right]^2} + \frac{1}{2}\left(1 - e^2\right) = \frac{8}{E_o}\frac{e^2}{1 - e^2}, \tag{8.4.2}$$

for $e(E_o, R_G)$ for given values of E_o (figure 8.10).

8.5 Conclusion

A formula is derived giving the rise velocity of an ellipsoidal gas bubble in a viscous liquid assuming that the motion of the liquid is irrotational. The rise velocity is expressed by a Froude number and it is determined by a Reynolds number, an Eötvös number and the aspect ratio of the ellipsoid. The formula for the ovary ellipsoid was fit to the data of Viana *et al.* (2003) who correlated all the published data on the rise velocity of long gas bubbles in round tubes filled with viscous liquids. This data is accurately represented by our formula when the aspect ratio takes on certain values. The fitting generates a family of aspect ratios which depends strongly on the Eötvös number and less strongly on the Reynolds number; this shows that the change in the shape of the nose of the rising bubble is strongly influenced by surface tension. Our analysis completely neglects sidewall drainage induced by the rising bubble and cannot be a precise description of the dynamics. We have generated what might be called the ovary ellipsoid model of a Taylor bubble. This model is very simple and astonishingly accurate.
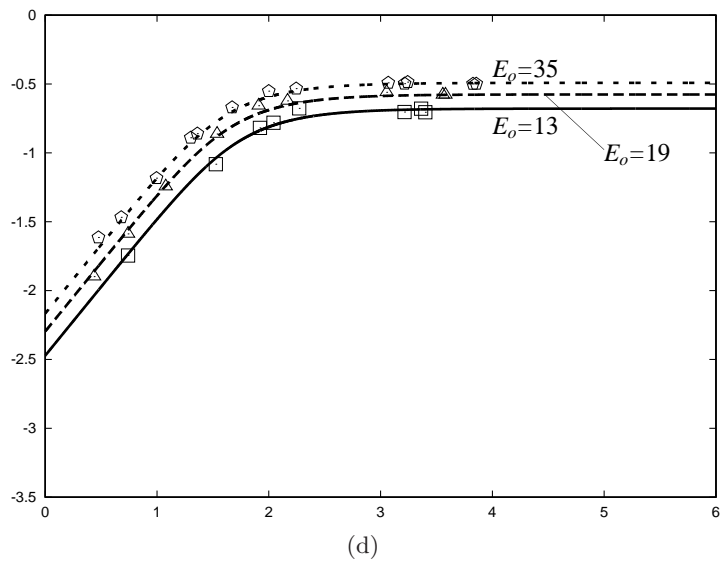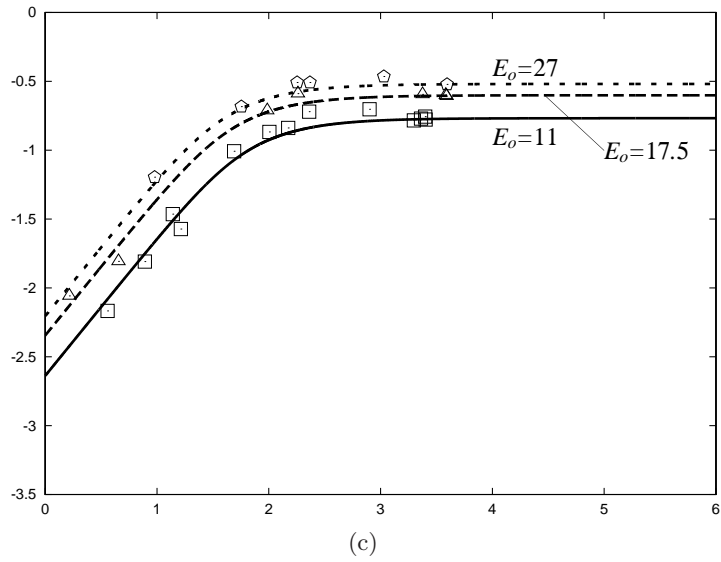
Fig. 8.7. $\log F_r$ versus $\log R_G$ for 12 values of E_o. The lines - - -, $- - -$, ——— are plots of (8.2.33) with $e(E_o)$ selected for best fit as described in table 8.1.
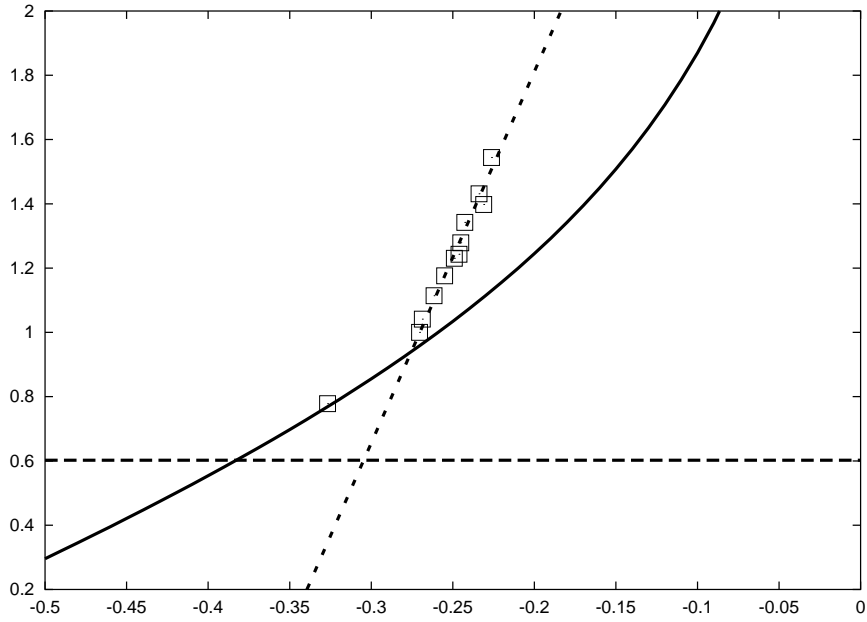
Fig. 8.8. $\log E_o$ versus $\log e$; $\square$ denotes the data given in table 8.1. The solid curve denotes the border $F_r = 0$ given by (8.2.37), above which one positive solution of F_r may exist and below which there arise two negative sollutions or complex solutions which are meaningless. The dashed line is for $E_o = 4$. The dotted line denotes $\log e = 0.0865513 \log E_o - 0.356762$ for which $e_o = E_o^{0.0866}/0.357$.
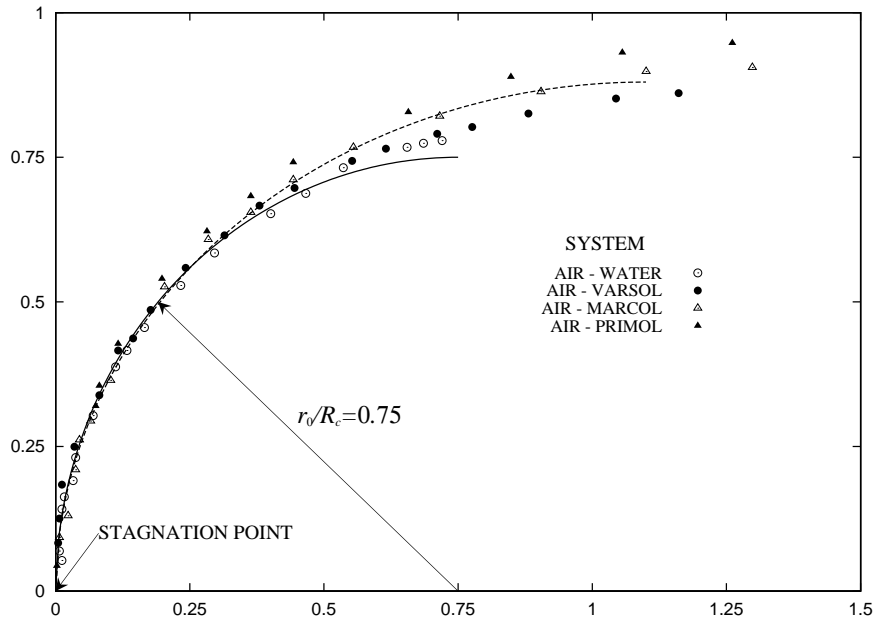
Fig. 8.9. Comparison of Brown's 1965 measurements of the shape of a large Taylor bubble rising in a round tube with an ovary ellipsoid (denoted by the dashed line) with $e = c/a = 0.6$, $b = a\sqrt{1 - e^2} = 0.8a$, $a = 1.10$. Ovary ellipsoids with smaller e are more spherical.

51
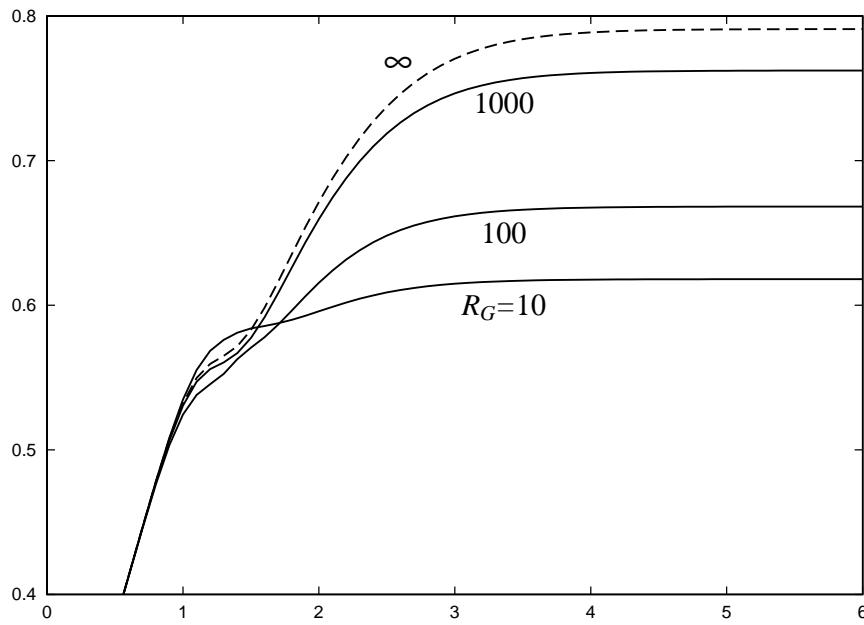
Fig. 8.10. $e(E_o, R_G)$ versus $\log E_o$ for various values of R_G. The curves ——— are obtained by the simultaneous equations (8.1.3) and (8.2.33). The solution of (8.4.1) and (8.4.2) is shown as - - - - -; all the solutions (8.1.3) and (8.2.33) coincide with - - - - - when $R_G > 10^4$.

9
Rayleigh-Taylor instability of viscous fluids

Rayleigh-Taylor (hereafter RT) instabilities are very important and very pervasive. They are driven by acceleration when a liquid acceleration away from a gas or vacuum. The signature of this instability is the waves which corrugate the free surface at the instant of acceleration. Ultimately these waves will finger into the liquid causing it to break-up.

Rayleigh (1890) showed that a heavy fluid over a light fluid is unstable, as common experience dictates. He treated the stability of heavy fluid over light fluid without viscosity, and he found that a disturbance of the flat free surface grows exponentially like $\exp(nt)$ where

$$n = \left\{ \frac{kg(\rho_2 - \rho_1)}{\rho_1 + \rho_2} \right\}^{1/2}, \tag{9.0.1}$$

where ρ_2 is the density of the heavy fluid, ρ_1 is the density of the light fluid, g is the acceleration due to gravity and $k = 2\pi/\ell$ is the wavenumber and ℓ is the wavelength. The instability described by (9.0.1) is catastrophic since the growth rate n tends to infinity, at any fixed time, no matter how small, as the wavelength tends to zero. The solutions are unstable to short waves even at the earliest times. Such disastrous instabilities are called 'Hadamard unstable' and the initial value problems associated with these instabilities are said to be 'ill posed' (Joseph & Saut 1990). Ill-posed problems are disasters for numerical simulations: because they are unstable to ever shorter waves, the finer the mesh, the worse the result.

Nature will not allow such a singular instability; for example, neglected effects like viscosity and surface tension will enter the physics strongly at the shortest wavelength. These effects have been taken into account in the study of RT instability by Harrison (1908) and in treatise of Chandrasekhar (1961). Surface tension eliminates the instability of the short waves; there is a finite wavelength depending strongly on viscosity as well as surface tension for which the growth rate n is maximum. This is the wavelength that should occur in a real physical problem and would determine the wavelength on the corrugated fronts of breaking drops in a high-speed air flow.

Taylor (1950) extended Rayleigh's inviscid analysis to the case where a constant acceleration of the superposed fluids other than gravity is taken into account. Assuming a constant value for the acceleration, Taylor (1950) showed that when two superposed fluids of different densities are accelerated in a direction perpendicular to their interface, this surface is unstable if the acceleration is directed from the lighter to the heavier fluid. The Taylor instability depends strongly on the value of the acceleration a; for example, if g in (9.0.1) is replaced by $a = 10^4 g$, the growth rate n is increased by a factor of 100.

9.1 Acceleration

The acceleration of the drop is a major factor in the Rayleigh-Taylor (RT) instability. It is instructive to see how the acceleration enters into the equations of motion. Suppose the laboratory frame is identified with $(\boldsymbol{X}, \hat{t})$ and the drop velocity is $\boldsymbol{v}(\boldsymbol{X}, \hat{t})$. Then we refer the equations of motion

$$\rho \left(\frac{\partial \boldsymbol{v}}{\partial \hat{t}} + \boldsymbol{v} \cdot \frac{\partial \boldsymbol{v}}{\partial \boldsymbol{X}} \right) = \operatorname{div} \mathbf{T} + \rho \boldsymbol{g}, \quad \frac{\partial}{\partial \boldsymbol{X}} \cdot \boldsymbol{v} = 0 \tag{9.1.1}$$
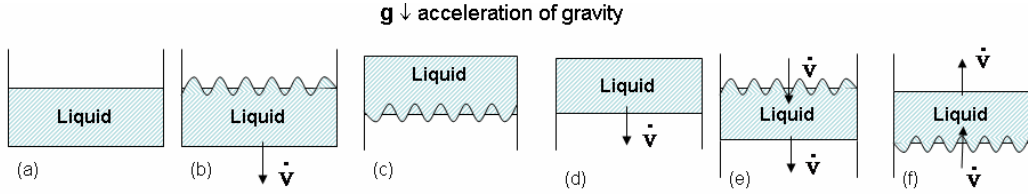
Fig. 9.1. RT instability: (a) the liquid in the containers at rest is stable under gravity (Rayleigh 1890) but if the container is turned upside down as in (c) the liquid falls out. The liquid at rest in container can be destabilized by downward acceleration of the liquid $a > g$ away from gas as in (b) and in the upside down case the liquid can be prevented from falling out by accelerating downward with $\dot{V} > g$ as in (d). If we open up the container and accelerates the liquid downward with $\dot{V} > g$, the top surface which accelerates away from the gas is unstable but the bottom surface which accelerates into the gas is stabilized as in (e), with the opposite effect when the acceleration is reversed as in (f).

to an accelerating frame in which the mass center of the drop is stationary, identified with $(\boldsymbol{x}, t)$ and $\boldsymbol{v}(\boldsymbol{X}, \hat{t}) = \boldsymbol{U}(\boldsymbol{x}, t) + \boldsymbol{V}(t)$, $\mathrm{d}\boldsymbol{X} = \mathrm{d}\boldsymbol{x} + \boldsymbol{V}(t)\mathrm{d}t$, $\mathrm{d}\hat{t} = \mathrm{d}t$. Then we find that

$$\rho\left(\frac{\partial \boldsymbol{U}}{\partial t} + \boldsymbol{U} \cdot \frac{\partial \boldsymbol{U}}{\partial \boldsymbol{x}}\right) + \rho\dot{\boldsymbol{V}} = \operatorname{div}\mathbf{T} + \rho\boldsymbol{g}, \quad \frac{\partial}{\partial \boldsymbol{x}} \cdot \boldsymbol{U} = 0 \qquad (9.1.2)$$

where $\mathbf{T}$ is the stress tensor.

The term

$$\rho\left(\boldsymbol{g} - \dot{\boldsymbol{V}}\right) \qquad (9.1.3)$$

enters into Rayleigh-Taylor instability and $\dot{\boldsymbol{V}}$ dominates in the drop breakup problem because the initial velocity is very small and the initial acceleration is very large.

The Rayleigh-Taylor instability occurs when $\dot{\boldsymbol{V}}$ is directed from the light to the heavy fluid as when the initially stationary drop is accelerated to the free-stream velocity in the high-speed air stream behind the shock in the shock tube or when a moving drop in a stagnant fluid is decelerated by the air to zero velocity. The analysis works well in air and liquid where the density and viscosity of air can be neglected with only small error; there is Rayleigh-Taylor instability in a vacuum because it is the drop acceleration term and not the material properties of air which induces the instability.

In the present application the acceleration of the drop is roughly proportional to the dynamic pressure which vanishes in a vacuum. Drop breakup in a vacuum could occur by acceleration due to gravity, say in a rarified Jovian atmosphere.

9.2 Simple thought experiments

These experiments are embodied in the cartoons and caption of figure 9.1. These experiments show the difference between the theory of Rayleigh (1890) who considered gravity g and Taylor (1950) who considered the effect of the acceleration $\dot{V}$. The accelerations destabilize the liquid-gas surfaces which accelerate away from the gas and stabilize the liquid-gas surface which accelerate toward the gas (figure 9.1 (e)).

9.3 Analysis

The linear theory of stability superposes small disturbances on a basic flow solution of the equations of motion. Nonlinear terms in small perturbation quantities are neglected. The properties of the basic flow are important. The basic flow for RT instability deserves consideration. Here we look for conditions under which corrugations appear on flat free surface on a liquid moving into or away from a gas or vacuum. What is important here is the acceleration and the fact that shear stresses do not develop in the basic flow. This is, of course, is even clearer if you take the gas away and leave a vacuum. In this chapter and in chapter 21 on RT instability of viscoelastic drops, we are obliged to consider RT instability on the front face of a flattened drops in which Kelvin-Helmholtz (KH) instability driven by shearing motion may play a minor role.

Lewis (1950) has shown experimentally that a layer of water driven by compressed air is unstable and that small disturbances, introduced at the air-water interface, grow so that it appears as though fingers of air move

through the water layer. Lewis (1950) finds agreement with his experiments when the viscosity of the liquid is small. The peaks of water in his experiments are sharp, but the match between Taylor's theory and the Lewis experiment is not perfect because the regularizing effects of surface tension were neglected.

The breakup of water drops in a high speed air behind a shock wave in a shock tube was studied in excellent experiments by Engel (1958). Since the acceleration is perpendicular to the air-liquid interface and directed from gas to liquid, the accelerating liquid drop is unstable and is prey to the characteristic short wave corrugation associated with this instability.

Joseph, Belanger and Beavers (1999) (hereafter JBB) studied the breakup of liquid drops of high and low viscosity and viscoelastic drop in high air behind shock waves moving at Mach numbers $M_s = 2$ and $M_s = 3$. They measured acceleration and wave lengths on the corrugation drops.

The corrugations at the front of an unstable drop are driven toward the drop equator by shear flow of gas coming from the high pressure stagnation point. This shear flow may also be subject to an instability of the Kelvin-Helmholtz type. Since the tangential velocity is zero at the stagnation point and small near the stagnation point, the Kelvin-Helmholtz instability may not interact too strongly with the Rayleigh-Taylor instability.

Some details of the corrugations on the front of breaking drops can be predicted by mathematical analysis of the foregoing instabilities, but the effects of viscosity and surface tension must be taken into account.

9.3.1 Linear theory of Chandrasekhar

A thorough explanation and analysis of the Rayleigh-Taylor instability can be found in Chapter X of the treatise by Chandrasekhar. Some effects of viscosity in special problems in Rayleigh-Taylor instability have been considered by Plesset and Whipple (1973). In Chandrasekhar's analysis the two fluids are separated by an interface $z = h(x, y, t)$ which perturbs the plane $z = 0$. The Navier-Stokes equations for the perturbations velocity $\boldsymbol{u}$, perturbation pressure p are solved above and below the plane $z = 0$. Gravity points down against the direction of z increasing. It is assumed that the heavy fluid is above the light fluid, or that the light fluid is accelerated into the heavy fluid above (the drop is the heavy fluid and the gas flowing into and around it is the light fluid). At the flat interface at $z = 0$, the linearized kinematic equation is

$$w = \frac{\partial h}{\partial t} \tag{9.3.1}$$

where

$$[|w|] = w_2 - w_1 \tag{9.3.2}$$

is the jump in the normal (z component) of velocity (w_2 is in $z > 0$, w_1 in $z < 0$). For the viscous case the jump in the tangential velocity is also zero

$$[|w|] = [|u|] = [|v|] = 0 \tag{9.3.3}$$

where u is in the x direction and v in the y direction. Since (9.3.3) holds for all x and y for $z = 0$, we may deduce that

$$\left[\left|\frac{\partial u}{\partial x} + \frac{\partial v}{\partial y}\right|\right] = -\left[\left|\frac{\partial w}{\partial z}\right|\right] = 0 \tag{9.3.4}$$

The continuity of the shear stress is expressed by

$$\left[\left|\mu\left(\frac{\partial u}{\partial z} + \frac{\partial w}{\partial x}\right)\right|\right] = 0, \quad \left[\left|\mu\left(\frac{\partial v}{\partial z} + \frac{\partial w}{\partial y}\right)\right|\right] = 0 \tag{9.3.5}$$

where μ is the viscosity.

The balance of normal stress is given by

$$-[|p|] + 2\left[\left|\mu\frac{\partial w}{\partial z}\right|\right] = -\gamma\left(\frac{\partial^2}{\partial x^2} + \frac{\partial^2}{\partial y^2}\right)h \tag{9.3.6}$$

where γ is the surface tension. We may remove the hydrostatic pressure from the z equation of motion by introducing the dynamic pressure

$$\pi = p + \rho g h$$

55

hence,

$$[|\pi|] = gh\,[|\rho|] + 2\left[\left|\mu\frac{\partial w}{\partial z}\right|\right] + \gamma\left(\frac{\partial^2}{\partial x^2} + \frac{\partial^2}{\partial y^2}\right)h \tag{9.3.7}$$

After introducing normal modes proportional to

$$f(z)\mathrm{e}^{nt+\imath k_x x+\imath k_y y}, \quad k^2 = k_x^2 + k_y^2 \tag{9.3.8}$$

where $f(z)$ is an amplitude function for π, u, v and h which may be eliminated to find equation (40) on page 433 of Chandrasekhar:

$$\left[\left|\left\{\left[\rho - \frac{\mu}{n}\left(\frac{\mathrm{d}^2}{\mathrm{d}z^2} - k^2\right)\right]\frac{\mathrm{d}w}{\mathrm{d}z} - \frac{1}{n}\left\{\left(\frac{\mathrm{d}^2}{\mathrm{d}z^2} + k^2\right)w\right\}\frac{\mathrm{d}\mu}{\mathrm{d}z}\right\}\right|\right] = -\frac{k^2}{n^2}\left\{g\,[|\rho|] - k^2\gamma\right\}w - \frac{2k^2}{n}\left[\left|\mu\frac{\mathrm{d}w}{\mathrm{d}z}\right|\right]. \tag{9.3.9}$$

For the present problem for which the unperturbed states above and below $z = 0$ are uniform $\mathrm{d}\mu/\mathrm{d}z = 0$ and, using (9.3.4)

$$\left[\left|\mu\frac{\mathrm{d}w}{\mathrm{d}z}\right|\right] = [|\mu|]\frac{\mathrm{d}w}{\mathrm{d}z}. \tag{9.3.10}$$

The entire problem is resolved by

$$w_1 = A_1\mathrm{e}^{kz} + B_1\mathrm{e}^{q_1 z} \ (z < 0)$$
$$w_2 = A_2\mathrm{e}^{-kz} + B_2\mathrm{e}^{-q_2 z} \ (z > 0) \tag{9.3.11}$$

where

$$q_1 = \sqrt{k^2 + n/\nu_1} \quad \text{and} \quad q_2 = \sqrt{k^2 + n/\nu_2}$$
$$\nu_1 = \mu_1/\rho_1, \quad \nu_2 = \mu_2/\rho_2 \tag{9.3.12}$$

provided that Chandrasekhar's equation (113) below is satisfied

$$-\left\{\frac{gk}{n^2}\left[(\alpha_1 - \alpha_2) + \frac{k^2\gamma}{g\,(\rho_1 + \rho_2)}\right] + 1\right\}(\alpha_2 q_1 + \alpha_1 q_2 - k) - 4k\alpha_1\alpha_2 + \frac{4k^2}{n}(\alpha_1\nu_1 - \alpha_2\nu_2)$$
$$\times \left\{(\alpha_2 q_1 - \alpha_1 q_2) + k\,(\alpha_1 - \alpha_2)\right\} + \frac{4k^3}{n^2}(\alpha_1\nu_1 - \alpha_2\nu_2)^2\,(q_1 - k)(q_2 - k) = 0 \tag{9.3.13}$$

where

$$\alpha_1 = \frac{\rho_1}{\rho_1 + \rho_2}, \quad \alpha_2 = \frac{\rho_2}{\rho_1 + \rho_2}, \quad \alpha_1 + \alpha_2 = 1$$

When the light fluid is gas; with only a very small error we may treat this as a vacuum. Hence we put

$$\rho_1 = \alpha_1 = 0, \quad \alpha_2 = 1$$
$$q_1 \to k, \quad \alpha_2 q_1 + \alpha_1 q_2 - k \to q_1 - k$$
$$(\alpha_2 q_1 - \alpha_1 q_2) + k\,(\alpha_1 - \alpha_2) \to q_1 - k \tag{9.3.14}$$

and, after factoring $q_1 - k$ in (9.3.13) we get

$$1 - \frac{gk}{n^2} = -\frac{k^3\gamma}{n^2\rho_2} - \frac{4k^2}{n}\frac{\mu_2}{\rho_2} + \frac{4k^3}{n^2}\frac{\mu_2^2}{\rho_2^2}(q_2 - k). \tag{9.3.15}$$

9.3.2 Viscous potential flow

The Rayleigh-Taylor instability may also be analyzed as a viscous potential flow (Joseph, 1994). In this approach the perturbation velocity is given by a potential

$$\boldsymbol{u} = \nabla\phi \tag{9.3.16}$$

and the Navier-Stokes equations are reduced to an identity provided that the pressure is given by Bernoulli's equation

$$p + \rho\frac{\partial\phi}{\partial t} + \rho gz = -\frac{\rho}{2}\,|\nabla\phi|^2. \tag{9.3.17}$$

In this linearization used to study instability the term on the right side of (9.3.17) is put to zero. The interface condition requires continuity of tangential velocities, (9.3.3) and (9.3.4), and the continuity of shear stress (9.3.5) cannot be enforced in viscous potential flow. The pressure in the normal stress condition (9.3.6) is eliminated using (9.3.17); this gives rise to

$$\left[\left|\rho \frac{\partial \phi}{\partial t}\right|\right] + gh[|\rho|] + 2\left[\left|\mu \frac{\partial w}{\partial z}\right|\right] + \gamma \left\{\frac{\partial^2}{\partial x^2} + \frac{\partial^2}{\partial y^2}\right\} h = 0. \tag{9.3.18}$$

After introducing normal modes, writing (9.3.1) as $nh = w$, we get

$$n[|\rho\phi|] + \frac{w}{n}[|\rho|]g + 2\left[\left|\mu \frac{\partial w}{\partial z}\right|\right] - \frac{\gamma k^2}{n}w = 0 \tag{9.3.19}$$

For viscous potential flow, $\nabla^2 \phi = 0$ everywhere and (9.3.11) holds with $B_1 = B_2 = 0$ and

$$\frac{\mathrm{d}w}{\mathrm{d}z} = \frac{\mathrm{d}^2\phi}{\mathrm{d}z^2} = k^2\phi. \tag{9.3.20}$$

After writing $[|\rho\phi|] = (1/k^2)[|\rho \mathrm{d}w/\mathrm{d}z|]$ in (9.3.19) we may verify that (9.3.9) and (9.3.19) are identical when (9.3.9) is evaluated for viscous potential flow. Further evaluation of (9.3.19) with normal modes give rise to the dispersion relation

$$1 = \frac{k}{n^2}\frac{\rho_2 - \rho_1}{\rho_2 + \rho_1}g - \frac{k^3\gamma}{n^2(\rho_2 + \rho_1)} - \frac{2k^2}{n}\frac{\mu_2 + \mu_1}{\rho_2 + \rho_1}. \tag{9.3.21}$$

Equation (9.3.21) may be solved for the growth rate

$$n = -k^2\frac{\mu_2 + \mu_1}{\rho_2 + \rho_1} \pm \left[k\frac{\rho_2 - \rho_1}{\rho_2 + \rho_1}g - \frac{k^3\gamma}{\rho_2 + \rho_1} + k^4\left(\frac{\mu_2 + \mu_1}{\rho_2 + \rho_1}\right)^2\right]^{1/2} \tag{9.3.22}$$

If the quantity under the root is negative, then the real part is negative and the interface is stable. For instability it is sufficient that

$$\sqrt{k\frac{\rho_2 - \rho_1}{\rho_2 + \rho_1}g + k^4\left(\frac{\mu_2 + \mu_1}{\rho_2 + \rho_1}\right)^2 - \frac{k^3\gamma}{\rho_2 + \rho_1}} > k^2\frac{\mu_2 + \mu_1}{\rho_2 + \rho_1}. \tag{9.3.23}$$

The border of instability $n = 0$ for $k = k_c$ is given by

$$k_c = \sqrt{\frac{(\rho_2 - \rho_1)g}{\gamma}} \tag{9.3.24}$$

independent of viscosity.

Evaluation of the growth rate formula with the gas neglected gives

$$n = -\frac{k^2\mu_2}{\rho_2} \pm \sqrt{kg - \frac{k^3\gamma}{\rho_2} + \frac{k^4\mu_2^2}{\rho_2^2}} \tag{9.3.25}$$

It is of interest to compare the growth rate formula (9.3.25) for viscous potential flow with the growth rate formula (9.3.15) for Chandrasekhar's exact solution. These two formulas give exactly the same growth rate when

$$q_2 - k = k\sqrt{1 + \frac{n\rho_2}{\mu_2 k^2}} - k \cong \frac{n\rho_2}{2\mu_2 k} \tag{9.3.26}$$

and

$$\frac{n\rho_2}{2\mu_2 k} \ll 1 \tag{9.3.27}$$

9.4 Comparison of theory and experiments

To evaluate the formulas for Rayleigh-Taylor instability for the experiments of JBB we must

$$\text{replace } g \text{ with } a = \dot{V}. \tag{9.4.1}$$

57
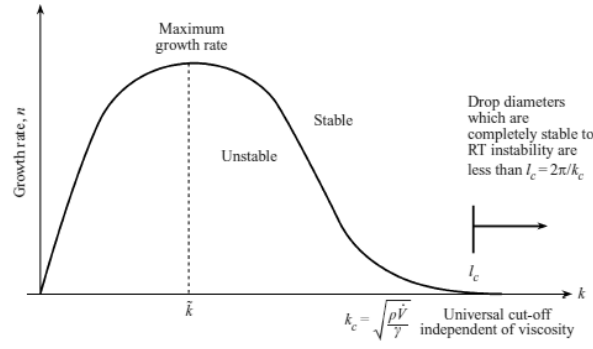
Fig. 9.2. Growth rate curve.

Equation (9.3.24) then implies that

$$k_c = \frac{2\pi}{\lambda_c} = \sqrt{\frac{\rho_2 a}{\gamma}} \qquad (9.4.2)$$

and waves with length

$$\lambda < \lambda_c = 2\pi\sqrt{\frac{\gamma}{\rho_2 a}} \qquad (9.4.3)$$

are stable. Taking liberties with (9.4.3), we identify $\lambda = D$ where D is the diameter of drops with acceleration a that cannot be fragmented by Rayleigh-Taylor instability. Applying this to our experiments (table 9.1) we get D between

$$23 \text{ and } 65\mu\text{m for } M_S = 3 \qquad (9.4.4)$$
$$46 \text{ and } 135\mu\text{m for } M_S = 2. \qquad (9.4.5)$$

A typical growth rate curve for the parameters in (9.4.4) and in (9.4.5) is shown by Fig.9.2.

9.5 Comparison of the stability theory with the experiments on drop breakup

JBB studied the breakup of liquid drops of high and low viscosity behind a shock wave in a shock tube moving with shock Mach number $M_s = 2$ and $M_s = 3$. The data for the experiments is listed in table 2 of JBB together with values of the dimensionless parameters. The Ohnesorge number Oh, the Weber number We and the Reynolds number Re

$$Oh = \frac{\mu_d}{(\rho_d D \gamma)^{1/2}}, \quad We = \frac{\rho V^2 D}{\gamma}, \quad Re = \frac{VD\rho}{\mu} \qquad (9.5.1)$$

are defined in terms of the initial drop diameter D, drop viscosity μ_d, surface tension γ, drop density ρ_d, and the free stream values of the velocity V, viscosity μ, and density ρ.

The breakup of drops in high speed airstream behind a shock wave in a shock tube was photographed with a rotating drum camera giving one photograph every $5\ \mu$s. From these photographs, JBB created movies of the fragmentation history of viscous drops of widely varying viscosity, and viscoelastic drops, at very high Weber and Reynolds numbers. Drops of the order of one millimeter are reduced to droplet clouds and possibly to vapor in times less than $500\ \mu$s. The movies may be viewed at http://www.aem.umn.edu/research/Aerodynamic_Breakup. They reveal sequences of breakup events which were previously unavailable for study. Bag and bag-and-stamen breakup can be seen at very high Weber numbers, in the regime of breakup previously called 'catastrophic.' The movies generate precise displacement-time graphs from which accurate values of acceleration (of orders 10^4 to 10^5 times the acceleration of gravity) are computed. These large accelerations from gas to liquid put the flattened drops at high risk to Rayleigh-Taylor instabilities. The most unstable Rayleigh-Taylor wave fits nearly perfectly with waves measured on enhanced images of drops from the movies, but the effects of viscosity cannot be neglected.

The breakup of drops in a high speed air stream exhibits universal features. First the shock wave passes over
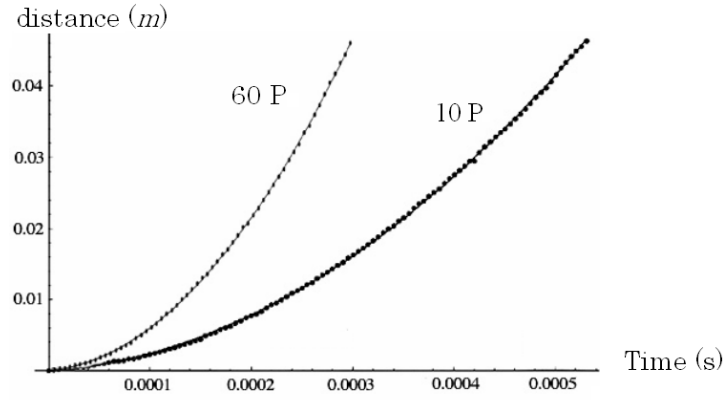
Liquid	Viscosity (Poise)	Initial accel. $M_s = 3.0$	(10^5m/sec^2) $M_s = 2.0$	Initial drop diameter (mm)
Silicone Oil	1	15.8	4.0	2.6
	10	11.12	2.92	2.6
	30	9.98	3.08	2.6
	40	12.06	2.02	2.5
	40	11.08	-	2.1
	50	8.99	-	2.5
	60	9.78	-	2.6
	100	7.73	-	2.6
2% Polyox	350	6.48	1.37	2.9
2% Polyacrylamide	9.6	4.92	-	3.2
2.6% PSBA / TBP	11.3	7.28	2.32	2.2
Glycerine	14.9	8.43	4.38	2.4
Water	0.01	6.47	1.52	2.5

Fig. 9.3. Time-displacement graph giving the acceleration of drops from the experiment of JBB 1999.

the drop. The shock wave does not have an important effect on the drop breakup. In the instant after the shock passes the speed of the air stream steps up a high value. The drop flattens because the stagnation pressure, fore and aft is very large before the boundary layer separates. At first, the flattened drop is stationary but it accelerates with huge accelerations larger than $10^4 g$, from gas to liquid. Corrugations due to RT instability are seen on the front, but not on the back face. These corrugations are driven away from the high pressure stagnation point on the front face to the equator where they are stripped away from the drop. The waves on the front face can be said to be driven by a Kelvin-Helmholtz instability. Since the tangential velocity is zero at the stagnation point, the Kelvin-Helmholtz may not interact too strongly with the RT instability.

A major achievement of the experimental study of JBB is the accurate measurement of acceleration using time-displacement data of the type shown in figure 9.3. More such time displacement graphs can be found in JBB and in the paper on breakup of viscoelastic drops by Joseph, Beavers and Funada (JBF) (2002).

Growth rate curves for the conditions specified in figure 9.3 are shown in figure 9.4 and 9.5. Values of the wave number, wavelength and growth rate of the fastest growing wave from figure 9.4 and 9.5 are given in table 9.1.

59
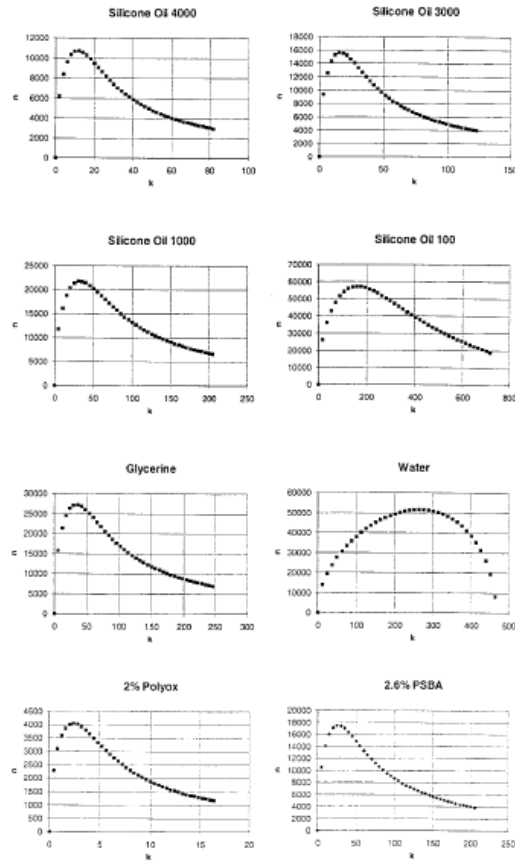
Fig. 9.4. n (sec^{-1}) vs. k (cm^{-1}) for viscous potential flow; shock Mach number $= 2$.

The parameters of the maximum growth rate computed by VPF are in excellent agreement with the exact solution.

9.6 Comparison of the measured wavelength of corrugations on the drop surface with the prediction of the stability theory

We have shown that the theoretical prediction about stability depends very strongly on viscosity and that this dependence is very well predicted by a purely irrotational theory. It remains to show that these predictions agree with experiments. JBB compared photos from their movies with the stability theory predicted in section 9.3. No special choice was made in selecting the frames for the comparisons other than choosing ones from the early part of the motion that were well focused. The wave-like structute can be identified much more easily on the computer screen than in the images reproduced in figures 1-13 of JBB. In figure 9.6 the predicted and observed wavelengths on a water drop at $M_s = 2$ and 3 are compared. The tick marks on the photos identify wave troughs so that the predicted distance between the tick marks is the length of an unstable wave. The same kind of comparison is given in figure 9.7 for silicone oil in figure 9.8 for glycerine.

In figure 9.9 (which is figure 14 in JBF) we show the analysis of RT waves can be enhanced by image processing.

Stages of breakup of water drops at $M_s = 2$ and $M_s = 3$ are shown in figures 9.10 and 9.11. RT waves appear on the front face immediately and the drop is reduced to mist in 200 μs. Very excellent photographs of the fragmentation of water drops to mist can be found in the paper of O.Engel (1958).

The agreements between theory and experiment may extend to high viscosity drop. The lengths of the most unstable waves are greater than the diameter of the drops. Waves shorter than those which grow fastest grow more slowly. The retardation of the instability of unstable waves which is predicted by theory is realized by experiments; the larger the viscosity the larger is the length of time it takes for the drop to break. Eventually they do break and the breakup looks like a bag breakup as in figure 9.10.
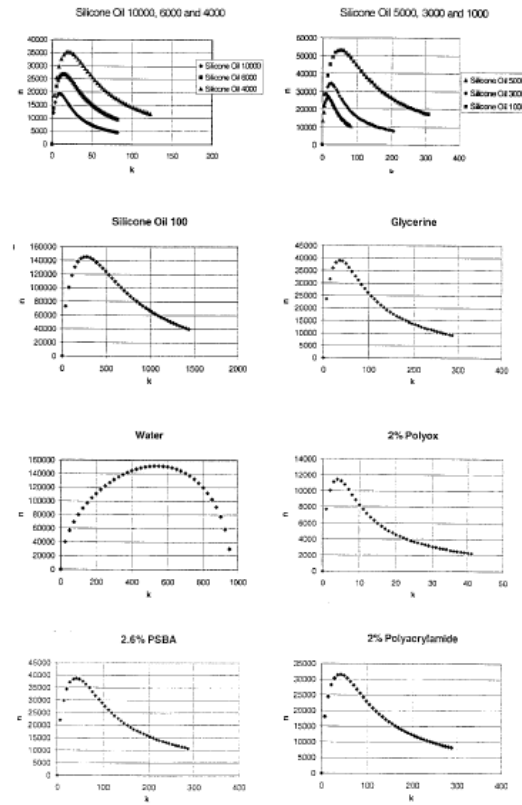
Fig. 9.5. n (sec^{-1}) vs. k (cm^{-1}) for viscous potential flow; shock Mach number $= 3$.
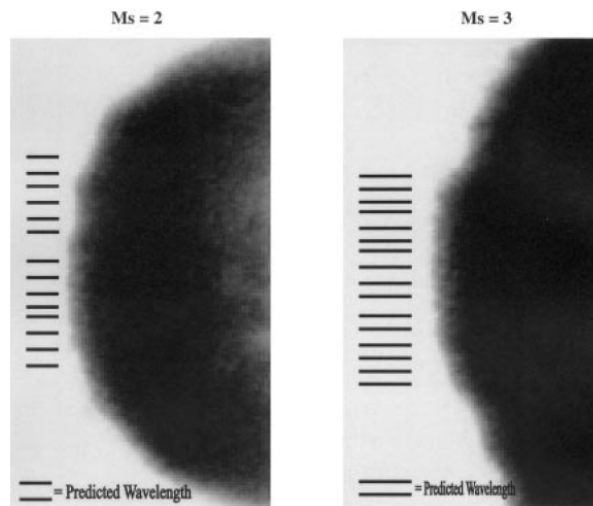
Fig. 9.6. Rayleigh-Taylor Waves in Water. The tick marks on the photographs locate wave troughs.

9.7 Fragmentation of Newtonian and viscoelastic drops

The breakup of drops in a high speed air flow is a fundamental problem of two-phase fluid and it has given rise to a large literature. Most of the early literature focuses on drops of Newtonian liquids in subsonic air streams, and is excellently reviewed by Pilch & Erdman (1987), and Hsiang and Faeth (1992). Shock tube studies of the breakup of Newtonian drops, usually water, under high subsonic and supersonic conditions were carried out by Hanson and Domich (1956), Engel (1958), Hanson, Domich, & Adams (1963), Ranger and Nicholls (1969), Reinecke & McKay (1969), Reinecke & Waldman (1970, 1975), Waldman, Reinecke & Glenn (1972), Simpkins & Bales (1972), Wierzba and Takayama (1988), Yoshida & Takayama (1990), Hirahara and Kawahashi (1992),

Table 9.1. *Values of the wave number, wave length, and growth rate of the most dangerous wave for the experimental conditions given in tables 1 and 2 of JBB.*

Liquid	Viscosity	Exact			Viscous Potential		
	(kg/m/s)	n (sec^{-1})	k (cm^{-1})	λ (mm)	n (sec^{-1})	k (cm^{-1})	λ (mm)
$M_s = 3$							
SO 10000	10	17790	9.5	6.61	19342	9.7	6.48
SO 6000	6	24673	14.45	4.35	26827	14.7	4.27
SO 5000	5	24787	15.86	3.96	26951	16.15	3.89
SO 4000	4	32550	20.3	3.10	35312	20.7	3.04
SO 3000	3	31507	23.08	2.72	34257	23.5	2.67
SO 1000	1	48769	49.68	1.26	53088	50.65	1.24
SO 100	0.1	132198	253.2	0.25	143699	259	0.24
Glycerine	1.49	38760	41.3	1.52	42141	42.1	1.49
2% PO	35	10492	3.95	15.91	11406	3.95	15.91
2.6% PSBA	1.13	34460	37.8	1.66	37467	38.5	1.63
2% PAA	0.96	28927	39.4	1.59	31451	40.15	1.56
Water	0.001	149632	531.95	0.12	151758	540.8	0.12
$M_s = 2$							
SO 4000	4	9868	11.2	5.61	10729	11.4	5.51
SO 3000	3	14388	15.6	4.03	15644	15.9	3.95
SO 1000	1	20018	31.8	1.98	21765	32.4	1.94
SO 100	0.1	52726	158	0.40	57304	161.9	0.39
Glycerine	1.49	25046	33.2	1.89	27231	33.8	1.86
2% PO	35	3723	2.35	26.74	4048	2.4	26.18
2.6% PSBA	1.13	16070	25.75	2.44	17472	26.25	2.39
Water	0.001	50971	260.9	0.24	51507	264.2	0.24
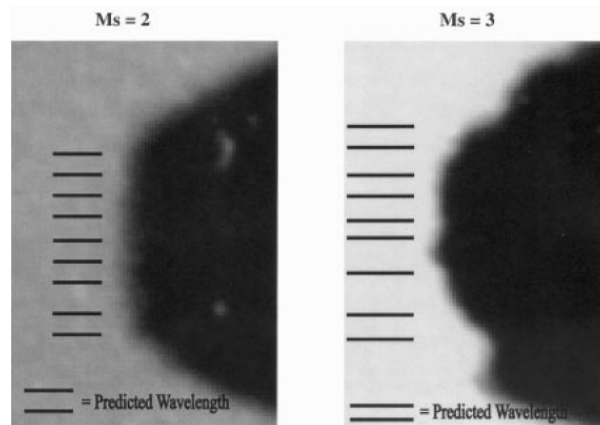
Fig. 9.7. Rayleigh-Taylor Waves in Silicone Oil (0.1 kg/msec). The tick marks on the photographs locate wave troughs.

and others. The excellent study of Engel (1958) showed that water drops of millimeter diameter would be reduced to mist by the flow behind an incident shock moving at Mach numbers in the range 1.3 to 1.7. Many of the other aforementioned studies allude to the presence of large amounts of mist. Joseph, Huang and Candler (1996) argued that mist could arise from condensed vapor under flash vaporization due to (1) low pressures at the leeside produced by rarefaction and drop acceleration, (2) high tensions produced by extensional motions in the liquid stripped from the drop, (3) the frictional heating by rapid rates of deformation, and (4) the heating of sheets and filaments torn from the drop by hot air. Though mist and vapor formation is not the focus of this study, it is relevant that the Rayleigh-Taylor instability pumps fingers of hot gas, behind the shock, into the drop increasing both the frictional heating and the area of liquid surface exposed to hot gas. The recent and fairly extensive literature on atomization is well represented in the papers by Hsiang and Faeth (1992), Hwang, Liu and Rietz (1996), and Faeth (1996). These results, and earlier drop breakup studies such as Krzeczkowski (1980), Wierzba (1990), Kitscha and Kocamustafaogullari (1989), and Stone (1994), are restricted to relatively low Weber and Reynolds numbers. The highest Weber and Reynolds data for drop breakup was reported by
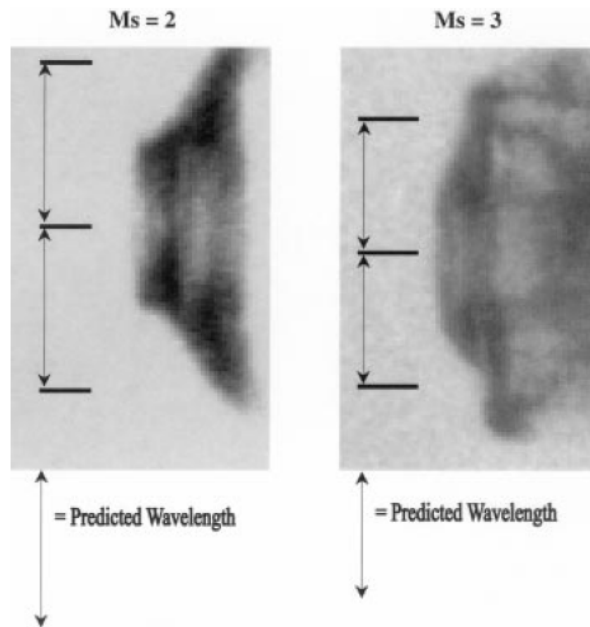
Fig. 9.8. Rayleigh-Taylor waves in glycerine. The tick marks on the photographs locate wave troughs.

Hsiang and Faeth (1992) who worked under conditions for which the Weber numbers ranged from 0.5 to 1000 with Reynolds numbers from 300 to 1600.

High Weber number drop breakup data were obtained by Engel (1958), Ranger and Nichols (1969), and Reinecke and Waldman (1970) for air and water only, so viscous effects could not be studied. In contrast, the data presented here cover a wide range of viscosities (from 0.001 to 35 kg/m sec) and a wide range of high Weber numbers (from 11,700 to 169,000), Ohnesorge numbers (from 0.002 to 82.3) and Reynolds numbers (from 40,000 to 127,600), based on the free stream conditions. Another feature which distinguishes the experiments of JBB from previous ones is that they recorded all of the data as real time movies which may be seen under 'video animations' at the Web address http://www.aem.umn.edu/research/Aerodynamic_Breakup/. The movies capture events which were previously unknown, such as bag breakup and bag-and-stamen breakup of high viscosity drops at very high Weber numbers, whereas short wave Rayleigh-Taylor corrugations appear on water drops under similar free stream conditions.

Only a few studies of the breakup of viscoelastic drops have been published; Lane (1951), Wilcox, June, Braun and Kelly (1961), Matta and Tytus (1982), and Matta, Tytus and Harris (1983). Matta and co-workers did studies at Mach numbers near one and less. They showed that threads and ligaments of liquid arise immediately after breakup, rather than the droplets which are seen in Newtonian liquids. Breakup of viscoelastic drops are shown in figure 9.9 and in many photographs shown by JBF 2002.

9.8 Modelling Rayleigh-Taylor instability of a sedimenting suspension of several thousand circular particles in a direct numerical simulation

Pan, Joseph and Glowinski (2000) studied the sedimentation of several thousand circular particles in two dimensions using the method of distributed Lagrange multipliers for solidliquid flow. The simulation gives rise to fingering which resembles Rayleigh-Taylor instabilities. The waves have a well-defined wavelength and growth rate which can be modelled as a conventional Rayleigh-Taylor instability of heavy fluid above light. The heavy fluid is modelled as a composite solid-liquid fluid with an effective composite density and viscosity. Surface tension cannot enter this problem and the characteristic shortwave instability is regularized by the viscosity of the solid-liquid dispersion. The dynamics of the Rayleigh-Taylor instability are studied using viscous potential flow, generalizing work of JBB to a rectangular domain bounded by solid walls; an exact solution is obtained. The model shows the same trends as the simulation but it allows the effective fluid to slip at the side-walls. The model with slip at the side walls is very easily constructed, but an analytic solution with no-slip at the side wall
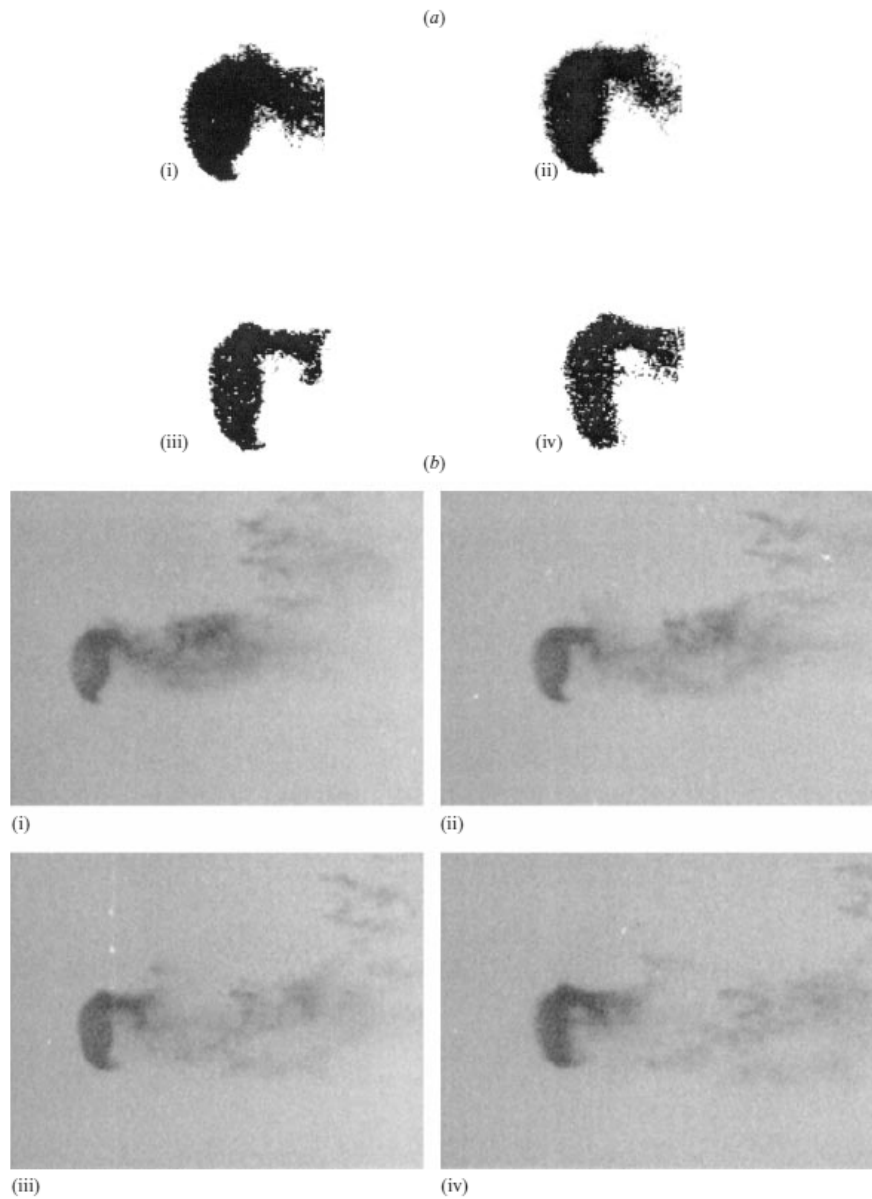
Fig. 9.9. (JBF, figure 14) (a) Rayleigh-Taylor waves in 2% aqueous polyox in the flow behind a Mach 2.9 shockwave. Time (in μs) after passage of shock: (i) 30, (ii) 35, (iii) 40, (iv) 45. (b) Movie frames corresponding to the contrast-enhanced images of (a).

is not known and apparently cannot be found by the method of separation of variables. It is probable that the numerical simulation would be better modeled by continuum model with no-slip at side walls.

Sample pictures of the simulation are shown in figures 9.13 and 9.14. The formation of RT instability follows the acceleration guidelines in the cartoon of fgure 9.1(e); the top surface is flat ad the bottom one is corrugated.
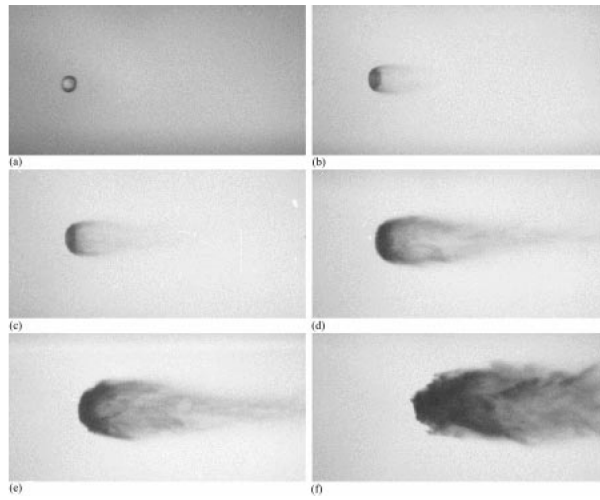
Fig. 9.10. Stages in the breakup of a water drop (diameter = 2.6 mm) in the flow behind a Mach 2 shock wave. Air velocity = 432 m/s; dynamic pressure = 158.0 kPa; Weber No. = 11,700. Time (μs): (a) 0, (b) 45, (c) 70, (d) 135, (e) 170, (f) 290.
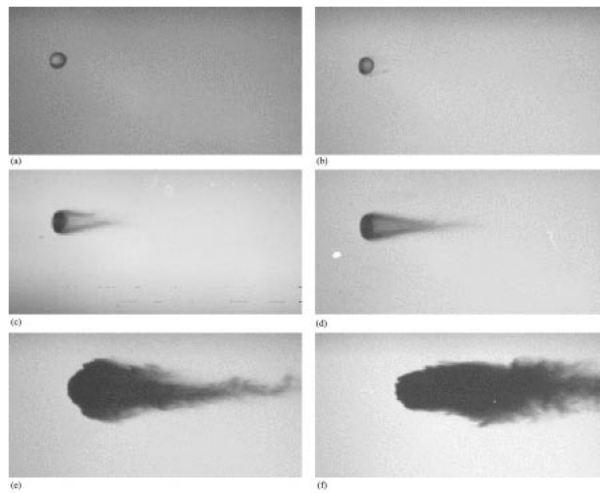
Fig. 9.11. Stages in the breakup of a water drop (diameter = 2.5 mm) in the flow behind a Mach 3 shock wave. Air velocity = 764 m/s; dynamic pressure = 606.4 kPa; Weber No. = 43,330. Time (μs): (a) 0, (b) 15, (c) 30, (d) 40, (e) 95, (f) 135.
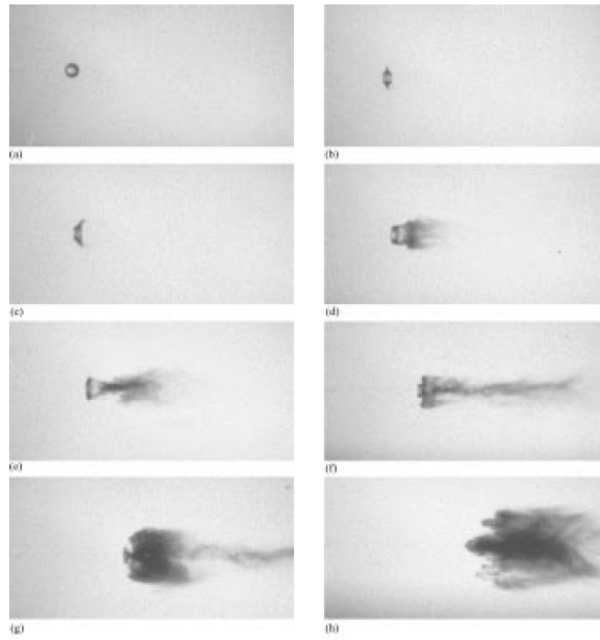
Fig. 9.12. Stages in the breakup of a drop of glycerine (diameter = 2.4 mm) in the flow behind a Mach 3 shock wave. Air velocity = 758 m/s; dynamic pressure = 554.0 kPa; Weber No. = 42,220. Time (μs): (a) 0, (b) 35, (c) 50, (d) 70, (e) 90, (f) 125, (g) 150, (h) 185.

Square   Hexagonal   Rectangular
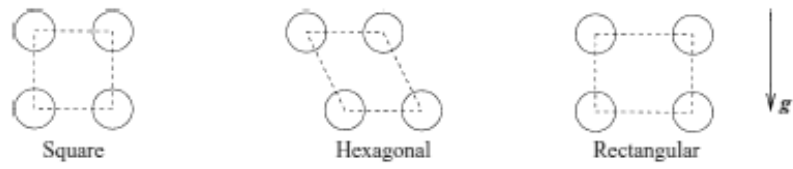
FIGURE 1. Initial lattices.

$(a) t = 0$

$(b) t = 0.476$

$(c) t = 0.476$
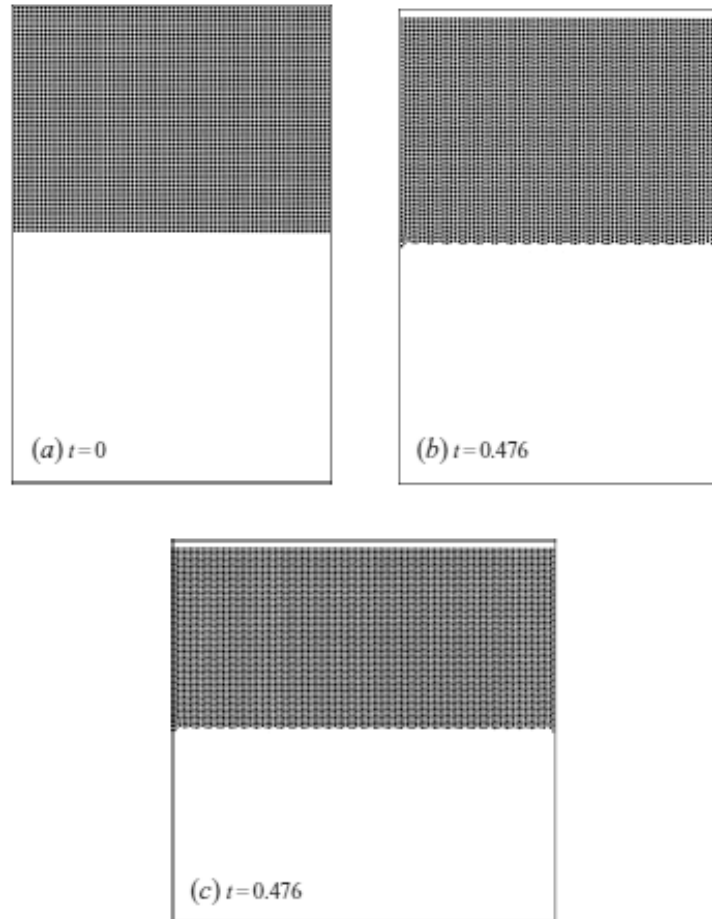
Fig. 9.13. Snapshots of the sedimentation of 5040 (a; b, $W = 8$ cm) and 7560 (c, $W = 12$ cm) disks of diameter 14/192 cm in two dimensions. The initial lattice is square.
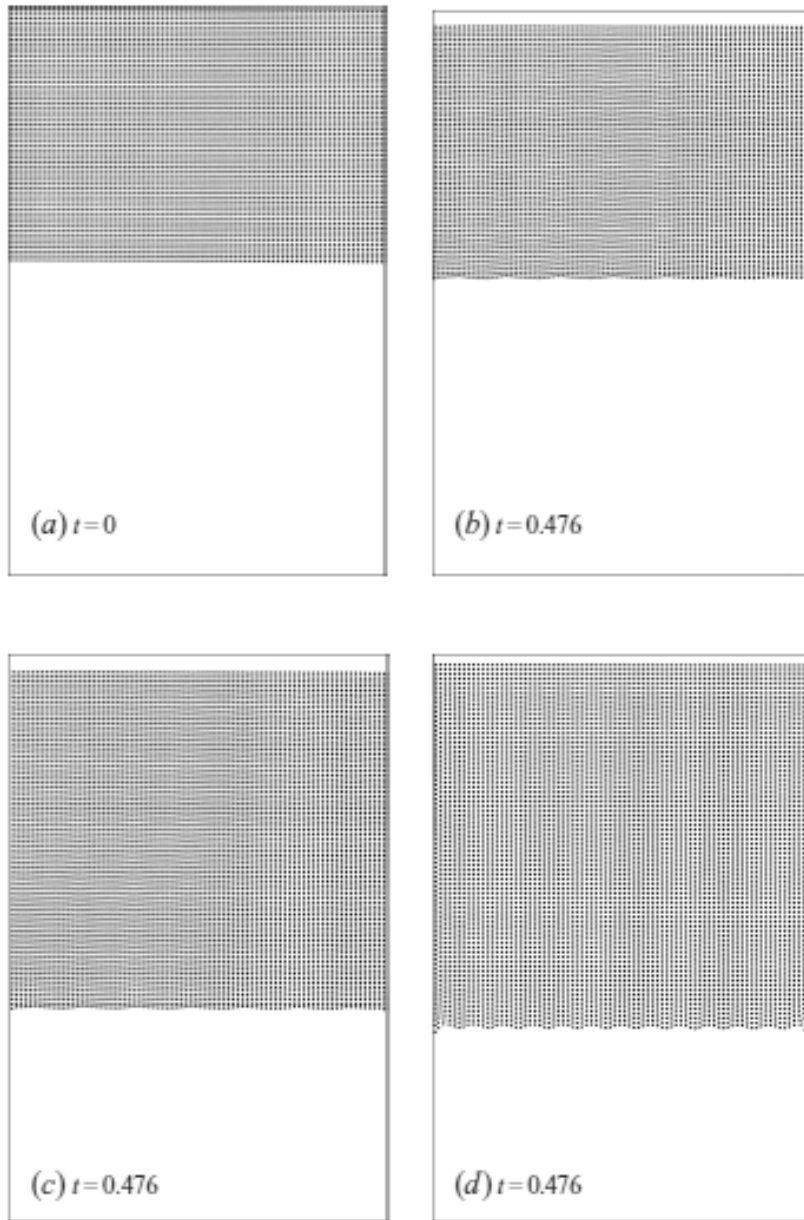
Fig. 9.14. Snapshots of the sedimentation of 4800 (a; b) and 6400 (c; d) disks in two dimensions ($W = 8$ cm). The diameter of disks in (a), (b) and (c) is 10/192 cm and the diameter of disks in (d) is 16/192 cm. The initial lattice is rectangular.

10

The force on a cylinder near a wall in viscous potential flows

We study the force on a two-dimensional cylinder near a wall in two potential flows: the flow due to the circulation $2\pi\kappa$ about the cylinder and the uniform streaming flow with velocity V past the cylinder. The pressure is computed using the Bernoulli equation and the viscous normal stress is calculated using viscous potential flow; the shear stress is ignored. The forces on the cylinder are computed by integration of the normal stress over the surface of the cylinder. In both of the two cases, the force perpendicular to the wall (lift) is only due to the pressure and the force parallel to the wall (drag) is only due to the viscous normal stress. Our results show that the drag on a cylinder near a wall is larger than on a cylinder in an unbounded domain. In the flow induced by circulation or in the streaming flow, the lift force is always pushing the cylinder towards the wall. However, when the two flows are combined, the lift force can be pushing the cylinder away from the wall or towards the wall.

10.1 The flow due to the circulation about the cylinder

Figure 10.1 shows a cylinder with radius a near the wall $x = 0$. Let b be the distance of the axis of the cylinder from the wall and $c = OP$ where OP is the tangent of the cylinder. The complex potential for the flow due to the anti-clockwise circulation $2\pi\kappa$ about the cylinder is (Milne-Thomson, 1968 §6.53)

$$\omega = -2\kappa\cot^{-1}\frac{\imath z}{c}. \tag{10.1.1}$$

To facilitate the calculation, we introduce a parameter η, so that

$$a = c\operatorname{csch}\eta \quad \text{and} \quad b = c\coth\eta. \tag{10.1.2}$$
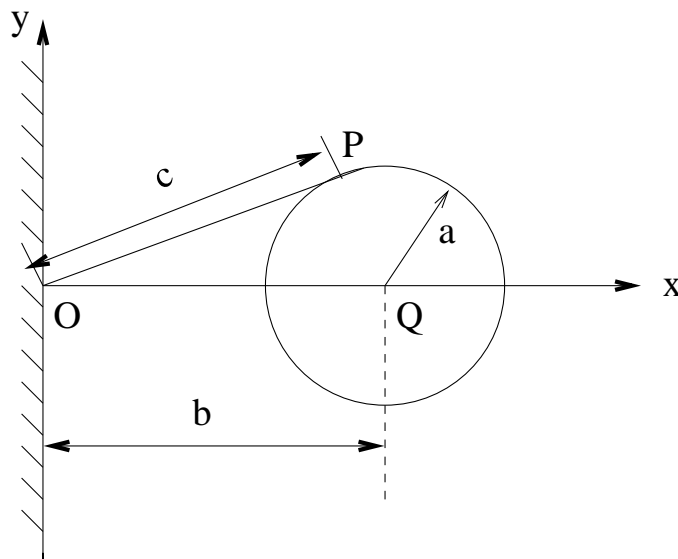
Fig. 10.1. A cylinder with radius a near the wall $x = 0$.

We can also express c and η in terms of a and b:

$$c = \sqrt{b^2 - a^2} \quad \text{and} \quad \eta = \cosh^{-1}(b/a). \tag{10.1.3}$$

The complex velocity is

$$u - \imath v = \frac{d\omega}{dz} = \frac{2\imath c\kappa}{c^2 - z^2}. \tag{10.1.4}$$

We separate the real and imaginary parts of the velocity to obtain

$$u = \frac{-4c\kappa xy}{(c^2 - x^2 + y^2)^2 + 4x^2 y^2} \quad \text{and} \quad v = \frac{-2c\kappa(c^2 - x^2 + y^2)}{(c^2 - x^2 + y^2)^2 + 4x^2 y^2}. \tag{10.1.5}$$

The pressure can be computed using the Bernoulli equation

$$p + \rho|u|^2/2 = \text{Const} \Rightarrow -p = \rho|u|^2/2 - \text{Const}. \tag{10.1.6}$$

The rate of strain tensor can be evaluated

$$2\mathbf{D} = \begin{bmatrix} 2\partial u/\partial x & \partial u/\partial y + \partial v/\partial x \\ \partial u/\partial y + \partial v/\partial x & 2\partial v/\partial y \end{bmatrix}. \tag{10.1.7}$$

The surface of the cylinder can be expressed as

$$x = c\coth\eta + c\operatorname{csch}\eta\cos\theta, \quad y = c\operatorname{csch}\eta\sin\theta, \tag{10.1.8}$$

where $0 \leqslant \theta \leqslant 2\pi$. The normal on the surface of the cylinder is

$$\mathbf{n} = \cos\theta\mathbf{e}_x + \sin\theta\mathbf{e}_y. \tag{10.1.9}$$

The viscous normal stress at the surface is

$$\tau_{nn} = \mathbf{n} \cdot 2\mu\mathbf{D} \cdot \mathbf{n} = 2\mu\left[\frac{\partial u}{\partial x}\cos^2\theta + \left(\frac{\partial u}{\partial y} + \frac{\partial v}{\partial x}\right)\sin\theta\cos\theta + \frac{\partial v}{\partial y}\sin^2\theta\right]$$
$$= \frac{-2\mu\kappa\sin\theta\sinh^3\eta}{c^2\left(\cos\theta + \cosh\eta\right)^2}, \tag{10.1.10}$$

and the pressure at the surface is

$$-p = \frac{\rho}{2}\frac{\kappa^2\sinh^4}{c^2\left(\cos\theta + \cosh\eta\right)^2} - \text{Const}. \tag{10.1.11}$$

The forces on the cylinder by the normal stress are

$$F_x = \int_0^{2\pi}(-p + \tau_{nn})\cos\theta\, c\operatorname{csch}\eta\, d\theta, \quad F_y = \int_0^{2\pi}(-p + \tau_{nn})\sin\theta\, c\operatorname{csch}\eta\, d\theta. \tag{10.1.12}$$

We calculate the contributions to the forces by the pressure and viscous stress separately. The superscript "p" and "v" stand for pressure and viscous stress, respectively. The forces by the pressure are

$$F_x^{\text{p}} = \int_0^{2\pi}\frac{\rho\kappa^2\sinh^3\eta}{2c}\frac{\cos\theta\, d\theta}{\left(\cos\theta + \cosh\eta\right)^2} = -\frac{\pi\rho\kappa^2}{c}, \tag{10.1.13}$$

$$F_y^{\text{p}} = \int_0^{2\pi}\frac{\rho\kappa^2\sinh^3\eta}{2c}\frac{\sin\theta\, d\theta}{\left(\cos\theta + \cosh\eta\right)^2} = 0, \tag{10.1.14}$$

which agree with the values computed using the theorem of Blasius (Milne-Thomson, 1968 §6.53). The forces by the viscous stress are

$$F_x^{\text{v}} = \int_0^{2\pi} -\frac{2\mu\kappa\sinh^2\eta}{c}\frac{\sin\theta\cos\theta\, d\theta}{\left(\cos\theta + \cosh\eta\right)^2} = 0, \tag{10.1.15}$$

$$F_y^{\text{v}} = \int_0^{2\pi} -\frac{2\mu\kappa\sinh^2\eta}{c}\frac{\sin\theta\sin\theta\, d\theta}{\left(\cos\theta + \cosh\eta\right)^2} = -\frac{2\pi\mu\kappa}{c}\left(1 - \mathrm{e}^{-2\eta}\right). \tag{10.1.16}$$
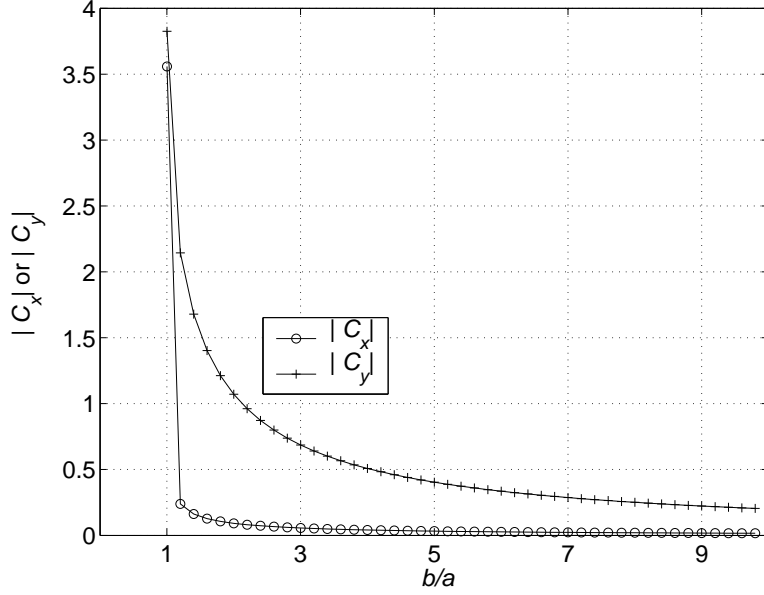
Fig. 10.2. The absolute values of the coefficients for the force $|C_x|$ and $|C_y|$ as functions of the ratio b/a. The Reynolds number is taken as 1 when computing C_y.

Using equation (10.1.3), the forces can be expressed in terms of a and b:

$$F_x = F_x^{\mathrm{p}} + F_x^{\mathrm{v}} = -\frac{\pi\rho\kappa^2}{\sqrt{b^2 - a^2}}, \tag{10.1.17}$$

$$F_y = F_y^{\mathrm{p}} + F_y^{\mathrm{v}} = -\frac{2\pi\mu\kappa}{\sqrt{b^2 - a^2}}\left(1 - \mathrm{e}^{-2\cosh^{-1}(b/a)}\right). \tag{10.1.18}$$

We define a characteristic velocity $U = 2\pi\kappa/a$ and make the forces dimensionless.

$$C_x = \frac{F_x}{\frac{1}{2}\rho U^2 a} = -\frac{1}{2\pi\sqrt{(b/a)^2 - 1}}, \tag{10.1.19}$$

$$C_y = \frac{F_y}{\frac{1}{2}\rho U^2 a} = -\frac{4}{R_e}\frac{1}{\sqrt{(b/a)^2 - 1}}\left[1 - \mathrm{e}^{-2\cosh^{-1}(b/a)}\right], \tag{10.1.20}$$

where $R_e = \rho U 2a/\mu$ is the Reynolds number. Here C_x is a function of the ratio b/a only; C_y is a function of b/a and R_e. We plot $|C_x|$ and $|C_y|$ as functions of b/a in Figure 10.2. The Reynolds number is taken as 1 when computing C_y. When b/a approaches 1, meaning that the gap between the wall and the cylinder is very small, both of the two forces approach infinity. When b/a approaches infinity, both of the two forces approach zero, because the interaction between the cylinder and the wall is negligible.

10.2 The streaming flow past the cylinder near a wall

The domain is bounded by the plane $x = 0$ and the cylinder $(x - b)^2 + y^2 = a^2$ (Figure 10.1). The uniform flow with the velocity V at infinity is streaming in the negtive direction of the y axis. The complex potential for the flow is (Milne-Thomson, 1968 p. 185)

$$\omega = \imath V z - 2\imath V a^2 z \left[\frac{1}{z^2 - b^2} + \sum_{n=1}^{\infty} \frac{a^{2n}}{\prod_{r=0}^{n-1}(b + x_r)^2 (z^2 - x_n^2)}\right], \tag{10.2.1}$$

where $x_0 = b$, $x_n = b - a^2/(b + x_{n-1})$. The potential is represented by an infinite series which converges rapidly for moderate or large values of the ratio b/a. To carry out the calculation, we consider the terms up to $n = 3$ in (10.2.1):

$$\omega = \imath V z - 2\imath V a^2 z \left[\frac{1}{z^2 - b^2} + \frac{a^2}{\beta_1(z^2 - x_1^2)} + \frac{a^4}{\beta_2(z^2 - x_2^2)} + \frac{a^6}{\beta_3(z^2 - x_3^2)}\right] \tag{10.2.2}$$

71

where

$$x_1 = b - \frac{a^2}{2b}, \quad x_2 = b - \frac{a^2}{2b - a^2/(2b)}, \quad x_3 = b - \frac{a^2}{2b - \frac{a^2}{2b - a^2/(2b)}}; \tag{10.2.3}$$

$$\beta_1 = (2b)^2, \quad \beta_2 = (2b)^2 \left(2b - \frac{a^2}{2b}\right)^2, \quad \beta_3 = (2b)^2 \left(2b - \frac{a^2}{2b}\right)^2 \left[2b - \frac{a^2}{2b - a^2/(2b)}\right]^2. \tag{10.2.4}$$

The complex velocity is $\mathrm{d}\omega/\mathrm{d}z$ and we separate the real and imaginary parts of it to obtain the velosities in x and y directions.

$$
\begin{aligned}
u = &- \frac{4a^2 V xy}{(x^2 - y^2 - b^2)^2 + 4x^2 y^2} - \frac{4a^4 V xy}{\beta_1 [(x^2 - y^2 - x_1^2)^2 + 4x^2 y^2]} \\
&- \frac{4a^6 V xy}{\beta_2 [(x^2 - y^2 - x_2^2)^2 + 4x^2 y^2]} - \frac{4a^8 V xy}{\beta_3 [(x^2 - y^2 - x_3^2)^2 + 4x^2 y^2]} \\
&+ \frac{8a^2 V xy \left[(x^2 + y^2)^2 - b^4\right]}{(b^4 - 2b^2 x^2 + x^4 + 2b^2 y^2 - 6x^2 y^2 + y^4)^2 + 16 x^2 y^2 (x^2 - y^2 - b^2)^2} \\
&+ \frac{a^2}{\beta_1} \frac{8a^2 V xy \left[(x^2 + y^2)^2 - x_1^4\right]}{[(x_1^4 - 2x_1^2 x^2 + x^4 + 2x_1^2 y^2 - 6x^2 y^2 + y^4)^2 + 16 x^2 y^2 (x^2 - y^2 - x_1^2)^2]} \\
&+ \frac{a^4}{\beta_2} \frac{8a^2 V xy \left[(x^2 + y^2)^2 - x_2^4\right]}{[(x_2^4 - 2x_2^2 x^2 + x^4 + 2x_2^2 y^2 - 6x^2 y^2 + y^4)^2 + 16 x^2 y^2 (x^2 - y^2 - x_2^2)^2]} \\
&+ \frac{a^6}{\beta_3} \frac{8a^2 V xy \left[(x^2 + y^2)^2 - x_3^4\right]}{[(x_3^4 - 2x_3^2 x^2 + x^4 + 2x_3^2 y^2 - 6x^2 y^2 + y^4)^2 + 16 x^2 y^2 (x^2 - y^2 - x_3^2)^2]};
\end{aligned}
\tag{10.2.5}
$$

$$
\begin{aligned}
v = &- V + \frac{2a^2 V (x^2 - y^2 - b^2)}{(x^2 - y^2 - b^2)^2 + 4x^2 y^2} + \frac{2a^4 V (x^2 - y^2 - x_1^2)}{\beta_1 [(x^2 - y^2 - x_1^2)^2 + 4x^2 y^2]} \\
&+ \frac{2a^6 V (x^2 - y^2 - x_2^2)}{\beta_2 [(x^2 - y^2 - x_2^2)^2 + 4x^2 y^2]} + \frac{2a^8 V (x^2 - y^2 - x_3^2)}{\beta_3 [(x^2 - y^2 - x_3^2)^2 + 4x^2 y^2]} \\
&- \frac{4a^2 V [b^4 (x^2 - y^2) - 2b^2 (x^2 + y^2)^2 + (x^2 - y^2)(x^2 + y^2)^2]}{(b^4 - 2b^2 x^2 + x^4 + 2b^2 y^2 - 6x^2 y^2 + y^4)^2 + 16 x^2 y^2 (x^2 - y^2 - b^2)^2} \\
&- \frac{a^2}{\beta_1} \frac{4a^2 V [x_1^4 (x^2 - y^2) - 2x_1^2 (x^2 + y^2)^2 + (x^2 - y^2)(x^2 + y^2)^2]}{[(x_1^4 - 2x_1^2 x^2 + x^4 + 2x_1^2 y^2 - 6x^2 y^2 + y^4)^2 + 16 x^2 y^2 (x^2 - y^2 - x_1^2)^2]} \\
&- \frac{a^4}{\beta_2} \frac{4a^2 V [x_2^4 (x^2 - y^2) - 2x_2^2 (x^2 + y^2)^2 + (x^2 - y^2)(x^2 + y^2)^2]}{[(x_2^4 - 2x_2^2 x^2 + x^4 + 2x_2^2 y^2 - 6x^2 y^2 + y^4)^2 + 16 x^2 y^2 (x^2 - y^2 - x_2^2)^2]} \\
&- \frac{a^6}{\beta_3} \frac{4a^2 V [x_3^4 (x^2 - y^2) - 2x_3^2 (x^2 + y^2)^2 + (x^2 - y^2)(x^2 + y^2)^2]}{[(x_3^4 - 2x_3^2 x^2 + x^4 + 2x_3^2 y^2 - 6x^2 y^2 + y^4)^2 + 16 x^2 y^2 (x^2 - y^2 - x_3^2)^2]}.
\end{aligned}
\tag{10.2.6}
$$

We can then calculate the pressure using (10.1.6) and the rate of strain tensor using (10.1.7). At the surface of the cylinder, we have

$$x = b + a\cos\theta, \quad y = a\sin\theta, \quad \text{and} \quad \mathbf{n} = \cos\theta \mathbf{e}_x + \sin\theta \mathbf{e}_y. \tag{10.2.7}$$

The pressure and viscous normal stress at the surface are then obtained. The forces by the normal stress on the cylinder are

$$F_x = \int_0^{2\pi} (-p + \tau_{nn}) \cos\theta \, a \, \mathrm{d}\theta, \quad F_y = \int_0^{2\pi} (-p + \tau_{nn}) \sin\theta \, a \, \mathrm{d}\theta. \tag{10.2.8}$$

Again we compute the forces by the pressure and the viscous normal stress separately and using $\rho V^2 a/2$ to make the forces dimensionless. The coefficients for the forces by the pressure are

$$C_x^p = \frac{\int_0^{2\pi} (-p)\cos\theta \, a \, \mathrm{d}\theta}{\rho V^2 a/2} = \frac{\int_0^{2\pi} (\rho |u|^2/2)\cos\theta \, a \, \mathrm{d}\theta}{\rho V^2 a/2} = \frac{\int_0^{2\pi} (u^2 + v^2)\cos\theta \, \mathrm{d}\theta}{V^2}; \tag{10.2.9}$$

$$C_y^p = \frac{\int_0^{2\pi} (u^2 + v^2)\sin\theta \, \mathrm{d}\theta}{V^2}. \tag{10.2.10}$$

b/a	C_x^p	C_y^p	C_x^v	C_y^v
1.05	-10.20	0	0	$-67.94/R_e$
1.1	-6.656	0	0	$-65.34/R_e$
1.2	-3.712	0	0	$-61.82/R_e$
1.3	-2.438	0	0	$-59.54/R_e$
1.5	-1.307	0	0	$-56.74/R_e$
2.0	-0.4595	0	0	$-53.64/R_e$
10	-3.16×10^{-3}	0	0	$-50.4/R_e$
30	-1.16×10^{-4}	0	0	$-50.28/R_e$

Table 10.1. *The coefficients for the forces on the cylinder by the pressure and the normal viscous stress obtained from numerical integration.*

The coefficients for the forces by the normal viscous stress are

$$C_x^v = \frac{\int_0^{2\pi} \tau_{nn} \cos\theta \, a \, d\theta}{\rho V^2 a/2}$$

$$= \frac{8}{R_e} \int_0^{2\pi} \left[\frac{\partial u}{\partial x} \cos^2\theta + \left(\frac{\partial u}{\partial y} + \frac{\partial v}{\partial x} \right) \sin\theta\cos\theta + \frac{\partial v}{\partial y} \sin^2\theta \right] \cos\theta \, a \, d\theta/V; \qquad (10.2.11)$$

$$C_y^v = \frac{8}{R_e} \int_0^{2\pi} \left[\frac{\partial u}{\partial x} \cos^2\theta + \left(\frac{\partial u}{\partial y} + \frac{\partial v}{\partial x} \right) \sin\theta\cos\theta + \frac{\partial v}{\partial y} \sin^2\theta \right] \sin\theta \, a \, d\theta/V, \qquad (10.2.12)$$

where $R_e = \rho V 2a/\mu$. Since the the expressions for the pressure and the viscous normal stress are very complicated, analytical expressions for C_x^p, C_y^p, C_x^v, and C_y^v are not obtained. Instead, numerical integration is used to obtain the values of these coefficients. We list the results of numerical integrations in Table 10.1.

Table 10.1 shows that C_y^p and C_x^v are both zero; in other words, the lift force in x direction is only due to the pressure and the drag in y direction is only due to the viscous normal stress. The lift force is in the negative x direction, pushing the cylinder towards the wall. This is because the velocity of the fluid in the gap between the cylinder and the wall is larger than that of exterior fluid, inducing a pressure gradient which gives rise to the lift force. The lift force has the largest magnitude when the gap between the cylinder and the wall is small ($b/a \sim 1$); it approaches zero when the cylinder is far away from the wall ($b/a \gg 1$). The drag is in the negative y direction and its magnitude decreases as b/a increases. When the cylinder is far away from the wall, the magnitude of the drag appoaches an asymptotic value $16\pi/R_e \simeq 50.265/R_e$. This asymptotic value is equal to the coefficient for the drag experienced by a cylinder in an unbounded uniform streaming flow. Therefore, our results indicate that the presence of the the wall increases the drag on the cylinder; when the cylinder is closer to the wall, the magnitude of the drag is larger.

10.3 The streaming flow past a cylinder with circulation near a wall

The combination of the two potentials (10.1.1) and (10.2.1) represents the uniform flow with the velocity V at infinity past a cylinder with circulation $2\pi\kappa$ near a wall. We calculate the force on the cylinder by the normal stress. The terms up to $n = 3$ in the infinite series are kept and the potential is

$$\omega = -2\kappa \cot^{-1} \frac{\imath z}{c} + \imath V z - 2\imath V a^2 z \left[\frac{1}{z^2 - b^2} + \frac{a^2}{\beta_1(z^2 - x_1^2)} + \frac{a^4}{\beta_2(z^2 - x_2^2)} + \frac{a^6}{\beta_3(z^2 - x_3^2)} \right], \qquad (10.3.1)$$

where x_1, x_2, x_3, β_1, β_2 and β_3 are defined in (10.2.3) and (10.2.4).

The velocity of the combined potential is the sum of the velocity incuded by the circulation and that of the streaming flow. It follows that the viscous normal stress is also the sum of the two from the circulation and the streaming flow. The calculation of the pressure is slightly complicated because the non-linear term $|u|^2$ is invovled. We skip the details of the calculation since they are similar to those in the previous sections.

There are two characteristic velocities here, V from the streaming flow and $U = 2\pi\kappa/a$ from the circulation. We introduce the parameter $2\pi\kappa/(aV)$; when $2\pi\kappa/(aV) = 1$, we have $V = U$. The coefficients for the forces are defined as

$$C_x = \frac{\int_0^{2\pi} (-p + \rho|u|^2/2)\cos\theta \, a \, d\theta}{\rho V^2 a/2}, \quad C_y = \frac{\int_0^{2\pi} (-p + \rho|u|^2/2)\sin\theta \, a \, d\theta}{\rho V^2 a/2}. \qquad (10.3.2)$$

Fig. 10.3. The lift coefficient C_x as a function of the ratio b/a. The five curves correspond to five values of the parameter $2\pi\kappa/(aV)$: -1, -0.5, 0, 1 and 2.

Our calculation shows that the lift force (C_x) is only due to the pressure and the drag (C_y) is only due to the viscous normal stress, which is the same as in the previous two sections.

In the flow induced by circulation or in the streaming flow, the lift force is always pushing the cylinder towards the wall. However, when the two flows are combined, the lift force can be pushing the cylinder away from the wall or towards the wall. We plot C_x and C_y as functions of the ratio b/a in figures 10.3 and 10.4, respectively. Five values of the parameter $2\pi\kappa/(aV)$ are studied: $-1, -0.5, 0, 1$ and 2. The circulation is anti-clockwise when $2\pi\kappa/(aV)$ is positive and clockwise when $2\pi\kappa/(aV)$ is negative.

The lift force is generated by the discrepancy between the fluid velocity in the gap and the velocity in the exterior. This discrepancy is determined by the effect of the wall and the circulation. The wall effect gives rise to a larger velocity in the gap than in the exterior. The smaller the gap, the larger the wall effect. When $\kappa = 0$, there is no circulation and the wall effect leads to a negative lift force. The anti-clockwise circulation increases the velocity discrepancy generated by the wall effect. As a result, the magnitude of the lift force for $2\pi\kappa/(aV) = 1$ or 2 is larger than for $\kappa = 0$. On the contrary, the clockwise circulation offsets the velocity discrepancy by the wall effect. When the gap is small (b/a is close to 1), the fluid velocity in the gap is still larger than in the exterior but the difference is smaller due to the clockwise circulation. Therefore, the lift force for $2\pi\kappa/(aV) = -0.5$ and -1 is still negative but with a smaller magnitude than for $\kappa = 0$. As b/a becomes larger, the wall effect is weaker and could be completely balanced by the clockwise circulation, leading to a zero lift force; the corresponding b/a may be called the critical gap. The critical gaps for $2\pi\kappa/(aV) = -0.5$ and -1 are approximately $b/a = 1.5$ and 1.23, respectively. When $b/a >> 1$, the wall effect is negligible and the lift force is determined by the circulation alone. The asymptotic value of the lift force can be calculated using the well-known lift formula (Milne-Thomson, 1968 §7.12)

$$F_x = -2\pi\kappa\rho V, \tag{10.3.3}$$

which is for a cylinder with circulation in an unbounded uniform streaming flow. The lift coefficient is

$$C_x = \frac{F_x}{\rho V^2 a/2} = \frac{-2\pi\kappa\rho V}{\rho V^2 a/2} = -2\frac{2\pi\kappa}{aV}. \tag{10.3.4}$$

Figure 10.3 shows that the asymptotic values are achieved in our calcultion.

The sum of drags from the circulation and from the streaming flow gives the total drag. When $\kappa = 0$, the drag is due to the streaming flow alone and is negative. The anti-clockwise circulation increases the manitude of the drag whereas the clockwise circulation adds decreases it. When $b/a >> 1$, the drag from the circulation is negligible and the drag coefficient approaches the asymptotic value $16\pi/R_e \simeq 50.265/R_e$ (see figure 10.4).

We study the effects of the strength of the circulation on the lift and drag at a fixed value of b/a. The lift and
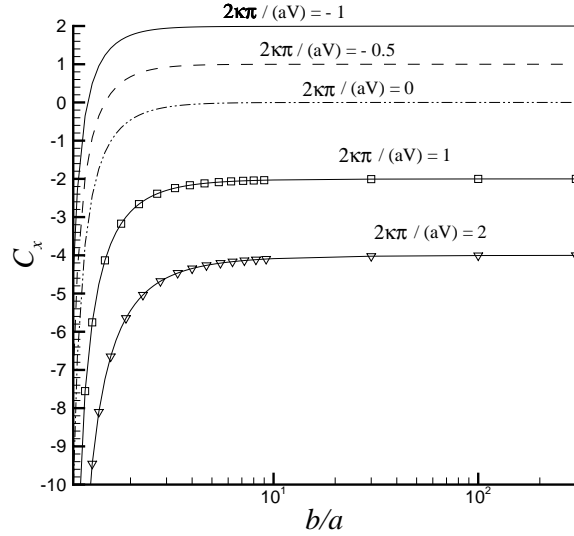
74
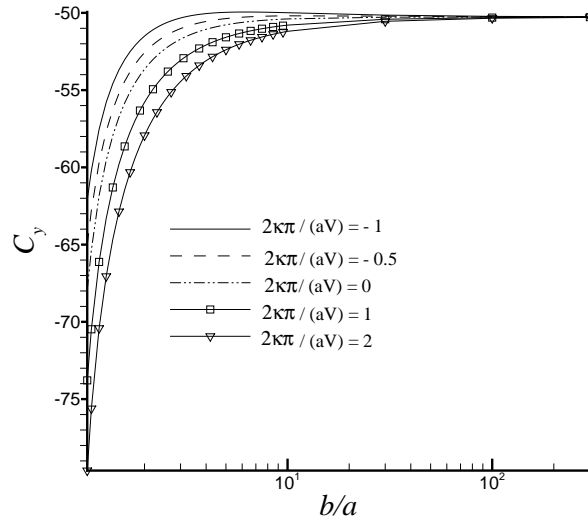
Fig. 10.4. The drag coefficient C_y as a function of the ratio b/a. The five curves correspond to five values of the parameter $2\pi\kappa/(aV)$: -1, -0.5, 0, 1 and 2. The Reynolds number is taken as 1 here.
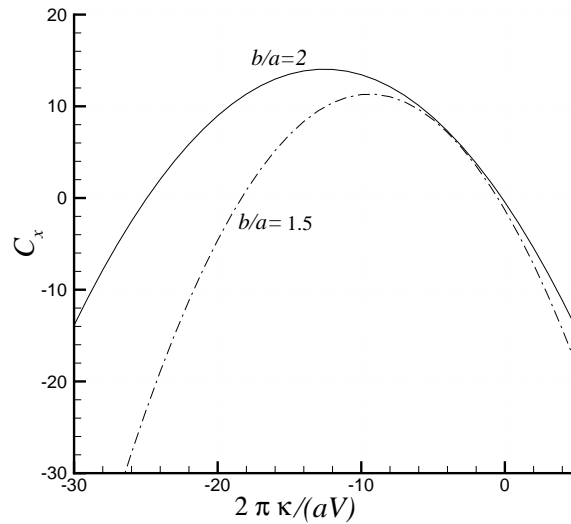
Fig. 10.5. The lift coefficient C_x as a function of $2\pi\kappa/(aV)$. The two curves are for b/a =1.5 and 2, respectively.

drag coefficients are plotted as functions of $2\pi\kappa/(aV)$ in figures 10.5 and 10.6, respectively. We note that C_x is zero at two different values of $2\pi\kappa/(aV)$ in figure 10.5. When $2\pi\kappa/(aV)$ is negative with a large magnitude, the circulation dominates and the streaming flow can be neglected. The flow in the gap is faster than in the exterior due to the wall effect, leading to a negative lift force. When $2\pi\kappa/(aV)$ is slightly smaller than zero, the streaming flow dominates. Again, the velocity discrepancy gives rise to a negative lift force. When $2\pi\kappa/(aV)$ is negative with a intermediate magnitude, the clockwise circulation overcomes the velocity discrepancy by the wall effect and the lift force is positive. The three regimes discussed above are separated by two points at which the lift force is zero. When $2\pi\kappa/(aV)$ is positive, the lift force is always negative.

The drag has contributions from the circulation and the streaming flow. The part from streaming flow is
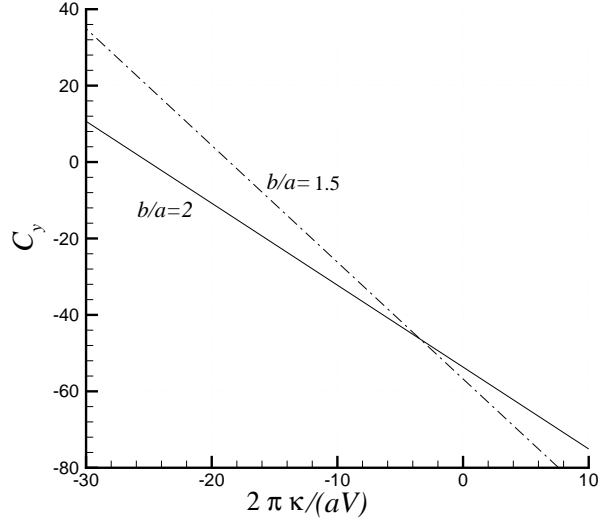
Fig. 10.6. The drag coefficient C_y as a function of $2\pi\kappa/(aV)$. The two curves are for $b/a = 1.5$ and 2, respectively. The Reynolds number is taken as 1 here.

independent of $2\pi\kappa/(aV)$; the part from the circulation is given by (10.1.18) and the dimensionless form is:

$$\frac{-2\pi\mu\kappa\left(1 - e^{-2\cosh^{-1}(b/a)}\right)/\sqrt{b^2 - a^2}}{\rho V^2 a/2} = -\frac{4}{R_e}\frac{2\pi\kappa}{aV}\frac{\left(1 - e^{-2\cosh^{-1}(b/a)}\right)}{\sqrt{(b/a)^2 - 1}}, \tag{10.3.5}$$

where $R_e = \rho V 2a/\mu$. It is clear from (10.3.5) that when b/a and R_e are fixed, the drag coefficient has a linear relationship with $2\pi\kappa/(aV)$, which can be seen in figure 10.6. The drag by the streaming flow is negative; its magnitude can be increased by a anti-clockwise circulation ($2\pi\kappa/(aV) > 0$) or decreased by a clockwise circulation ($2\pi\kappa/(aV) < 0$). When $2\pi\kappa/(aV)$ is negative with a large magnitude, the sign of the drag is changed to positve.

11
Kelvin-Helmholtz instability

The instability of uniform flow of incompressible fluids in two horizontal parallel infinite streams of different velocities and densities, is known as the Kelvin-Helmholtz (KH) instability. It is usual to study this instability by linearizing the nonlinear equations around the basic uniform flow followed by analysis of normal modes proportional to

$$\exp\left(\sigma t + \imath k x\right). \tag{11.0.1}$$

It is also usual to assume that the fluids are inviscid; if they were viscous the discontinuity of velocity could not persist. Moreover, if the basic streams are assumed uniform, then there are no rigorous ways to evaluate the shear and interfacial stresses. In practice, the streams being modeled are turbulent and analytic studies of stability must make approximations. The usual procedure adopted by many authors whose work has been reviewed by Mata *et al.* (2002) is to employ empirical correlations for the evaluation of shear and interfacial stress. The agreement with experiments achieved by this empirical approach is not compelling.

The study of KH instability using viscous potential flow does not allow for no-slip conditions or interfacial stresses but unlike the inviscid theory, the normal viscous stresses are well represented. There is an important viscous resistance to the up and down motion of the waves independent of the action of shear stresses.

The KH instability is produced by the action of pressures on the perturbed interface; the instability is often discussed as being due to shear, but shear stresses are not the major actor here and in any event could not be inserted into an analysis based on potential flow even when viscosity is not neglected.

The formation of the instability may be described in terms of the action of pressure in Bernoulli equation which is small where the speed is great (at the top in figure 11.1) and large where it is small (in troughs).

An example of the KH instability due to wind shear in the atmosphere is shown in figure 11.2.
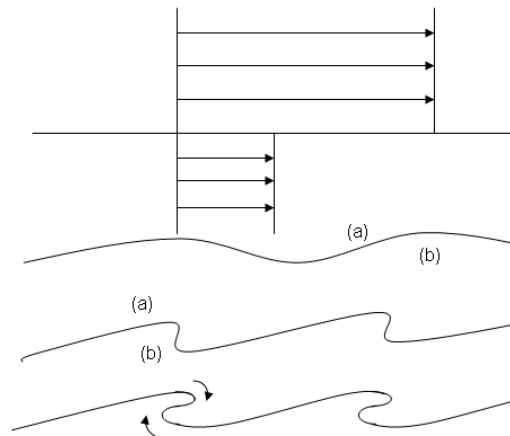
Fig. 11.1. The speed of the fluid above is greater. The pressure is greater at crests (a) than at troughs (b). The upper part of the interface is carried by upper fluid causing the interface to overturn.

Fig. 11.2. A KH instability rendered visible by clouds over Mount Duval in Australia.

11.1 KH instability on an unbounded domain

The instability corresponding to figure 11.1 was considered by Drazin and Reid (1981) the fluids are inviscid and the flows irrotational. The flow domain is not bounded so that perturbations decay far away from the interface. Their analysis combines RT and KH instabilities which are very different kinds of instability. In particular, RT instability can occur in a vacuum but the pressures from the ambient in KH instability cannot be neglected.

Funada and Joseph (2001) did the analysis when the fluid is viscous and the flow is irrotational and bounded in a channel. They confined their attention to the case in which air is above and RT instability for heavy fluid above does not occur. The results of Drazin and Reid can be obtained from the formulas of Funada and Joseph which are developed in sections which follow.

The dispersion relation for the stability analysis when the flow is irrotational and the fluids are viscous can be obtained by following the analysis of Drazin and Reid (1981). The pressure balance is replaced by a viscous normal stress balance:

$$p'_a - 2\mu_a \frac{\partial w'_a}{\partial z} = p'_l - 2\mu_l \frac{\partial w'_l}{\partial z}, \tag{11.1.1}$$

and taking the perturbation in the form of functions of z (the normal direction) times $\exp(\sigma t + \imath k x)$, we find the dispersion relation

$$(\rho_a + \rho_l)\,\sigma^2 + 2\sigma \left[\imath k\left(\rho_a U_a + \rho_l U_l\right) + k^2\left(\mu_a + \mu_l\right)\right] - k^2\left(\rho_a U_a^2 + \rho_l U_l^2\right)$$
$$+ 2\imath k^3\left(\mu_a U_a + \mu_l U_l\right) + \left(\rho_l - \rho_a\right)gk + \gamma k^3 = 0 \tag{11.1.2}$$

where ρ, μ, U are respectively density, viscosity, velocity; γ is surface tension and g the gravitational constant. Gravity acts downward from side a towards side l. The real part of σ is the growth rate given as a function of the wave number k.

11.2 Maximum growth rate, Hadamard instability, neutral curves

Equation (11.0.1) may be written as

$$\exp\left(\sigma_R t\right)\exp\left[\imath\left(\sigma_I t + kx\right)\right] \tag{11.2.1}$$

where

$$\sigma_R = \sigma_R(k, \text{parameters}). \tag{11.2.2}$$

When the parameters are such that

$$\sigma_R(k) > 0, \tag{11.2.3}$$

the flow is KH unstable. When the parameters are such that

$$\sigma_R(k) = 0, \tag{11.2.4}$$

the flow is neutrally stable. Sometimes it is said that the flow is marginally stable.

78

11.2.1 Maximum growth rate

For unstable flows

$$\sigma_{Rm} = \max_{k \in \mathbb{R}} = \sigma_R(k_m). \tag{11.2.5}$$

σ_{Rm} is the maximum growth rate for a certain set of parameters and k_m is the wave number of maximum growth. The wavelength $\lambda_m = 2\pi/k_m$ for the fastest growing wave is usually observed in experiments. It is selected by nonlinear mechanisms which are not well understood.

11.2.2 Hadamard instability

Surface tension is very important; it stabilizes short waves. When $\gamma = 0$, the flow can be unstable as $k \to \infty$ or $\lambda \to 0$. If the viscosity is also zero, then the KH instability is Hadamard unstable with $e^{\alpha k t}$, $\alpha > 0$. This bad instability is worse than the RT instability which grows with $\sqrt{k}$ instead of k. Hadamard instabilities are ubiquitous in fluid mechanics; they are very important and should be a central topic in the study of hydrodynamic instabilities. However, these instabilities are not discussed in any of the standard books on hydrodynamic stability. Flows which are Hadamard unstable cannot be realistically studied by numerical methods; the finer the mesh, the worse the result.

11.2.3 The regularization of Hadamard instability

In the mathematical literature, problems which are Hadamard instability are shown to be ill-posed. A regularized problem is not catastrophically unstable to short waves; σ_{Rm} can be positive but it does not go to infinity as $k \to \infty$. Viscosity can be a regularizer. Really good regularizers, like surface tension, can stabilize short waves. The choice of regularizers should respect physics. It is not possible to present valid results for problems which are Hadamard unstable without understanding the physics which regularizes the awful instabilities. Unlike surface tension, viscosity will not cause the small waves to decay; they still grow but their growth is limited and the growth rate $\mathrm{Re}\,[\sigma(k)]$ does not go to infinity with k as in Hadamard instability. The positive growth rate is given by

$$\mathrm{Re}\,[\sigma_+] = \frac{\rho_a \mu_l^2 + \rho_l \mu_a^2}{2\left(\mu_l + \mu_a\right)^3}\left(U_a - U_l\right)^2 \quad k \to \infty.$$

11.2.4 Neutral curves

Neutral curves $|U_a - U_l|$ versus k for $\sigma_R = 0$ and growth rate curves for an unstable value of $|U_a - U_l|$ are plotted in figures 11.3 and 11.4.

11.3 KH instability in a channel

Funada and Joseph (2001) studied the stability of stratified gas-liquid flow in a horizontal rectangular channel using viscous potential flow. The analysis leads to an explicit dispersion relation in which the effects of surface tension and viscosity on the normal stress are not neglected but the effect of shear stresses is neglected. Formulas for the growth rates, wave speeds and neutral stability curve are given in general and applied to experiments in air-water flows. The effects of surface tension are always important and determine the stability limits for the cases in which the volume fraction of gas is not too small. The stability criterion for viscous potential flow is expressed by a critical value of the relative velocity. The maximum critical value is when the viscosity ratio is equal to the density ratio; surprisingly the neutral curve for this viscous fluid is the same as the neutral curve for inviscid fluids. The maximum critical value of the velocity of all viscous fluids is given by inviscid fluids. For air at 20°C and liquids with density $\rho = 1$ g/cm^3 the liquid viscosity for the critical conditions is 15 cp; the critical velocity for liquids with viscosities larger than 15 cp is only slightly smaller but the critical velocity for liquids with viscosities smaller than 15 cp, like water, can be much lower. The viscosity of the liquid has a strong effect on the growth rate. The viscous potential flow theory fits the experimental data for air and water well when the gas fraction is greater than about 70%. It predicts the transition from smooth stratified to wavy stratified flow in a 0.508 m diameter flow loop with air and 0.480 Pa s lube oil.
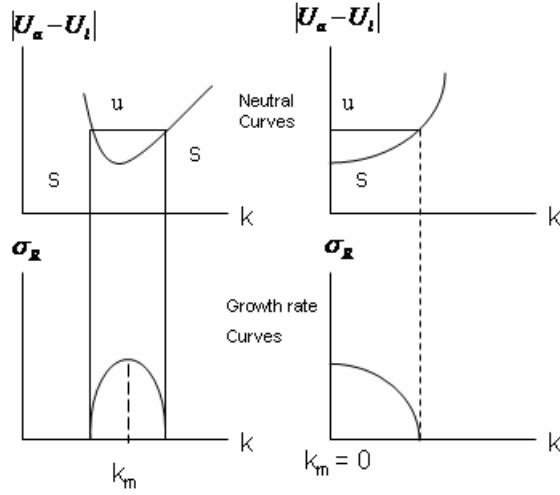
Fig. 11.3. Neutral curves and growth rate curves when surface tension $\gamma \neq 0$. (a) Flow is stable for short and long waves. (b) Flow is stable for short waves but not long waves.
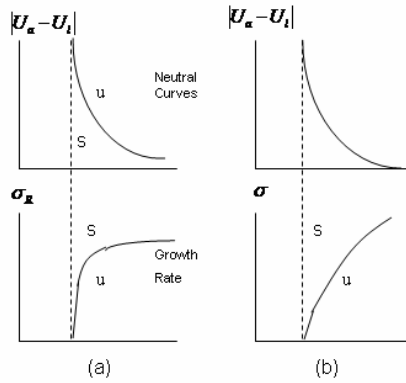
Fig. 11.4. Neutral curves and growth rate curves when $\gamma = 0$. (a) $\mu > 0$. The flow is unstable as $k \to 0$ but not Hadamard unstable. (b) $\mu = 0$, the flow is Hadamard unstable $\sigma_R \to \infty$ with k.

11.3.1 Formulation of the problem

A channel of rectangular cross-section with height H and width W and of length L is set horizontally, in which a gas layer is over a liquid layer (see figure 11.5): the two-layer Newtonian incompressible fluids are immiscible. The undisturbed interface is taken at $z = 0$ on the z-axis of Cartesian coordinates (x, y, z). We denote velocity by (u, w), pressure p, density ρ, viscosity μ and acceleration due to gravity $(0, -g)$; the y component is ignored herein.

In the undisturbed state, the gas (air) with a uniform flow $(U_a, 0)$ is in $0 < z < h_a$, and the liquid with a uniform flow $(U_l, 0)$ is in $-h_l < z < 0$ ($H = h_l + h_a$); the pressure has an equilibrium distribution due to the gravity. We consider Kelvin-Helmholtz instability of small disturbances to the undisturbed state.

The discontinuous prescription of data in the study of Kelvin-Helmholtz instability is a viscous potential flow solution of the Navier-Stokes in which no-slip conditions at the walls and no-slip and continuity of shear stress across the gas liquid interface are neglected. Usually the analysis of Kelvin-Helmholtz instability is done using potential flow for an inviscid fluid but this procedure leaves out certain effects of viscosity which can be included with complete rigor. An exact study of, say air over water requires the inclusion of all of the effects of viscosity, and even the prescription of a basic flow is much more complicated. Problems of superposed viscous fluids have been considered, for example, in the monograph on two-fluid mechanics by Joseph & Renardy (1991) and more recently in the paper and references therein of Charru & Hinch (2000).
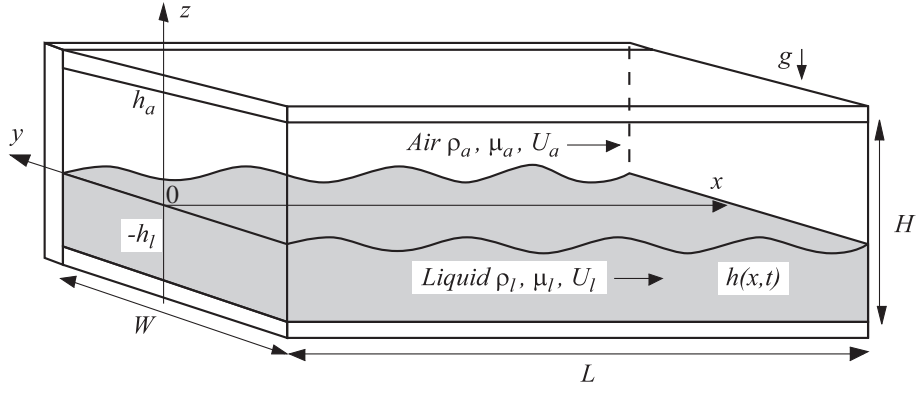
Fig. 11.5. Kelvin Helmholtz instability due to a discontinuity of velocity of air above liquid in a rectangular channel. The no-slip condition is not enforced in viscous potential flow so that the two dimensional solution satisfies the side-wall boundary conditions.

11.3.2 Viscous potential flow analysis

If the fluids are allowed to slip at the walls, then the two-dimensional solution will satisfy the three-dimensional equations and we may reduce the analysis to flow between parallel plates. We found by computing that three-dimensional disturbances are more stable than two-dimensional ones. We now consider two-dimensional disturbances, for which the velocity potential $\phi \equiv \phi(x, z, t)$ gives $(u, w) = \boldsymbol{\nabla}\phi$.

The potential is subject to the equation of continuity:

$$\frac{\partial u}{\partial x} + \frac{\partial w}{\partial z} = 0 \;\; \rightarrow \;\; \frac{\partial^2 \phi}{\partial x^2} + \frac{\partial^2 \phi}{\partial z^2} = 0; \tag{11.3.1}$$

thus the potentials for the respective fluids are given by

$$\frac{\partial^2 \phi_a}{\partial x^2} + \frac{\partial^2 \phi_a}{\partial z^2} = 0 \quad \text{in } 0 < z < h_a, \tag{11.3.2}$$

$$\frac{\partial^2 \phi_l}{\partial x^2} + \frac{\partial^2 \phi_l}{\partial z^2} = 0 \quad \text{in } -h_l < z < 0. \tag{11.3.3}$$

Boundary conditions at the interface (at $z = h$, where $h \equiv h(x, t)$ is the interface elevation) are given by

$$\frac{\partial h}{\partial t} + U_a \frac{\partial h}{\partial x} = w_a, \quad \frac{\partial h}{\partial t} + U_l \frac{\partial h}{\partial x} = w_l, \tag{11.3.4}$$

and the conditions on the walls are given by

$$w_a = 0 \quad \text{at } z = h_a, \tag{11.3.5}$$

$$w_l = 0 \quad \text{at } z = -h_l. \tag{11.3.6}$$

The potential ϕ_a that satisfies (11.3.2) and (11.3.5) for the air and the potential ϕ_l that satisfies (11.3.3) and (11.3.6) for the liquid are given, respectively, by

$$\phi_a = A_a \cosh\left[k\left(z - h_a\right)\right] \exp\left(\sigma t + \mathrm{i}kx\right) + \text{c.c.}, \tag{11.3.7a}$$

$$\phi_l = A_l \cosh\left[k\left(z + h_l\right)\right] \exp\left(\sigma t + \mathrm{i}kx\right) + \text{c.c.}, \tag{11.3.7b}$$

and the interface elevation may be given by

$$h = A_0 \exp\left(\sigma t + \mathrm{i}kx\right) + \text{c.c.}, \tag{11.3.7c}$$

where A_a, A_l and A_0 denote the complex amplitude, and c.c. stands for the complex conjugate of the preceding expression; σ is the complex growth rate and $k > 0$ denotes the wavenumber; $\mathrm{i} = \sqrt{-1}$. From the kinematic conditions (11.3.4), we have the following equations for the complex amplitudes:

$$\left(\sigma + \mathrm{i}kU_a\right) A_0 = -kA_a \sinh\left(kh_a\right), \tag{11.3.8a}$$

$$\left(\sigma + \mathrm{i}kU_l\right) A_0 = kA_l \sinh\left(kh_l\right). \tag{11.3.8b}$$

81

The other boundary condition is the normal stress balance (with the normal viscous stress) at the interface:

$$-p_a + 2\mu_a \frac{\partial w_a}{\partial z} + \rho_a gh - \left(-p_l + 2\mu_l \frac{\partial w_l}{\partial z} + \rho_l gh\right) = -\gamma \frac{\partial^2 h}{\partial x^2}, \tag{11.3.9}$$

in which γ denotes the surface tension. Noting that the pressure is solely subject to the Laplace equation derived from the equation of motion for small disturbances, the pressure terms in (11.3.9) may be eliminated using the equations of motion in which the viscous terms vanish identically when $\boldsymbol{u} = \boldsymbol{\nabla}\phi$; $\mu\nabla^2\boldsymbol{u} = \mu\boldsymbol{\nabla}\left(\nabla^2\phi\right) \equiv 0$. Thus p_a may be written, from the equation of motion where the viscous term vanishes, as

$$\rho_a \left(\frac{\partial u_a}{\partial t} + U_a \frac{\partial u_a}{\partial x}\right) = -\frac{\partial p_a}{\partial x}, \tag{11.3.10a}$$

and with the aid of the equation of continuity, we have the expression of p_a

$$\rho_a \left(\frac{\partial^2 w_a}{\partial t \partial z} + U_a \frac{\partial^2 w_a}{\partial x \partial z}\right) = \frac{\partial^2 p_a}{\partial x^2}; \tag{11.3.10b}$$

the pressure p_l may be written as

$$\rho_l \left(\frac{\partial^2 w_l}{\partial t \partial z} + U_l \frac{\partial^2 w_l}{\partial x \partial z}\right) = \frac{\partial^2 p_l}{\partial x^2}. \tag{11.3.11}$$

Thus the normal stress balance is now written as

$$-\rho_a \left(\frac{\partial^2 w_a}{\partial t \partial z} + U_a \frac{\partial^2 w_a}{\partial x \partial z}\right) + 2\mu_a \frac{\partial^3 w_a}{\partial x^2 \partial z} + \rho_l \left(\frac{\partial^2 w_l}{\partial t \partial z} + U_l \frac{\partial^2 w_l}{\partial x \partial z}\right) - 2\mu_l \frac{\partial^3 w_l}{\partial x^2 \partial z}$$
$$- (\rho_l - \rho_a) g \frac{\partial^2 h}{\partial x^2} = -\gamma \frac{\partial^4 h}{\partial x^4}, \tag{11.3.12}$$

hence we have the equation of σ, using (11.3.7a)–(11.3.8b):

$$\left[\rho_a (\sigma + ikU_a)^2 + 2\mu_a k^2 (\sigma + ikU_a)\right] \coth(kh_a) + \left[\rho_l (\sigma + ikU_l)^2 + 2\mu_l k^2 (\sigma + ikU_l)\right] \coth(kh_l)$$
$$+ (\rho_l - \rho_a) gk + \gamma k^3 = 0. \tag{11.3.13}$$

11.3.2.1 Dispersion relation

From (11.3.13) the dispersion relation is given as

$$A\sigma^2 + 2B\sigma + C = 0, \tag{11.3.14}$$

where the coefficients A, B and C are defined as

$$A = \rho_l \coth(kh_l) + \rho_a \coth(kh_a), \tag{11.3.15a}$$

$$B = ik \left[\rho_l U_l \coth(kh_l) + \rho_a U_a \coth(kh_a)\right] + k^2 \left[\mu_l \coth(kh_l) + \mu_a \coth(kh_a)\right] = B_R + iB_I, \tag{11.3.15b}$$

$$C = (\rho_l - \rho_a) gk - k^2 \left[\rho_l U_l^2 \coth(kh_l) + \rho_a U_a^2 \coth(kh_a)\right] + \gamma k^3$$
$$+ 2ik^3 \left[\mu_l U_l \coth(kh_l) + \mu_a U_a \coth(kh_a)\right] = C_R + iC_I. \tag{11.3.15c}$$

The solution σ may be expressed as

$$\sigma = -\frac{B}{A} \pm \sqrt{\frac{B^2}{A^2} - \frac{C}{A}} \quad \rightarrow \quad \sigma_R + i\sigma_I = -\frac{B_R + iB_I}{A} \pm \frac{\sqrt{D}}{A}, \tag{11.3.16}$$

where D is given by

$$D = D_R + iD_I = (B_R + iB_I)^2 - A(C_R + iC_I), \tag{11.3.17a}$$

$$D_R = \rho_l \rho_a (U_a - U_l)^2 k^2 \coth(kh_l) \coth(kh_a) + k^4 \left[\mu_l \coth(kh_l) + \mu_a \coth(kh_a)\right]^2$$
$$- \left[\rho_l \coth(kh_l) + \rho_a \coth(kh_a)\right] \left[(\rho_l - \rho_a) gk + \gamma k^3\right], \tag{11.3.17b}$$

$$D_I = 2k^3 (\rho_a \mu_l - \rho_l \mu_a) (U_a - U_l) \coth(kh_l) \coth(kh_a). \tag{11.3.17c}$$

When $\rho_a \mu_l = \rho_l \mu_a$ for which $D_I = 0$, and if $D_R \geq 0$, we have

$$\sigma_R = \frac{-B_R \pm \sqrt{D_R}}{A}, \tag{11.3.18a}$$

$$\sigma_I = -\frac{B_I}{A}. \tag{11.3.18b}$$

82

This is a typical case where the real and imaginary parts of σ can be expressed most clearly.

If the top and bottom are far away $h_l \to \infty$, $h_a \to \infty$, then (11.3.14) gives rise to

$$
\begin{aligned}
\sigma = \ & -\frac{\mathrm{i}k\left(\rho_a U_a + \rho_l U_l\right) + k^2\left(\mu_a + \mu_l\right)}{\left(\rho_a + \rho_l\right)} \\
& \pm \left[\frac{\rho_a\rho_l k^2\left(U_a - U_l\right)^2}{\left(\rho_a + \rho_l\right)^2} - \frac{\left(\rho_l - \rho_a\right)gk + \gamma k^3}{\left(\rho_a + \rho_l\right)} + \frac{k^4\left(\mu_a + \mu_l\right)^2}{\left(\rho_a + \rho_l\right)^2} + 2\mathrm{i}k^3\frac{\left(\rho_a\mu_l - \rho_l\mu_a\right)\left(U_a - U_l\right)}{\left(\rho_a + \rho_l\right)^2}\right]^{1/2},
\end{aligned}
$$

which is reduced, for a particular case that $\rho_a\mu_l = \rho_l\mu_a$, to

$$
\sigma_R = -\frac{k^2\left(\mu_a + \mu_l\right)}{\left(\rho_a + \rho_l\right)} \pm \left[\frac{\rho_a\rho_l k^2\left(U_a - U_l\right)^2}{\left(\rho_a + \rho_l\right)^2} - \frac{\left(\rho_l - \rho_a\right)gk + \gamma k^3}{\left(\rho_a + \rho_l\right)} + \frac{k^4\left(\mu_a + \mu_l\right)^2}{\left(\rho_a + \rho_l\right)^2}\right]^{1/2}, \tag{11.3.19a}
$$

$$
\sigma_I = -\frac{k\left(\rho_a U_a + \rho_l U_l\right)}{\left(\rho_a + \rho_l\right)}. \tag{11.3.19b}
$$

Here, it is easy to find that $\sigma_R = 0$ gives a relation independent of viscosity. In other words, the relation holds even for inviscid fluids; this is helpful for the problem to be considered herein.

11.3.2.2 Growth rates and wave speeds

In terms of $\sigma = \sigma_R + \mathrm{i}\sigma_I$, (11.3.14) is also written, for the real and imaginary parts, as

$$
A\left(\sigma_R^2 - \sigma_I^2\right) + 2\left(B_R\sigma_R - B_I\sigma_I\right) + C_R = 0, \quad \sigma_I = -\frac{2B_I\sigma_R + C_I}{2\left(A\sigma_R + B_R\right)}. \tag{11.3.20}
$$

Eliminating σ_I from the above, we have a quartic equation for σ_R:

$$
a_4\sigma_R^4 + a_3\sigma_R^3 + a_2\sigma_R^2 + a_1\sigma_R + a_0 = 0, \tag{11.3.21}
$$

where the coefficients are given as

$$
a_4 = A^3, \quad a_3 = 4A^2 B_R, \quad a_2 = 5AB_R^2 + AB_I^2 + A^2 C_R, \tag{11.3.22a}
$$

$$
a_1 = 2B_R^3 + 2B_R B_I^2 + 2AB_R C_R, \quad a_0 = -\frac{1}{4}AC_I^2 + B_R B_I C_I + B_R^2 C_R. \tag{11.3.22b}
$$

The quartic equation (11.3.21) can be solved analytically. Neutral states for which $\sigma_R = 0$ are described in terms of the solution to the equation $a_0 = 0$. The peak value (the maximum growth rate) σ_m and the corresponding wavenumber k_m are obtained by solving (11.3.21). It is usually true, but unproven, that $\lambda_m = 2\pi/k_m$ will be the length of unstable waves observed in experiments.

The complex values of σ are frequently expressed in terms of a complex frequency ω with

$$
\sigma_R + \mathrm{i}\sigma_I = \sigma = -\mathrm{i}\omega = -\mathrm{i}\omega_R + \omega_I. \tag{11.3.23}
$$

Hence

$$
\sigma_R = \omega_I; \quad \sigma_I = -\omega_R. \tag{11.3.24}
$$

The wave speed for the mode with wavenumber k is

$$
\tilde{C}_R = \omega_R/k = -\sigma_I/k. \tag{11.3.25}
$$

The set of wavenumbers for which flows are stable is also of interest. The wavelengths corresponding to these wavenumbers will not appear in the spectrum. Cut-off wavenumbers k_C separate the unstable and stable parts of the spectrum.

11.3.2.3 Neutral curves

Neutral curves define values of the parameters for which $\sigma_R(k) = 0$. These curves may be obtained by putting $a_0 = 0$:

$$
-\frac{\rho_l\mu_a^2\coth\left(kh_l\right)\coth^2\left(kh_a\right) + \rho_a\mu_l^2\coth^2\left(kh_l\right)\coth\left(kh_a\right)}{\left[\mu_l\coth\left(kh_l\right) + \mu_a\coth\left(kh_a\right)\right]^2}kV^2 + \left(\rho_l - \rho_a\right)g + \gamma k^2 = 0, \tag{11.3.26}
$$

where the relative velocity V is defined by $V \equiv U_a - U_l$. This equation may be solved for V^2 where

$$V^2(k) = \frac{[\mu_l \coth(kh_l) + \mu_a \coth(kh_a)]^2}{\rho_l \mu_a^2 \coth(kh_l) \coth^2(kh_a) + \rho_a \mu_l^2 \coth^2(kh_l) \coth(kh_a)} \frac{1}{k} \left[(\rho_l - \rho_a) g + \gamma k^2 \right]. \tag{11.3.27}$$

The lowest point on the neutral curve $V^2(k)$ is

$$V_c^2 = \min_{k \geq 0} V^2(k) \equiv V^2(k_c), \tag{11.3.28}$$

where $\lambda_c = 2\pi/k_c$ is the wavelength that makes V^2 minimum. The flow is unstable when

$$V^2 = (-V)^2 > V_c^2. \tag{11.3.29}$$

This criterion is symmetric with respect to V and $-V$, depending only on the absolute value of the difference. This feature stems from Galilean invariance; the flow seen by an observer moving with the gas is the same as the one seen by an observer moving with the liquid.

By recalling the results obtained by computing, it is interesting to note here that the three dimensional disturbances in the sense of the viscous potential flow lead to the relative velocity V_{3D}, which can be expressed in terms of (11.3.27) as

$$V_{3D}^2 \equiv \frac{(\boldsymbol{k} \cdot \boldsymbol{U}_a - \boldsymbol{k} \cdot \boldsymbol{U}_l)^2}{k_x^2} = \frac{k^2}{k_x^2} V^2(k), \tag{11.3.30}$$

only if we regard the 3D-wavenumber vector $\boldsymbol{k} = (k_x, k_y)$ as

$$k = \sqrt{k_x^2 + k_y^2}, \qquad k_y = 0, \pm\frac{\pi}{W}, \pm\frac{2\pi}{W}, \cdots. \tag{11.3.31}$$

It is evident in (11.3.30) that V_{3D}^2 is larger than $V^2(k)$ if $k_y \neq 0$; the most dangerous three-dimensional disturbance is two-dimensional with $k_y = 0$.

11.3.3 K-H Instability of inviscid fluid

For inviscid fluids ($\mu_a = \mu_l = 0$), we have $B_R = 0$ and $C_I = 0$; thus $a_3 = a_1 = a_0 = 0$ and (11.3.21) reduces to

$$a_4 \sigma_R^4 + a_2 \sigma_R^2 = 0, \tag{11.3.32}$$

thus we have

$$a_4 \sigma_R^2 + a_2 = 0, \tag{11.3.33}$$

and

$$\sigma_I = -\frac{B_I}{A} = -\frac{k \left[\rho_l U_l \coth(kh_l) + \rho_a U_a \coth(kh_a) \right]}{\rho_l \coth(kh_l) + \rho_a \coth(kh_a)}. \tag{11.3.34}$$

It should be noted here that the neutral curve was given by the equation $a_0 = 0$ in the viscous potential analysis ((11.3.26) and (11.3.27)), whereas the neutral curve in this K-H instability is given by the equation $a_2 = 0$. It is also noted that σ_I is the same as (11.3.18b), though σ_R may be different, in general, from (11.3.18a). But the equation $\sigma_R = 0$ in (11.3.33) is the same that $\sigma_R = 0$ in (11.3.18a); for the case of $\rho_a \mu_l = \rho_l \mu_a$.

From (11.3.33) with $a_2 < 0$, the growth rate σ_R is expressed as

$$\sigma_R = \pm \frac{\sqrt{\rho_l \rho_a k^2 \coth(kh_l) \coth(kh_a) V^2 - [\rho_l \coth(kh_l) + \rho_a \coth(kh_a)] \left[(\rho_l - \rho_a) gk + \gamma k^3 \right]}}{\rho_l \coth(kh_l) + \rho_a \coth(kh_a)}. \tag{11.3.35}$$

At the neutral state $\sigma_R = 0$ for which $a_2 = 0$, we have

$$\frac{\rho_l \rho_a k \coth(kh_l) \coth(kh_a)}{\rho_l \coth(kh_l) + \rho_a \coth(kh_a)} V^2 - \left[(\rho_l - \rho_a) g + \gamma k^2 \right] = 0. \tag{11.3.36}$$

Instability arises if

$$V^2 > \left[\frac{\tanh(kh_l)}{\rho_l} + \frac{\tanh(kh_a)}{\rho_a} \right] \frac{1}{k} \left[(\rho_l - \rho_a) g + \gamma k^2 \right] \equiv V_i^2(k). \tag{11.3.37}$$

In the stable case for which $a_2 > 0$, the wave velocity $\tilde{C}_R$ is given by

$$- k\tilde{C}_R = \sigma_I = -\frac{B_I}{A} \pm \sqrt{\frac{B_I^2}{A^2} + \frac{C_R}{A}}. \tag{11.3.38}$$

11.3.4 Dimensionless form of the dispersion equation

The dimensionless variables are designated with a hat and are

$$
\begin{aligned}
\hat{k} &= kH, \\
\hat{h}_a &= \frac{h_a}{H} \equiv \alpha, \\
\hat{h}_l &= \frac{h_l}{H} = 1 - \hat{h}_a, \\
\hat{\rho} &= \frac{\rho_a}{\rho_l}, \\
\hat{\mu} &= \frac{\mu_a}{\mu_l}, \\
\hat{\gamma} &= \frac{\gamma}{\rho_l g H^2},
\end{aligned}
\qquad
\begin{aligned}
\hat{U}_a &= \frac{U_a}{Q}, \\
\hat{U}_l &= \frac{U_l}{Q}, \\
\hat{V} &= \hat{U}_a - \hat{U}_l \\
\hat{\sigma} &= \frac{\sigma H}{Q}, \\
\theta &= \frac{\mu_l}{\rho_l H Q},
\end{aligned}
$$

where

$$Q = \left[\frac{(1-\hat{\rho})gH}{\hat{\rho}}\right]^{1/2}.$$

The dimensionless form of (11.3.14) is given by

$$
\begin{aligned}
\Big[\coth(\hat{k}\hat{h}_l) \;&+\; \hat{\rho}\coth(\hat{k}\hat{h}_a)\Big]\hat{\sigma}^2 \\
&+\; 2\hat{\sigma}\left\{i\hat{k}\left[\hat{U}_l\coth(\hat{k}\hat{h}_l) + \hat{\rho}\hat{U}_a\coth(\hat{k}\hat{h}_a)\right] + \theta\hat{k}^2\left[\coth(\hat{k}\hat{h}_l) + \hat{\mu}\coth(\hat{k}\hat{h}_a)\right]\right\} \\
&-\; \hat{k}^2\left[\hat{U}_l^2\coth(\hat{k}\hat{h}_l) + \hat{\rho}\hat{U}_a^2\coth(\hat{k}\hat{h}_a)\right] + 2i\hat{k}^3\theta\left[\hat{U}_l\coth(\hat{k}\hat{h}_l) + \hat{\mu}\hat{U}_a\coth(\hat{k}\hat{h}_a)\right] \\
&+\; \hat{k}\left[1 + \frac{\hat{\gamma}\hat{k}^2}{(1-\hat{\rho})}\right] = 0. \tag{11.3.39}
\end{aligned}
$$

The expression (11.3.27) for the neutral curve $\hat{\sigma}_R(\hat{k}) = 0$ is written in dimensionless variables as

$$\hat{V}^2 = \frac{\left[\tanh(\hat{k}\hat{h}_a) + \hat{\mu}\tanh(\hat{k}\hat{h}_l)\right]^2}{\tanh(\hat{k}\hat{h}_a) + (\hat{\mu}^2/\hat{\rho})\tanh(\hat{k}\hat{h}_l)} \frac{1}{\hat{k}}\left[1 + \frac{\hat{\gamma}\hat{k}^2}{(1-\hat{\rho})}\right]. \tag{11.3.40}$$

Notice that the growth rate parameter $\theta = \mu_l/(\rho_l H Q)$, which depends linearly on the kinematic viscosity $\nu_l = \mu_l/\rho_l$ of the liquid, does not appear in (11.3.40). Note also that the value of $(1 - \hat{\rho})$ is close to unity, since $\hat{\rho} = 0.0012$ for air-water.

The neutral curves for an inviscid fluid (11.3.36) can be obtained by putting $\hat{\mu} = \hat{\rho}$ or $\mu_l/\rho_l = \mu_a/\rho_a$. This gives from (11.3.40) the following expression;

$$\hat{V}^2 = \left[\tanh(\hat{k}\hat{h}_a) + \hat{\rho}\tanh(\hat{k}\hat{h}_l)\right]\frac{1}{\hat{k}}\left[1 + \frac{\hat{\gamma}\hat{k}^2}{1-\hat{\rho}}\right] \tag{11.3.41}$$

which is the dimensionless form of (11.3.37). Though this reduction is immediate it is surprising.

Evaluating (11.3.40) for $\hat{\mu} = 0$, we get

$$\hat{V}^2 = \tanh(\hat{k}\hat{h}_a)\frac{1}{\hat{k}}\left[1 + \frac{\hat{\gamma}\hat{k}^2}{1-\hat{\rho}}\right]. \tag{11.3.42}$$

Evaluating (11.3.40) for $\hat{\mu} = \infty$ we get

$$\hat{V}^2 = \hat{\rho}\tanh(\hat{k}h_l)\frac{1}{\hat{k}}\left[1 + \frac{\hat{\gamma}\hat{k}^2}{1-\hat{\rho}}\right]. \tag{11.3.43}$$

It is easy to verify that $\hat{V}^2$ is maximum at $\hat{\mu} = \hat{\rho}$, for inviscid fluids. Viscosity in viscous potential flow is destabilizing; however, large viscosities are less destabilizing than small viscosities.

Since $\hat{\rho} = 0.0012$, which is very small, the variation in the stability is large when $\hat{\mu}$ varies between $\hat{\rho}$ and ∞, and is very small when $\hat{\mu}$ varies between $\hat{\rho}$ and zero. The value $\hat{\mu} = 0.018 > \hat{\rho} = 0.0012$, and is in the interval in which $\hat{V}^2$ is rapidly varying (see figure 11.8).

In the literature on gas liquid flows a long-wave approximation is often made to obtain stability limits. For long waves $\hat{k} \to 0$ and $\tanh(\hat{k}\hat{h}) \to \hat{k}\hat{h}$ and (11.3.40) reduces to

$$\hat{V}^2 = \frac{(\hat{h}_a + \hat{\mu}\hat{h}_l)^2}{\hat{h}_a + (\hat{\mu}^2/\hat{\rho})\hat{h}_l} \left[1 + \frac{\hat{\gamma}\hat{k}^2}{1 - \hat{\rho}} \right]. \tag{11.3.44}$$

The effect of surface tension disappears in this limit but the effects of viscosity are important. To obtain the long wave limit in the inviscid case put $\hat{\mu} = \hat{\rho}$.

The regularization of short-waves by surface tension is an important physical effect. For short waves, $\hat{k} \to \infty$, $\tanh(\hat{k}\hat{h}) \to 1$ and

$$\hat{V}^2 = \frac{(\hat{\mu} + 1)^2}{1 + \hat{\mu}^2/\hat{\rho}} \frac{1}{\hat{k}} \left[1 + \frac{\hat{\gamma}\hat{k}^2}{(1 - \hat{\rho})} \right]. \tag{11.3.45}$$

To obtain the short wave limit in the inviscid case put $\hat{\mu} = \hat{\rho}$.

The effects of surface tension may be computed from (11.3.44) and (11.3.45). The stability limit for long waves $\hat{k} \to 0$ is independent of $\hat{\gamma}$. For short waves (11.3.44) has a minimum at $\hat{k} = \sqrt{(1 - \hat{\rho})/\hat{\gamma}}$ with a value there given by

$$\hat{V}^2 = \frac{2(\hat{\mu} + 1)^2}{1 + \hat{\mu}^2/\hat{\rho}} \sqrt{\frac{\hat{\gamma}}{1 - \hat{\rho}}}. \tag{11.3.46}$$

Equation (11.3.46) shows that short waves are stabilized by increasing $\hat{\gamma}$. For small $\hat{\gamma}$, long waves are unstable.

11.3.5 The effect of liquid viscosity and surface tension on growth rates and neutral curves

For air and water at 20°C

$$\rho_a = 0.0012\,\text{g/cm}^3, \quad \rho_l = 1\,\text{g/cm}^3, \quad \hat{\rho} = \rho_a/\rho_l = 0.0012, \tag{11.3.47}$$

$$\mu_a = 0.00018\,\text{poise}, \quad \mu_l = 0.01\,\text{poise}, \quad \hat{\mu} = \mu_a/\mu_l = 0.018. \tag{11.3.48}$$

The surface tension of air and pure water is $\gamma = 72.8$ dynes/cm. Usually the water is slightly contaminated and $\gamma = 60$ dynes/cm is more probable for the water-air tension in experiments. For all kinds of organic liquids a number like $\gamma = 30$ dynes/cm is a good approximation.

Neutral curves for $\hat{\mu} = 0.018$ (air/water) and $\hat{\mu} = \hat{\rho} = 0.0012$ (inviscid flow) and $\hat{\mu} = 3.6 \times 10^{-6}$ ($\mu_l = 50$ poise) with $\gamma = 60$ dynes/cm are selected here; the former two are shown in figures 11.6 and 11.7. The liquid viscosities $\mu_l = \rho_l \mu_a/\rho_a$ corresponding to these three cases are $\mu_l = 0.01$ poise, 0.15 poise and 50 poise. The neutral curves for $\hat{\mu} \geq \hat{\rho}$ are nearly identical. The neutral curves for $\hat{\mu} = 0.018$ (air/water) are to be compared with experiments. We have identified the minimum values of (11.3.40) over $\hat{k} \geq 0$ in the air/water case, and in tables 11.1, 11.2 and 11.3 the critical velocity $V_c = V(k_c)$, the critical wave number k_c (and wave length $\lambda_c = 2\pi/k_c$) and associated wave speeds $\tilde{C}_{Rc} = \tilde{C}_R(k_c)$ are listed. In the tables, V_s and $\tilde{C}_{Rs}$ denote the values taken at $k = 10^{-3}$ cm^{-1}, which may be representative of values in the limit of long waves, $k \to 0$. The variation of the critical velocity with the viscosity ratio $\hat{\mu} = \mu_a/\mu_l$ for a representative gas fraction $\alpha = 0.5$ is shown in figure 11.8. The vertical line $\hat{\mu} = \hat{\rho}$ identifies the stability limit for inviscid fluids. Points to the left of this line have high liquid viscosities $\mu_l > 0.15$ poise, and for points to the right, $\mu_l < 0.15$ poise.

In all cases the critical velocity is influenced by surface tension; the critical velocity is given by long waves only when α is small (small air gaps). For larger values of α (say $\alpha > 0.2$), the most dangerous neutrally unstable wave is identified by a sharp minimum determined by surface tension, which is identified in table 11.1 (c.f. equation (11.3.46)).
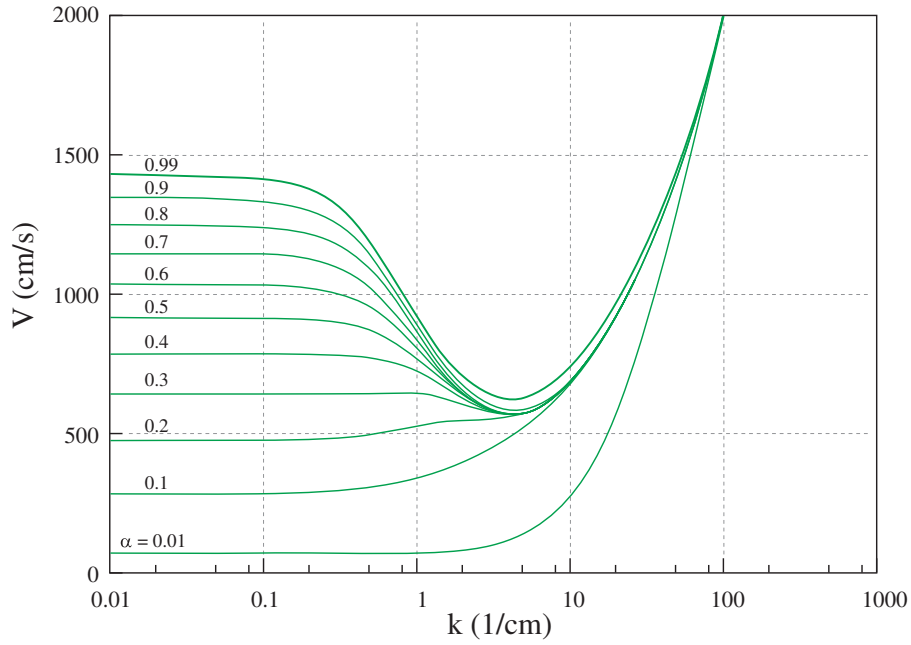
Fig. 11.6. Neutral curves for air and water ($\hat{\mu} = 0.018$, see table 11.1 and figure 11.8); $\alpha = \hat{h}_a$ is the gas fraction. As in the usual manner, the disturbances will grow above the neutral, but decay below it. For α larger than about 0.2, there arises the critical velocity V_c below which all the disturbances will decay.

Table 11.1. *Typical values of the neutral curves in figure 11.6 for air-water with $\rho_a = 0.0012$ g/cm^3, $\mu_a = 0.00018$ poise, $\rho_l = 1.0$ g/cm^3, $\mu_l = 0.01$ poise, $g = 980.0$ cm/sec^2, $\gamma = 60.0$ dynes/cm, $H = 2.54$ cm. (This table was based upon the results of computation that the neutral curves with $\alpha = 0.1$ and 0.2 in figure 11.6 increase monotonically from the values V_s cm/sec at $k = 10^{-3}$ cm^{-1}; the curve with $\alpha = 0.3$ in figure 11.6 increases from the value V_s cm/sec at $k = 10^{-3}$ cm^{-1}, takes a maximum $V = 651.3$ cm/sec at $k = 0.692$ cm^{-1}, and then takes a minimum $V_c = 572.5$ cm/sec (the critical) at $k_c = 3.893$ cm^{-1}; for the other values of α, the corresponding curves give the critical V_c at k_c.)*

$\hat{h}_a$	V_s cm/sec	$\tilde{C}_{Rs}$ cm/sec	k_c cm^{-1}	λ_c cm	V_c cm/sec	$\tilde{C}_{Rc}$ cm/sec
0.01	76.04	198.6	0.649	9.676	72.92	155.9
0.1	285.6	43.22				
0.2	478.5	20.82				
0.3	643.4	12.50	0.692	9.076	651.3	9.432
			3.893	1.614	572.5	5.510
0.4	788.8	8.150	4.020	1.563	573.9	5.484
0.5	919.4	5.481	4.052	1.551	574.1	5.481
0.6	1039	3.676	4.052	1.551	574.1	5.479
0.7	1149	2.373	4.052	1.551	574.3	5.459
0.8	1252	1.389	4.117	1.526	575.7	5.319
0.9	1348	0.619	4.354	1.443	585.3	4.415
0.99	1430	0.056	4.150	1.514	628.0	0.585
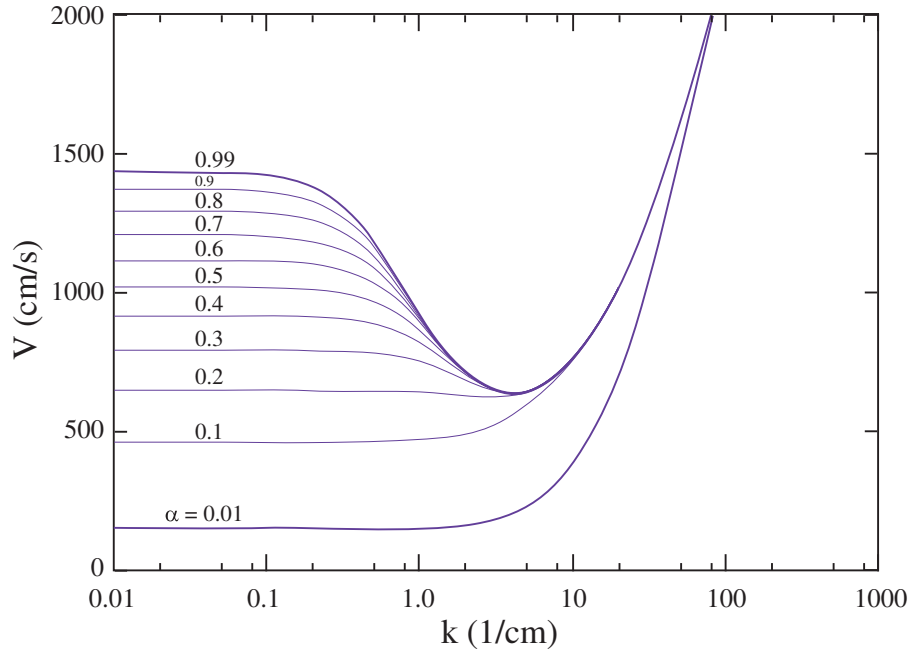
Fig. 11.7. Neutral curves for inviscid fluids ($\hat{\mu} = \hat{\rho} = 0.0012$) for different gas fractions $\alpha = \hat{h}_a$. This neutral curve arose for the special case $\hat{\mu} = \hat{\rho} = 0.0012 = \mu_a/\mu_l$ with $\mu_a = 0.00018$ poise; hence $\mu_l = 0.15$ poise. Surprisingly it is identical to the case $\mu_a = \mu_l = 0$ (see table 11.2 and figure 11.8). The neutral curves for viscous fluids with $\mu_l > 15$ cp are essentially the same as these (<u>c.f.</u> table 11.2 and 11.3).

Table 11.2. *Typical values of the neutral curves in figure 11.7 for air-water (as inviscid fluids) with*
$\rho_a = 0.0012$ *g/cm*^{3}, $\mu_a = 0.0$ *poise*, $\rho_l = 1.0$ *g/cm*^{3}, $\mu_l = 0.0$ *poise*, $g = 980.0$ *cm/sec*^{2}, $\gamma = 60.0$ *dynes/cm*,
H = 2.54 cm.

$\hat{h}_a$	V_s cm/sec	$\tilde{C}_{Rs}$ cm/sec	k_c cm^{-1}	λ_c cm	V_c cm/sec	$\tilde{C}_{Rc}$ cm/sec
0.01	152.2	16.17	0.629	9.990	150.6	9.725
0.1	457.6	4.890				
0.2	645.3	3.082	2.990	2.101	619.8	0.818
0.3	789.5	2.204	3.924	1.601	634.4	0.764
0.4	911.2	1.637	4.020	1.563	635.7	0.762
0.5	1018	1.221	4.052	1.551	635.9	0.762
0.6	1115	0.892	4.052	1.551	635.9	0.762
0.7	1205	0.619	4.052	1.551	635.9	0.759
0.8	1288	0.386	4.052	1.551	635.9	0.738
0.9	1366	0.182	4.052	1.551	635.8	0.590
0.99	1432	0.017	4.052	1.551	635.6	0.078
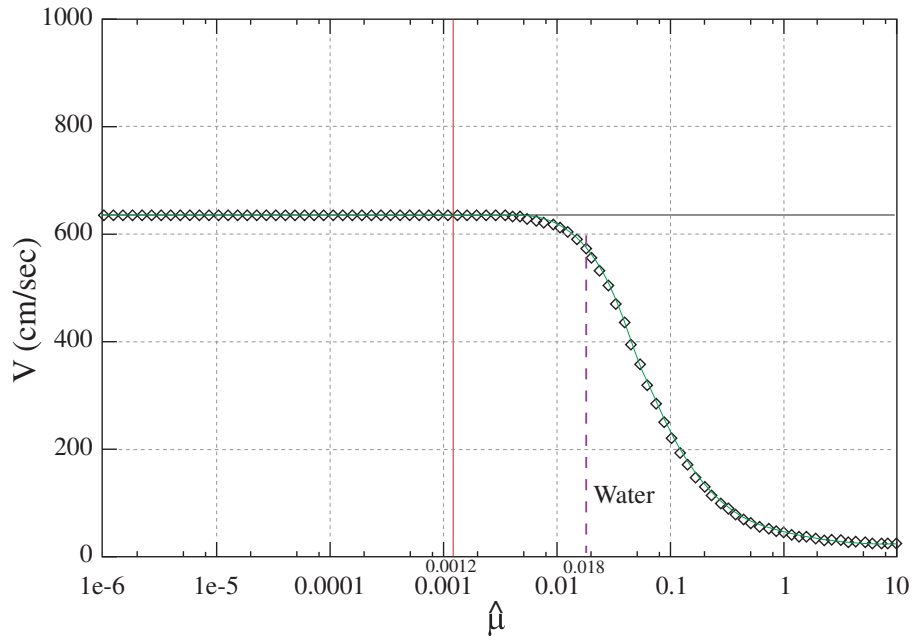
Fig. 11.8. Critical velocity V vs. $\hat{\mu}$ for $\alpha = 0.5$. The critical velocity is the minimum value on the neutral curve. The vertical line is $\hat{\mu} = \hat{\rho} = 0.0012$ and the horizontal line at $V = 635.9$ cm/sec is the critical value for inviscid fluids. The vertical dashed line at $\hat{\mu} = 0.018$ is for air and water. Typical values for a high viscosity liquid are given in table 11.3 below.

Table 11.3. *Typical values of the neutral curves for air-high viscosity liquid with $\rho_a = 0.0012$ g/cm^3, $\mu_a = 0.00018$ poise, $\rho_l = 1.0$ g/cm^3, $\mu_l = 50.0$ poise, $g = 980.0$ cm/sec^2, $\gamma = 60.0$ dynes/cm, $H = 2.54$ cm; thus $\hat{\mu} = 3.6 \times 10^{-6}$. This corresponds to a high viscosity case in figure 11.8. (The curves with $\hat{h}_a = 0.5$ through 0.8 take almost the same minimum value at $k = k_c$, though the values at $k = 10^{-3}$ cm^{-1} change as $V_s = 1018\text{-}1287$ cm/sec and $\tilde{C}_{Rs} = 0.0011\text{-}0.0003$ cm/sec.) (see table 11.4 for the maximum growth rate.)*

$\hat{h}_a$	V_s cm/sec	$\tilde{C}_{Rs}$ cm/sec	k_c cm^{-1}	λ_c cm	V_c cm/sec	$\tilde{C}_{Rc}$ cm/sec
0.01	144.0	0.1104				
0.1	455.2	0.0100				
0.2	643.7	0.0045	2.990	2.101	619.4	0.0012
0.3	788.4	0.0026	3.924	1.601	634.1	0.0011
0.4	910.4	0.0017	4.020	1.563	635.4	0.0011
0.5	1018	0.0011	4.052	1.551	635.5	0.0011
0.6	1115	0.0007	4.052	1.551	635.5	0.0011
0.7	1204	0.0005	4.052	1.551	635.5	0.0011
0.8	1287	0.0003	4.052	1.551	635.5	0.0011
0.9	1366	0.0001	4.052	1.551	635.5	0.0009
0.99	1432	1.1×10^{-5}	4.052	1.551	635.5	0.0001
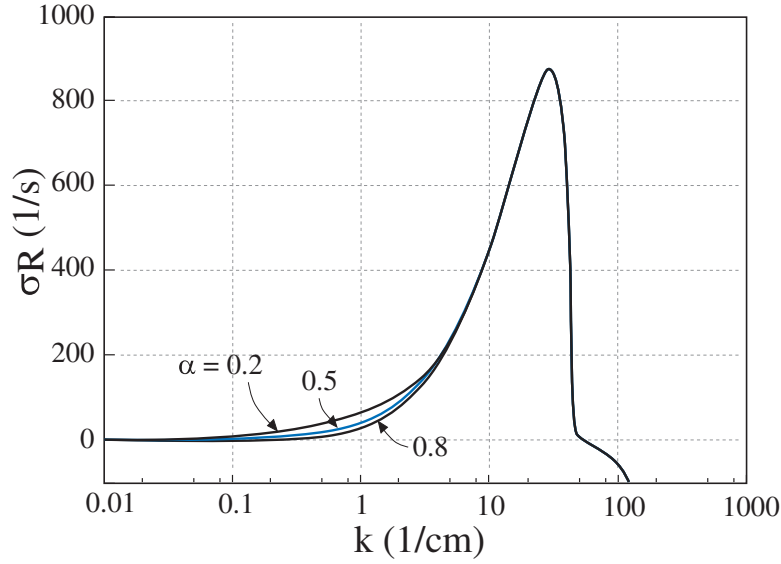
Fig. 11.9. The real part of growth rate σ_R sec^{-1} vs. k cm^{-1} for $\hat{\mu} = 0.018$ (water, $\mu_l = 1$ cp), $V = 1500$ cm/sec. The graphs are top to bottom $\alpha = 0.2,\ 0.5,\ 0.8$. The curves of σ_R sec^{-1} along the line of $V = 1500$ cm/sec in figure 11.6, are drawn here for respective values of α. Instability may arise for all the disturbances of wavenumbers below the cut-off wavenumber k_C. The maximum growth rate σ_{Rm} and the corresponding wavenumber $k_m = 2\pi/\lambda_m$ for $V = 1500$ and 900 cm/sec are listed with wave velocity $\tilde{C}_{Rm}$ in table 11.4 below.

The growth rates depend strongly on the liquid viscosity unlike the neutral curves. The most dangerous linear wave is the one whose growth rate σ_R is maximum at $k = k_m$,

$$\sigma_{Rm} = \sigma_R(k_m) \overset{\text{max}}{\underset{k \geq 0}{}} \sigma_R(k) \tag{11.3.49}$$

with an associated wavelength $\lambda_m = 2\pi/k_m$ and wave speed $\tilde{C}_{Rm} = \tilde{C}_R(k_m)$. Typical growth rate curves are shown in figure 11.9. Maximum growth rate parameters for $\hat{\mu} = 0.018$ (figure 11.9), $\hat{\mu} = \hat{\rho} = 0.0012, \mu_l = 15$ cp and $\hat{\mu} = 3.6 \times 10^{-6}(\mu_l = 50$ p) are listed for $V = 1500$ and 900 cm/sec in table 11.4.

90

Table 11.4. *Wave number, wave length and wave speed for the maximum growth rate (11.3.49).*

$\hat{\mu}$	V cm/sec	$\hat{h}_a$	k_m cm^{-1}	λ_m cm	σ_{Rm} sec^{-1}	$\tilde{C}_{Rm}$ cm/sec
0.018	1500	0.01	29.90	0.2101	1448	3.044
		0.1-0.9	29.66	0.2118	872.5	2.049
		0.99	32.13	0.1955	706.2	1.454
	900	0.01	15.40	0.408	615.3	3.046
		0.1	10.00	0.628	167.7	1.183
		0.2	10.24	0.613	164.2	1.175
		0.3-0.8	10.24	0.613	164.2	1.174
		0.9	10.33	0.609	163.3	1.164
		0.99	11.36	0.553	84.66	0.367
0.0012	1500	0.01	26.95	0.233	1340	3.022
		0.1-0.9	27.17	0.231	768	1.798
		0.99	30.14	0.209	584.7	1.159
	900	0.01	14.45	0.435	585.2	3.064
		0.1	9.456	0.665	155.1	1.097
		0.2-0.7	9.685	0.649	151.0	1.079
		0.8	9.763	0.644	151.0	1.079
		0.9	9.841	0.638	149.9	1.064
		0.99	10.66	0.589	69.59	0.285
3.6×10^{-6}	1500	0.01	1.821	3.450	295.1	24.55
		0.1	0.916	6.861	60.04	4.495
		0.2	0.845	7.432	34.43	2.049
		0.3	3.087	2.035	21.96	0.086
		0.4-0.6	4.4-4.5	1.42-1.40	21.89	0.045-0.04
		0.7	4.679	1.343	21.85	0.040
		0.8	5.360	1.172	21.61	0.032
		0.9	7.743	0.812	20.21	0.017
		0.99	20.54	0.306	6.801	0.003
	900	0.01	1.323	4.750	145.9	19.64
		0.1	0.676	9.297	24.80	3.017
		0.2	0.581	10.82	10.48	1.199
		0.3	0.984	6.385	4.294	0.135
		0.4-0.6	4.02-4.08	1.56-1.51	4.86	0.010
		0.7	4.150	1.514	4.840	0.009
		0.8	4.460	1.409	4.735	0.008
		0.9	5.534	1.135	4.100	0.005
		0.99	7.994	0.786	0.741	0.001

11.3.6 Comparison of theory and experiments in rectangular ducts

Kordyban & Ranov (1970) and Wallis & Dobson (1973) are the only authors to report the results of experiments in rectangular ducts. Many other experiments have been carried out in round pipes; the results of these experiments are not perfectly matched to the analysis done here or elsewhere, and will be discussed later.

All experimenters were motivated to understand the transition from stratified flow with a flat smooth interface to slug flow. They note that in many cases the first transition, which is studied here, is from smooth stratified flow to small-amplitude sinusoidal waves, called capillary waves by Wallis & Dobson (1973). The data given by these authors are framed as a transition to slug flow, though the criteria given are for the loss of stability of smooth stratified flow. The theoretical predictions are for the loss of stability, which may or may not be to slug flow.

Note also that all the linear theories that neglect viscosity overpredict the observed stability limit. Wallis & Dobson (1973) note that "...as a result of the present experiments it is our view that the various small wave theories are all inappropriate for describing 'slugging.' Slugging is the result of the rapid development of a large wave which rides over the underlying liquid and can eventually fill the channel to form a slug..." They also note that "It was found possible to produce slugs at air fluxes less than those predicted" by their empirical formula, $j^* < 0.5\alpha^{3/2}$. All this suggests that we may be looking at something akin to subcritical bifurcation with multiple solutions and hysteresis.

Turning next to linearized theory we note that Wallis & Dobson (1973) do an inviscid analysis stating that "...if waves are 'long' ($kh_L \ll 1$, $kh_G \ll 1$) and surface tension can be neglected, the predicted instability condition is

$$(v_G - v_L)^2 > (\rho_L - \rho_G) g \left(\frac{h_G}{\rho_G} + \frac{h_L}{\rho_L} \right). \tag{11.3.50}$$

If $\rho_G \ll \rho_L$ and $v_L \ll v_G$ they may be simplified further to give

$$\rho_G v_G^2 > g(\rho_L - \rho_G)h_G \tag{11.3.51}$$

which is the same as

$$j_G^* > \alpha^{3/2} \tag{11.3.52}$$

..." Here $\alpha = h_G/H$ and

$$j_G^* = \frac{v_G \alpha \sqrt{\rho_G}}{\sqrt{gH(\rho_L - \rho_G)}} > \alpha^{3/2}.$$

Their criterion (11.3.50) is identical to our (11.3.44) for the long wave inviscid case $\hat{\mu} = \hat{\rho}$ and $\hat{k} \to 0$. They compare their criterion (11.3.52) with transition observations that they call 'slugging' and note that empirically the stability limit is well described by

$$j_G^* > 0.5\alpha^{3/2},$$

rather than (11.3.52).

In figures 11.10 we plot j^* vs. α giving $j_G^* = \alpha^{3/2}$ and $0.5\alpha^{3/2}$; we give the results from our viscous potential flow theory for the inviscid case in table 11.2 and the air water case in table 11.1 and we show the experimental results presented by Wallis & Dobson (1973) and Kordyban & Ranov (1970). Our theory fits the data better than Wallis & Dobson (1973) $j^* = \alpha^{3/2}$; it still overpredicts the data for small α but fits the large α data quite well; we have good agreement when the water layer is small.

The predicted wave length and wave speed in table 11.1 can be compared with experiments in principle, but in practice this comparison is obscured by the focus on the formation of slugs. For example, Wallis & Dobson (1973) remarks that "at a certain minimum air velocity, ripples appeared at the air entry end, and slowly spread down the channel. These waves were about 2-in. (0.05 m) long and were made up of long wave crests, with three or four capillary waves riding on the troughs. The long waves traveled faster than the capillary waves." The speed of these long waves were reported by Wallis & Dobson (1973) to be less than 0.3 m/sec in all cases. Theoretical results from table 11.1 show that the wave length λ_c increases with the water depth (as in the experiment) and the wave speed varies from 0.1 m/sec to 0.04 m/sec. The predicted spacing of the waves on average is about 1.5 cm/sec. The predicted wave length and wave speed from viscous potential flow are apparently in good agreement with the waves Wallis & Dobson (1973) call capillary waves.
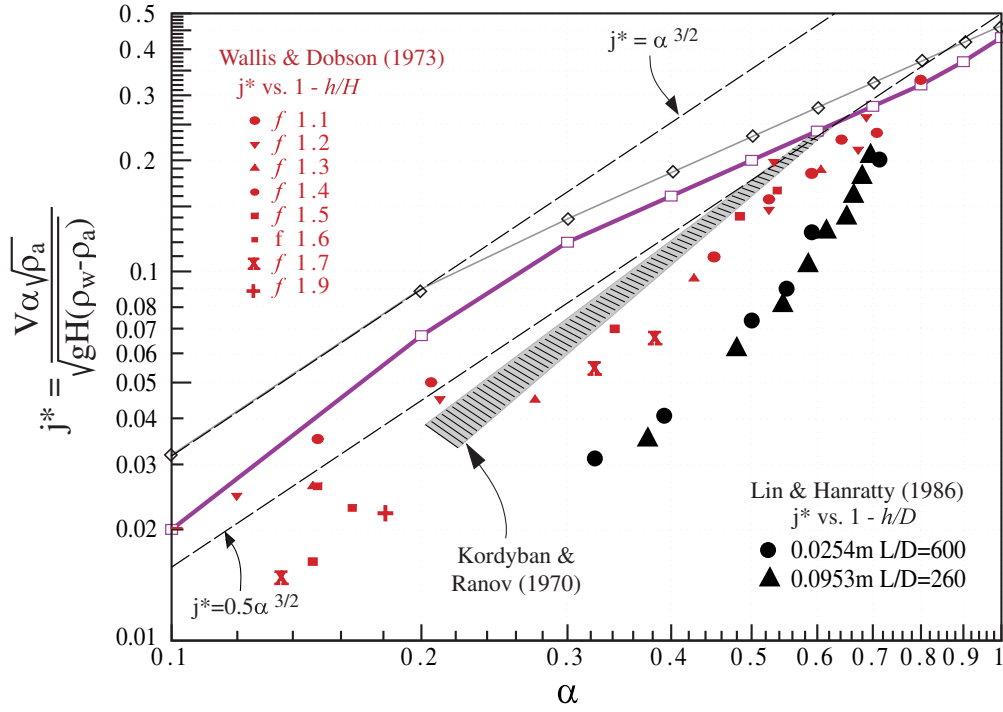
Fig. 11.10. j^* vs. α is for marginal stability of air and water in a frame in which the water velocity is zero. The heavy line through $\square$ = air-water, our result with $\gamma = 60$ dynes/cm from table 11.1; $\diamond$ = inviscid fluid from table 11.2. $j^* = \alpha^{3/2}$ is the long wave criterion for an inviscid fluid put forward by Wallis & Dobson (1973). $j^* = 0.5\alpha^{3/2}$ was proposed by them as best fit to the experiments $f1.1$ through $f1.9$ described in their paper. The shaded region is from experiments by Kordyban & Ranov (1970). Also shown are experimental data in rectangular conduits $j * vs. 1 - h/H = \alpha$ and in round pipes $j * vs. 1 - h/D = \alpha$ (Lin & Hanratty 1986, figure 4).

Observations similar to those of Wallis & Dobson (1973) just cited were made by Andritsos, Williams & Hanratty (1989) who note that for high viscosity liquid (80 cp) a region of regular 2D waves barely exists. "The first disturbances observed with increasing gas velocity are small-amplitude, small-wavelength, rather regular 2D waves. With a slight increase in gas velocity, these give way to a few large-amplitude waves with steep fronts and smooth troughs, and with spacing that can vary from a few centimeters to a meter."

11.3.7 Critical viscosity and density ratios

The most interesting aspect of our potential flow analysis is the surprising importance of the viscosity ratio $\hat{\mu} = \mu_a/\mu_l$ and density ratio $\hat{\rho} = \rho_a/\rho_l$; when $\hat{\mu} = \hat{\rho}$ the equation (11.3.40) for marginal stability is identical to the equation for the neutral stability of an inviscid fluid even though $\hat{\mu} = \hat{\rho}$ in no way implies that the fluids are inviscid. Moreover, the critical velocity is a maximum at $\hat{\mu} = \hat{\rho}$; hence the critical velocity is smaller for all viscous fluids such that $\hat{\mu} \neq \hat{\rho}$ and is smaller than the critical velocity for inviscid fluids. All this may be understood by inspection of figure 11.8, which shows that $\hat{\mu} = \hat{\rho}$ is a distinguished value that can be said to divide high viscosity liquids with $\hat{\mu} < \hat{\rho}$ from low viscosity liquids. The stability limit of high viscosity liquids can hardly be distinguished from each other while the critical velocity decreases sharply for low viscosity fluids. This result may be framed in terms of the kinematic viscosity $\nu = \mu/\rho$ with high viscosities $\nu_l > \nu_a$. The condition $\nu_a = \nu_l$ can be written as

$$\mu_l = \mu_a \frac{\rho_l}{\rho_a}. \tag{11.3.53}$$

For air and water

$$\mu_l = 0.15 \text{ poise.} \tag{11.3.54}$$

Hence $\mu_l > 0.15$ poise is a high viscosity liquid and $\mu_l < 0.15$ poise is a low viscosity liquid provided that $\rho_l \approx 1$ g/cm^3.
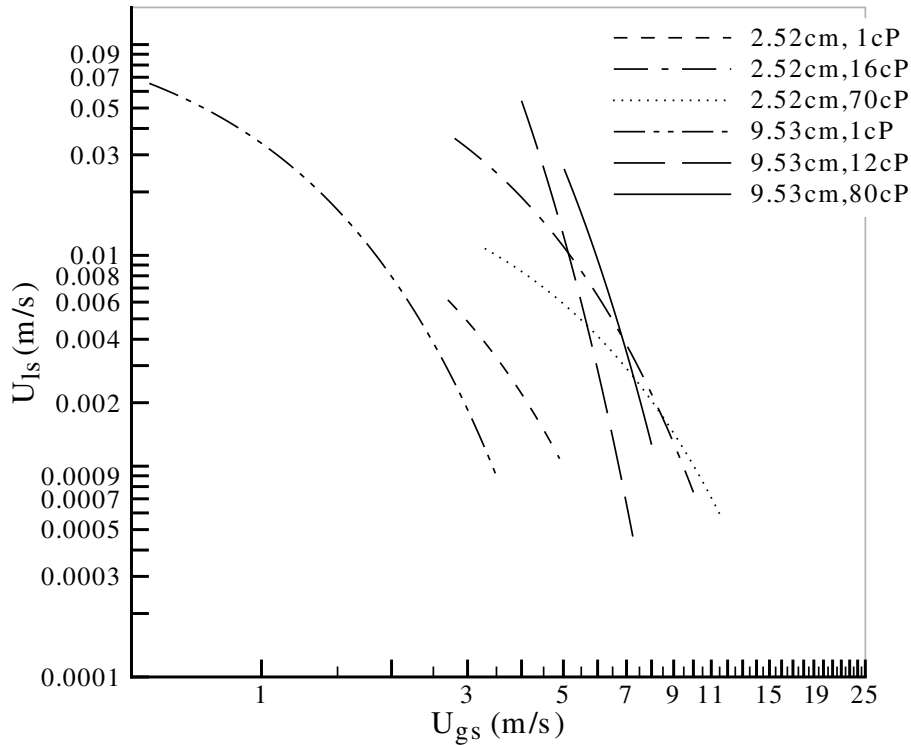
Fig. 11.11. (After Andritsos & Hanratty 1987.) The borders between smooth stratified flow and disturbed flow are observed in experiment. The water-air data is well below the cluster of high viscosity data that is bunched together.

Other authors have noted unusual relations between viscous and inviscid fluids. Barnea & Taitel (1993) note that "the neutral stability lines obtained from the viscous Kelvin-Helmholtz analysis and the inviscid analysis are quite different for the case of low liquid viscosities, whereas they are quite similar for high viscosity, contrary to what one would expect." Their analysis starts from a two-fluid model and it leads to different dispersion relations; they do not obtain the critical condition $\hat{\mu} = \hat{\rho}$. Earlier, Andritsos <u>et al</u> (1989) noted a "surprising result that the inviscid theory becomes more accurate as the liquid viscosity increases."

Andritsos & Hanratty (1987) have presented flow regime maps for flows in 2.52 cm and 9.53 cm pipe for fluids of different viscosity ranging from 1 cp to 80 cp. These figures present flow boundaries; the boundaries of interest to us are those that separate 'smooth' flow from disturbed flow. Liquid holdups (essentially α) are not specified in these experiments. We extracted the smooth flow boundaries from figures in Andritsos & Hanratty (1987) and collected them in our figure 11.11. It appears from this figure that the boundaries of smooth flow for all the liquids with $\mu_l > 15$ cp are close together, but the boundary for water with $\mu_l = 1$ cp is much lower. The velocities shown in these figures are superficial velocities; the average velocities which could be compared with critical velocities in tables 11.1, 11.2 and 11.3 are larger than the superficial velocities and are significantly larger than those in the tables.

Even earlier Francis (1951) had observed that even though the inviscid prediction of the KH instability overestimates the onset for air over water, this prediction is in good agreement with experiments in rectangular ducts when air is above water.

11.3.8 Further comparisons with previous results

In practice interest in the pipelining of gas-liquid flow is in round pipes. All experiments other than those of Kordyban & Ranov (1970) and Wallis & Dobson (1973) reviewed in section 11.3.6 have been carried out in round pipes. To our knowledge there is no other theoretical study in which the stability of stratified flow in a round pipe is studied without approximations. Theoretical studies of stability of stratified flow have been presented by Wallis (1969); Wu *et al.* (1987), Barnea (1991), Crowley, Wallis & Barry (1992), Kordyban & Ranov (1970), Wallis & Dobson (1973), Taitel & Dukler (1976), Mishima & Ishii (1980), Lin & Hanratty (1986), Andritsos & Hanratty (1987), Andritsos *et al.* (1989), Barnea & Taitel (1993). Viscosity is neglected by Kordyban & Ranov

94

(1970), Wallis & Dobson (1973), Taitel & Dukler (1976) and Mishima & Ishii (1980). Surface tension is neglected by Wallis (1969), Kordyban & Ranov (1970), Wallis & Dobson (1973), Taitel & Dukler (1976), Mishima & Ishii (1980) and Lin & Hanratty (1986). Wallis (1969), Lin & Hanratty (1986), Wu *et al.* (1987), Barnea (1991), Crowley *et al.* (1992) and Barnea & Taitel (1993) use one or other of the forms of two-fluids equations. In these equations averaged variables are introduced, the actual geometry is represented only so far as its area and round, elliptical or rectangular pipes with equal areas are equivalent. The effects of viscosity in these averaged models are introduced through empirical wall and interfacial fraction correlations. All these authors neglect the normal component of viscous stress (extensional stresses are neglected). The approach of Andritsos & Hanratty (1987), Andritsos *et al.* (1989) is different; all the main physical effects are represented in analysis of the plane flow which is later applied to flow in round pipes. The disturbance equations for the liquid are solved exactly except that the shear of basic liquid flow is neglected using a plug flow assumption. The effects of the gas on the liquid are represented through empirical correlations and further approximations are required for round pipes.

The viscous analysis of Andritsos & Hanratty (1987) for stability of stratified flow indicates that the critical velocity increases with increasing viscosity unlike the present analysis which predicts no such increase when $\nu_l > \nu_a$. The discrepancy may be due to the approximations made by Andritsos & Hanratty (1987).

Experiments on the stability of stratified flow have been reported by Kordyban & Ranov (1970), Wallis & Dobson (1973), Taitel & Dukler (1976), Lin & Hanratty (1986), Crowley *et al.* (1992) and Andritsos & Hanratty (1987). The experiments of Lin & Hanratty (1986) and Andritsos & Hanratty (1987) do not have data giving the height of the liquid and gas layers. Kordyban & Ranov (1970) and Wallis & Dobson (1973) did experiments in rectangular ducts, the geometry analysed in this paper, the other experiments were done in round pipes. Authors Lin & Hanratty (1986), Crowley *et al.* (1992) and Andritsos & Hanratty (1987) are the only experimenters to report results for fluids with different viscosities.

It is difficult to compare the results of experiments in round pipes and rectangular channels. The common practice for round pipes is to express results in terms of h/D where D is the pipe diameter and h is the height above the bottom of the pipe; h/H is the liquid fraction in rectangular pipes and $\alpha = 1 - h/H$ is the gas fraction, but h/D is not the liquid fraction in round pipes and $1 - h/D$ is not the gas fraction in round pipes. Lin & Hanratty (1986) presented experimental results for thin liquid films in round pipes giving (their figure 4) h/D vs. $j*$; we converted their results to $j*$ vs. $1 - h/D$ and compared them in figure 11.10 with the results for rectangular pipes. The experimental results for round pipes are much lower than those for rectangular pipes. All this points to the necessity of taking care when comparing results between round and rectangular pipes and interpreting results of analysis for one experiment to another.

In general we do not expect viscous potential flow analysis to work well in two-liquid problems; we get good results only when one of the fluids is a gas so that retarding effects of the second liquid can be neglected. However, the case of Holmboe waves studied by Pouliquen, Chomaz & Huerre (1994) may have a bearing on the two-liquid case. These waves appear only near our critical condition of equal kinematic viscosity. They account for viscosity by replacing the vortex sheet with layers of constant vorticity across which no-slip conditions and the continuity of shear stress are enforced for the basic flow but the disturbance is inviscid. They did not entertain the notion that an inviscid analysis is just what would emerge from the condition of equal kinematic viscosity for viscous potential flow.

11.3.9 Nonlinear effects

None of the theories agree with experiments. Attempts to represent the effects of viscosity are only partial, as in our theory of viscous potential flow, or they require empirical data on wall and interfacial friction, which are not known exactly and may be adjusted to fit the data. Some choices for empirical inputs underpredict and others overpredict the experimental data.

It is widely acknowledged that nonlinear effects at play in the transition from stratified to slug flow are not well understood. The well-known criterion of Taitel & Dukler (1976), based on a heuristic adjustment of the linear inviscid long wave theory for nonlinear effects, is possibly the most accurate predictor of experiments. Their criterion replaces $j* = \alpha^{3/2}$ with $j* = \alpha^{5/2}$. We can obtain the same heuristic adjustment for nonlinear effects on viscous potential flow by multiplying the critical value of velocity in table 11.1 by α. Plots of $j* = \alpha^{3/2}$, $j* = \alpha^{5/2}$ and the heuristic adjustment of viscous potential flow, together with the experimental values of Wallis & Dobson (1973) and Kordyban & Ranov (1970) are shown in figure 11.13. The good agreement in evidence there lacks a convincing foundation.
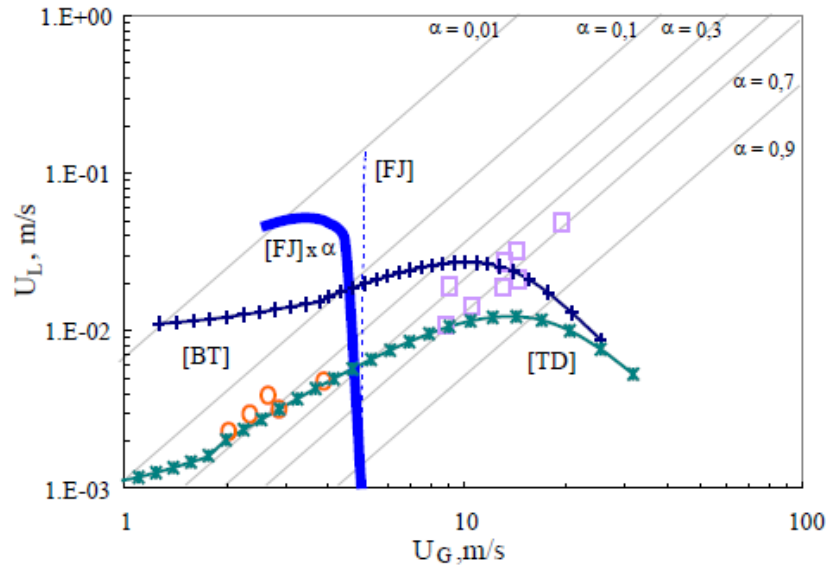
Fig. 11.12. Local liquid velocity U_L versus local gas velocity U_G for PDVSA-Intevep data from 0.508 m i.d. flow loop with air and 0.404 Pa s lube oil. The identified flow patterns are SS (open circles), SW (open squares). Straftified to non-stratified flow transition theories after different authors are compared; TD: stars, BT: +, FJ: broken line, Funada and Joseph multiplied by α (2001) FJ $\times\alpha$ heavy line. Constant void fraction α lines are indicated. Notice that the curves FJ and FJ $\times\alpha$ sharply drop around $U_B 5$ m/s, separating SS data from SW data.

To summarize, we studied Kelvin-Helmholtz stability of superposed uniform streams in rectangular ducts using viscous potential flow. Viscous potential flows satisfy the Navier-Stokes equations. Because the no-slip condition can not be satisfied the effects of shear stresses are neglected, but the effects of extensional stresses at the interface on the normal stresses are fully represented. The solution presented is complete and mathematically rigorous. The effects of shear stresses are neglected at the outset; after that no empirical inputs are introduced. The main result of the analysis is the emergence of a critical value of velocity, discussed in section 11.3.7. The main consequence of this result is that for air-liquid systems the critical values of velocity for liquids with viscosities greater than 15 cp are essentially independent of viscosity and the same as for an inviscid fluid, but for liquids with viscosities less than 15 cp the stability limits are much lower. The criterion for stability of stratified flow given by viscous potential flow is in good agreement with experiments when the liquid layer is thin, but it overpredicts the data when the liquid layer is thick. Though viscous potential flow neglects the effects of shear the qualitative prediction of the peculiar effects of liquid viscosity has been obtained by other authors using other methods of analysis in which shear is not neglected. A rather accurate predictor of experimental results is given by applying the Taitel & Dukler nonlinear correction factor to account for the effect of finite amplitude wave on the results of viscous potential flow.

11.3.10 Combinations of Rayleigh-Taylor and Kelvin-Helmholtz instabilities

Dispersion relations for the combined action of RT and KH instability of irrotational flows of inviscid fluids are presented in the first chapter of the book by Drazin and Reid 1981.

The analysis of the combined action of RT and KH instability can be readily extended to include important effects of viscosity in irrotational flows by techniques explained in Chapter 9 and 11. Updating the potential flow analysis of the dispersion relation to include effects of viscosity using VPF is very easily done and the results are only marginally more complicated than those given by the inviscid analysis but with a much richer physical content.

The extension of nonlinear analysis based on potential flow of inviscid fluids can also be extended to find the irrotational effects of viscosity. The combination of the two instabilities is ubiquitous in nonlinear problems. Joseph, Liao and Saut (1992) considered the KH mechanism for side branching in the displacement of light with heavy fluid under gravity. They showed that the strongest Hadamard instabilities occur as KH instabilities
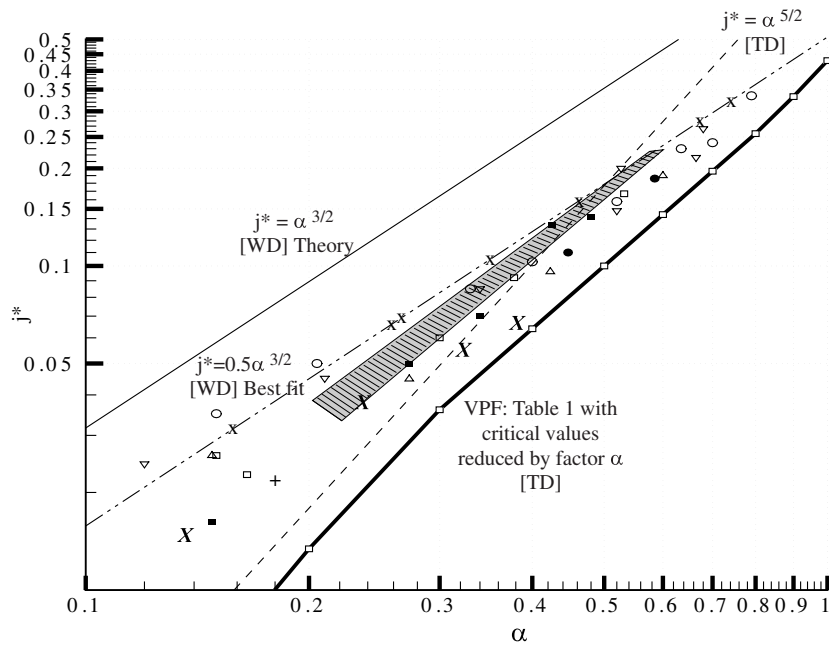
96

Fig. 11.13. Nonlinear effects. The Taitel-Dukler 1976 correction (multiply by α).
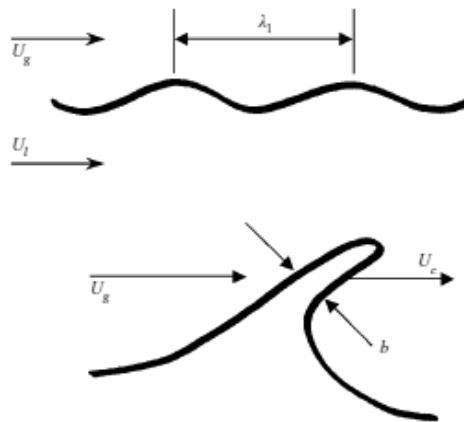
Fig. 11.14. (Varga *et al.* 2003) Schematic of the development of the liquid jet breakup process.

associated with a velocity difference at the sides of falling fingers. The Hadamard instabilities will be regularized by adding irrotational effects of viscosity and surface tension.

Another example of combined KH-RT instability goes in another way. Instead of generating a secondary KH instability on a primary RT instability generated by falling fingers, a secondary RT instability can develop on a primary KH instability in a small-diameter liquid jet exposed to a large-diameter high-speed gas jet studied by Varga, Lasheras and Hopfinger 2003. They proposed a breakup model based on the acceleration mechanism which breakup liquid drops in a high speed air stream studied in chapter 9. In their model, the RT instability is generated on the wave crests generated by a primary KH instability, as is shown in figures 11.14-11.17.

Varga *et al.* 2003 show that the mean droplet sizes scale well on the most unstable RT wavelength. The dependence of the droplet diameter on both the atomizing gas velocity and the liquid surface tension are successfully captured by the proposed breakup model.
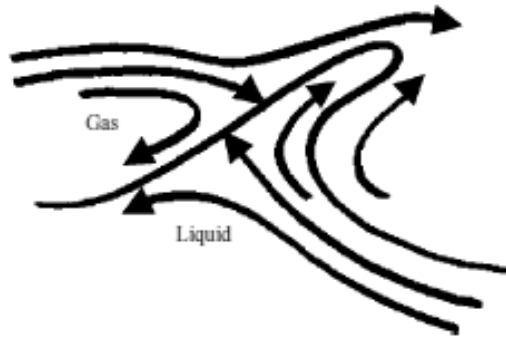
Fig. 11.15. (Varga *et al.* 2003) Sketch of the gas and liquid streamlines in the liquid tongue formation process.
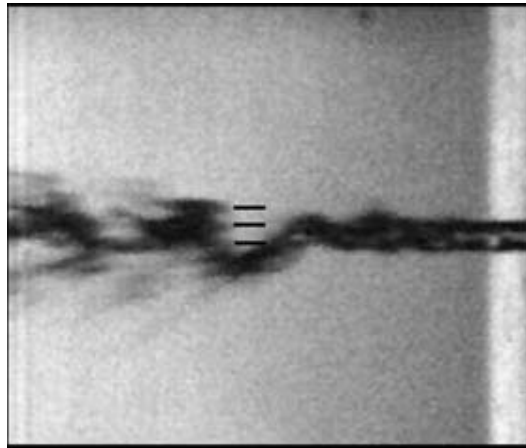
Fig. 11.16. (Varga *et al.* 2003) Instantaneous flow image with identified Rayleigh-Taylor wavelengths, D_l =0.32 mm, We =37, $\lambda_{\text{measured}} = 200\mu$m. (cf. figures 9.6-9.8)
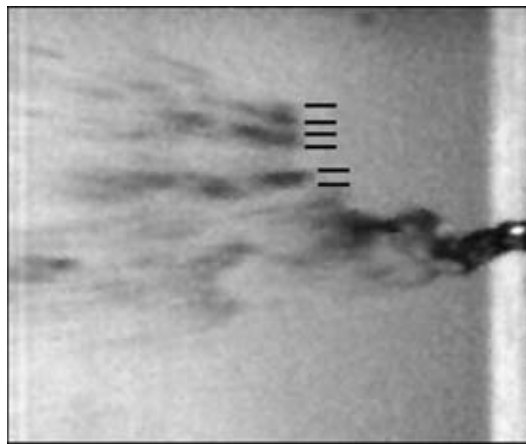
Fig. 11.17. (Varga *et al.* 2003) Instantaneous flow image with identified Rayleigh-Taylor wavelengths, D_l =0.32 mm, We =47, $\lambda_{\text{measured}} = 185\mu$m. (cf. Figs. 9.6-9.8)

12

Energy equation for irrotational theories of gas-liquid flow: viscous potential flow (VPF), viscous potential flow with pressure correction (VCVPF), dissipation method (DM)

12.1 Viscous potential flow (VPF)

The effects of viscosity on the irrotational motions of spherical cap bubble, Taylor bubbles in round tubes, Rayleigh-Taylor and Kelvin-Helmholtz instability described in previous chapters were obtained by evaluating the viscous normal stress on potential flow. In gas-liquid flows, the viscous normal stress does not vanish and it can be evaluated on the potential. It can be said that in the case of gas-liquid flow, the appropriate formulation of the irrotational problem is the same as the conventional one for inviscid fluids with the caveat that the viscous normal stress is included in the normal stress balance. This formulation of viscous potential flow is not at all subtle; it is the natural and obvious way to express the equations of balance when the flow is irrotational and the fluid viscous.

We shall use the acronym VPF, viscous potential flow, to stand for the irrotational theory in which the viscous normal stresses are evaluated on the potential.

In gas-liquid flows we may assume that the shear stress in the gas is negligible so that no condition need be enforced on the tangential velocity at the free surface, but the shear stress must be zero. The condition that the shear stress is zero at each point on the free surface is dropped in the irrotational approximations. In general, you get an irrotational shear stress from the irrotational analysis. The discrepancy between this shear stress and the zero shear stress required for exact solutions will generate a vorticity layer. In many cases this layer is thin and its influence on the bulk motion and on the irrotational effects of viscosity is minor. Exact solutions cannot be the same as any irrotational approximation for cases in which the irrotational shear stress does not vanish.

12.2 Dissipation method according to Lamb

Another purely irrotational theory of flow of viscous fluids is associated with the dissipation method. The acronym DM is used for the dissipation method. The DM extracts information from evaluating the equation governing the evolution of energy and dissipation on irrotational flow. VPF does not rely on arguments about energy and dissipation and the results of the two irrotational theories, DM and VPF, are usually different.

The dissipation method was used by Lamb (1932) to compute the decay of irrotational waves due to viscosity. This method can be traced back to Stokes (1851). A pressure correction was not introduced in these studies. Lamb presented some exact solutions from which the irrotational approximation can be evaluated and the nature of the boundary layer rigorously examined. Lamb (1932) studied the viscous decay of free oscillatory waves on deep water § 348 and small oscillations of a mass of liquid about the spherical form § 355, using the dissipation method. Lamb showed that in these cases the rate of dissipation can be calculated with sufficient accuracy by regarding the motion as irrotational.

Lamb's (1932) calculations are based on the assumption that the speed of a progressive wave is the same as in an inviscid fluid. Padrino (Padrino and Joseph 2006, §14.2.4 and 14.3.1) noticed that a more complete calculation of the dissipation method yields a different result; the growth rates are the same as in Lamb's calculation but the speed of the wave depends on the viscosity of the liquid.

12.3 Drag on a spherical gas bubble calculated from the viscous dissipation of an irrotational flow

The computation of the drag D on a sphere in potential flow using the dissipation method seems to have been given first by Bateman in 1932 (see Dryden, Murnaghan, and Bateman 1956) and repeated by Ackeret (1952). They found that $D = 12\pi a\mu U$ where μ is the viscosity, a radius of the sphere and U its velocity. This drag is twice the Stokes drag and is in better agreement with the measured drag for Reynolds numbers in excess of about 8.

The drag on a spherical gas bubble of radius a rising in a viscous liquid at modestly high Reynolds numbers was calculated, using the dissipation method by various investigators beginning with Levich (1949), who obtained the value $12\pi a\mu U$ or equivalently the drag coefficient $48/R$, where $R = 2aU\rho/\mu$ is the Reynolds number, by calculating the dissipation of the irrotational flow around the bubble. Moore (1959) calculated the drag directly by integrating the pressure and viscous normal stress of the potential flow and neglecting the viscous shear stress (which physically should be zero), obtaining the value $8\pi a\mu U$.

12.4 The idea of a pressure correction

The discrepancy between the two drag values led G. K. Batchelor, as reported by Moore (1963), to suggest the idea discrepancy could be resolved by introducing a viscous correction to the irrotational pressure. We do not know whether we should praise or blame Batchelor for this idea since it comes to us second hand. There is no doubt that the pressure in the liquid depends on the viscosity and it could take on its largest values in boundary layer next to the free surface but the velocity there could also come to depend on the viscosity. Moore (1963) performed a boundary layer analysis and his pressure correction is readily obtained by setting $y = 0$ in his equation (2.37):

$$p_v = (4/R)\left(1 - \cos\theta\right)^2\left(2 + \cos\theta\right)/\sin^2\theta \tag{12.4.1}$$

which is singular at the separation point where $\theta = \pi$. The presence of separation is a problem for the application of boundary layers to the calculation of drag on solid bodies. To find the drag coefficient Moore (1963) calculated the momentum defect, and obtained the Levich value $48/R$ plus contributions of order $R^{-3/2}$ or lower.

Kang & Leal (1988a, b) put the shear stress of the potential flow on the bubble surface to zero and calculated a pressure correction. They obtained the drag coefficient given by Levich's dissipation approximation by direct integration of the normal viscous stress and pressure over the bubble surface. They accomplished this by expanding the pressure correction as a spherical harmonic series and noting that only one term of this series contributes to the drag, no appeal to the boundary-layer approximation being necessary. A similar result was obtained by Joseph & Wang (2004a) using their theory described below, for computing a pressure correction.

The accepted idea, starting with Batchelor, is that the pressure correction is a real viscous pressure which varies from the pressure in the irrotational flow outside a narrow vorticity layer near the gas-liquid surface, to the required value at the interface. This boundary layer has not been computed. Maybe the idea is not quite correct. In the case of the decay of free irrotational gravity waves computed by Lamb (1932), a viscous pressure correction does not appear. The pressure correction computed by Wang & Joseph (2006d) as shown in §14.1 gives the same result as the dissipation method and is in excellent agreement with the exact solution but it is not a viscous correction in a boundary layer of the exact solution.

12.5 Energy equation for irrotational flow of a viscous fluid

Consider the equations of motion for an incompressible Newtonian fluid with gravity as a body force per unit mass

$$\rho\frac{\mathrm{d}\mathbf{u}}{\mathrm{d}t} = -\nabla\Phi + \mu\nabla^2\mathbf{u} \tag{12.5.1}$$

where

$$\Phi = p + \rho g z. \tag{12.5.2}$$

The stress is given by

$$\mathbf{T} = -p\mathbf{1} + \boldsymbol{\tau} \tag{12.5.3}$$

100

where

$$\boldsymbol{\tau} = 2\mu \mathbf{D}[\mathbf{u}]$$

and

$$\nabla \cdot \boldsymbol{\tau} = \mu \nabla^2 \mathbf{u}$$

The mechanical energy equation corresponding to (12.5.1) is given by

$$\frac{\mathrm{d}}{\mathrm{d}t} \int_\Omega \frac{\rho}{2} |\mathbf{u}|^2 \ \mathrm{d}\Omega = \int_S \mathbf{n} \cdot \tilde{\mathbf{T}} \cdot \mathbf{u} \mathrm{d}S - 2\mu \int_\Omega \mathbf{D} : \mathbf{D} \ \mathrm{d}\Omega, \tag{12.5.4}$$

where S is the boundary of Ω, with outward normal $\mathbf{n}$. On solid boundaries no-slip is imposed; say $\mathbf{u} = 0$ there, and on the free surface

$$z = \eta(x, y, t)$$

and the shear stress

$$\mathbf{n} \cdot \mathbf{T} \cdot \mathbf{e}_\mathrm{s} = 0, \tag{12.5.5}$$

where $\mathbf{e}_s$ is any vector tangent to the free surface S_f. On S_f we have

$$\int_S \mathbf{n} \cdot \tilde{\mathbf{T}} \cdot \mathbf{u} \mathrm{d}S = \int_{S_f} \mathbf{n} \cdot \tilde{\mathbf{T}} \cdot \mathbf{u} \mathrm{d}S$$

where

$$\tilde{\mathbf{T}} = \mathbf{T} - \rho g \eta \mathbf{1}, \tag{12.5.6}$$

$$\mathbf{n} \cdot \mathbf{T} \cdot \mathbf{n} = -\gamma \nabla_\mathrm{II} \cdot \mathbf{n}. \tag{12.5.7}$$

Hence, on S_f

$$\mathbf{n} \cdot \tilde{\mathbf{T}} \cdot \mathbf{n} = -\rho g \eta - \gamma \nabla_\mathrm{II} \cdot \mathbf{n}. \tag{12.5.8}$$

and, since the shear stress vanishes on S_f

$$\begin{aligned} \mathbf{n} \cdot \tilde{\mathbf{T}} \cdot \mathbf{u} &= \mathbf{n} \cdot \tilde{\mathbf{T}} \cdot (u_\mathrm{n}\mathbf{n} + u_\mathrm{s}\mathbf{e}_\mathrm{s}) \\ &= -(\rho g \eta + \gamma \nabla_\mathrm{II} \cdot \mathbf{n}) u_\mathrm{n}. \end{aligned} \tag{12.5.9}$$

Hence, (12.5.4) may be written as

$$\frac{\mathrm{d}}{\mathrm{d}t} \int_\Omega \frac{\rho}{2} |\mathbf{u}|^2 \ \mathrm{d}\Omega = - \int_{S_\mathrm{f}} (\rho g \eta + \gamma \nabla_\mathrm{II} \cdot \mathbf{n}) u_\mathrm{n} \mathrm{d}S_\mathrm{f} - 2\mu \int_\Omega \mathbf{D} : \mathbf{D} \ \mathrm{d}\Omega, \tag{12.5.10}$$

Equation (12.5.10) holds for viscous fluids satisfying the Navier–Stokes equations (12.5.1) subject to the vanishing shear stress condition (12.5.5).

We turn now to potential flow $\mathbf{u} = \nabla\phi$, $\nabla^2\phi = 0$. In this case, $\nabla^2\mathbf{u} = 0$ but the dissipation does not vanish. How can this be? In Chapter 4 we showed that the irrotational viscous stress is self-equilibrated and does give rise to a force density term $\nabla^2\nabla\phi = 0$; however, the power of self-equilibrated irrotational viscous stresses

$$\int_{S_\mathrm{f}} \mathbf{n} \cdot 2\mu \nabla \otimes \nabla\phi \cdot \mathbf{u} \mathrm{d}S_\mathrm{f}$$

does not vanish, and it gives rise to an irrotational viscous dissipation

$$\begin{aligned} 2\mu \int_\Omega \mathbf{D}[\mathbf{u}] : \mathbf{D}[\mathbf{u}] \mathrm{d}\Omega &= 2\mu \int_\Omega \frac{\partial^2\phi}{\partial x_\mathrm{i} \partial x_\mathrm{j}} \frac{\partial^2\phi}{\partial x_\mathrm{i} \partial x_\mathrm{j}} \mathrm{d}\Omega = 2\mu \int_S n_\mathrm{j} \frac{\partial^2\phi}{\partial x_\mathrm{j} \partial x_\mathrm{i}} u_\mathrm{i} \mathrm{d}S \\ &= 2\mu \int_{S_\mathrm{f}} \mathbf{n} \cdot \mathbf{D}[\nabla\phi] \cdot \mathbf{u} \mathrm{d}S_\mathrm{f} = 2\mu \int_{S_\mathrm{f}} \mathbf{n} \cdot \mathbf{D} \cdot (u_\mathrm{n}\mathbf{n} + u_\mathrm{s}\mathbf{e}_\mathrm{s}) \ \mathrm{d}S_\mathrm{f} \\ &= \int_{S_\mathrm{f}} \left(2\mu \frac{\partial^2\phi}{\partial n^2} u_\mathrm{n} + \tau_\mathrm{s} u_\mathrm{s} \right) \mathrm{d}S_\mathrm{f} \end{aligned} \tag{12.5.11}$$

where τ_s is an irrotational shear stress

$$\tau_s = 2\mu\mathbf{n}\cdot\mathbf{D}[\nabla\phi]\cdot\mathbf{e}_\mathrm{s},$$
$$u_\mathrm{s} = \mathbf{u}\cdot\mathbf{e}_\mathrm{s}. \tag{12.5.12}$$

Turning next to the inertial terms, we have

$$(\mathbf{u}\cdot\nabla)\mathbf{u} = \nabla\frac{|\mathbf{u}|^2}{2}$$

and

$$
\begin{aligned}
\frac{\mathrm{d}}{\mathrm{d}t}\int_\Omega \frac{\rho}{2}|\mathbf{u}|^2\mathrm{d}\Omega &= \int_\Omega \rho\left(\mathbf{u}\cdot\frac{\partial\mathbf{u}}{\partial t} + \mathbf{u}\cdot\nabla\frac{|\mathbf{u}|^2}{2}\right)\mathrm{d}\Omega \\
&= \int_\Omega \rho\left[\frac{\partial\phi}{\partial x_\mathrm{i}}\frac{\partial}{\partial x_\mathrm{i}}\frac{\partial\phi}{\partial t} + \nabla\cdot\left(\mathbf{u}\frac{|\mathbf{u}|^2}{2}\right)\right]\mathrm{d}\Omega \\
&= \int_{S_\mathrm{f}} \rho u_\mathrm{n}\left(\frac{\partial\phi}{\partial t} + \frac{|\nabla\phi|^2}{2}\right)\mathrm{d}S_\mathrm{f}
\end{aligned}
\tag{12.5.13}
$$

Collecting the results (12.5.9), (12.5.11), (12.5.12) and (12.5.13) we need to evaluate the energy equation (12.5.4) for (12.5.1) when $\mathbf{u} = \nabla\phi$; we find that

$$\int_{S_\mathrm{f}} u_\mathrm{n}\left[\rho\left(\frac{\partial\phi}{\partial t} + \frac{|\nabla\phi|^2}{2} + g\eta\right) + 2\mu\frac{\partial^2\phi}{\partial n^2} + \gamma\nabla_\mathrm{II}\cdot\mathbf{n}\right]\mathrm{d}S_\mathrm{f} = -\int_{S_\mathrm{f}} \tau_\mathrm{s}u_\mathrm{s}\mathrm{d}S_\mathrm{f}. \tag{12.5.14}$$

Equation (12.5.14) was derived by Joseph; it is the energy equation for the irrotational flow of a viscous fluid. As in the case of the radial motion of a spherical gas bubble (6.0.8), the normal stress balance converts into the energy equation for viscous irrotational flow.

12.6 Viscous correction of viscous potential flow

The viscous pressure p_v for VCVPF can be defined by the equation

$$\int_{S_\mathrm{f}} (-p_\mathrm{v})u_\mathrm{n}\mathrm{d}S_\mathrm{f} = \int_{S_\mathrm{f}} \tau_\mathrm{s}u_\mathrm{s}\mathrm{d}S_\mathrm{f}. \tag{12.6.1}$$

This equation can be said to arise from the condition that the shear stress should vanish but it does not vanish in the irrotational approximation. Batchelor's idea, as reported by Moore (1963), is that the additional drag $4\pi a\mu U$ on a spherical gas-bubble needed to obtain the Levich drag $12\pi a\mu U$ from the value $8\pi a\mu U$, computed using the viscous normal stress, arises from a real viscous pressure in a thin boundary layer at the surface of the bubble.

Our interpretation of Batchelor's idea is to replace the unwanted shear stress term in the energy equation with an additional contribution to the normal stress in the form of a viscous pressure satisfying (12.6.1). An identical interpretation of Batchelor's idea, with a different implementation, has been proposed by Kang and Leal (1988b) and is discussed in §13.1.1.

Suppose now that there is such a pressure correction and Bernoulli equation

$$p_\mathrm{i} + \rho\left(\frac{\partial\phi}{\partial t} + \frac{|\nabla\phi|^2}{2} + g\eta\right) = C$$

holds. Since

$$C\int_S \mathbf{u}\cdot\mathbf{n}\mathrm{d}S = C\int_\Omega \nabla\cdot\mathbf{u}\mathrm{d}\Omega = 0$$

we obtain

$$\int_{S_\mathrm{f}} u_\mathrm{n}\left[-p_\mathrm{i} - p_\mathrm{v} + 2\mu\frac{\partial^2\phi}{\partial n^2} + \gamma\nabla_\mathrm{II}\cdot\mathbf{n}\right]\mathrm{d}S_\mathrm{f} = 0 \tag{12.6.2}$$

The normal stress balance for VCVPF is

$$-p_\mathrm{i} - p_\mathrm{v} + 2\mu\frac{\partial^2\phi}{\partial n^2} + \gamma\nabla_\mathrm{II}\cdot\mathbf{n} = 0 \tag{12.6.3}$$

Equation (12.6.3) is a working equation in the VCVPF theory only if p_v can be calculated. In the problems discussed in this book, p_v and a velocity correction $\mathbf{u}_v$ are coupled in a linear equation

$$\rho\frac{\partial \mathbf{u}_v}{\partial t} = -\nabla p_v + \mu\nabla^2 \mathbf{u}_v, \qquad \nabla \cdot \mathbf{u}_v = 0, \tag{12.6.4}$$

and since $\mathbf{u}_v$ is harmonic $\nabla^2 p_v = 0$ and p_v can be represented by a series of harmonics functions. In most of the problems in this book, orthogonality conditions show that all the terms in the series but one are zero and this one term is completely determined by (12.6.1). In other problems, such as the flow over bodies studied in Chapter 13, (12.6.1) determines the coefficient of the term in the harmonic series that enters into the direct calculation of the drag; the other coefficients remain undetermined.

Having obtained p_v it is necessary to consider the problem (12.6.4) for $\mathbf{u}_v$. This problem is overdetermined; (12.6.4) is a system of four equations for three unknowns. We must also satisfy the kinematic equation $\mathbf{u}_v = \partial\eta_v/\partial t$ and the normal stress boundary condition. Wang and Joseph (2006d) showed that a purely irrotational $\mathbf{u}_v$ and higher order corrections satisfaying (12.6.1) can be computed in the case in which the normal stress bpundary condition is not corrected. Their solution procedure leads to a series of purely irrotational velocities in powers of ν, or reciprocal powers of the Reynolds number (see §14.12). This same kind of special irrotational solution in reciprocal powers of the Reynolds number was constructed by Funada et al (2005) for capillary instability of a viscous fluid and by Wang et al (2005b) for a capillary instability of a viscoelastic fluid.

There is no reason to think that the higher order irrotational solutions generated by p_v have a hydrodynamical significance. In general, the solution of potential flow problems with pressure corrections can be expected to induce vorticity. This is the case for the nonlinear model of capillary collapse and rupture studied in §17.4.2. The flow from irrotational stagnation points of depletion to irrotational stagnation points of accumulation cannot occur without generating the vorticity given by (17.4.24) at leading order.

In the direct applications of the dissipation method, a pressure correction is not introduced; the power of the irrotational shear stress on the right side of (12.5.14) is computed directly. The energy equation for the system of VCVPF equations with p_v is the same as (12.5.14) when the power of p_v is replaced by the power of the shear stress using (12.6.1).

In the case of rising bubbles we may compute the same value for the drag in a direct computation in which the irrotational shear stress is neglected and p_v is included as we get from the dissipation method using (12.5.14) with $\tau_s \neq 0$ and $p_v = 0$.

The dissipation method requires that we work with the power generated by the shear $u_s\tau_s$ and not with a direct computation using p_v. The direct computation of drag with $p_v = 0$ and $\tau_s \neq 0$ given by potential flow leads to zero drag (13.1.8). The pressure correction allows us to do direct calculations without using the energy equations. The two methods lead to the same results by different routes. This feature of energy analysis is related to the fact that irrotational stresses are self-equilibrated (4.3.1) but do work.

The nature of the construction of VCVPF equations, which have the same energy equations as those used in the dissipation method, guarantees that the same results will be obtained by these two methods.

The VCVPF theory is perhaps artificial in some cases, like the decay of gravity waves in which no viscous pressure appears in the exact solution (see §14.1.3). However, in all cases, VCVPF leads to the same results as the dissipation method.

We have now arrived at the following classification of irrotational solutions:

IPF - inviscid potential flow

VPF - viscous potential flow

VCVPF - viscous correction of viscous potential flow

DM - dissipation method

Recognizing now that DM and VCVPF lead to the same results by different routes, even if p_v is not a true hydrodynamic pressure, we can introduce yet another acronym

VCVPF/DM

and

ES - exact solution.

VCVPF/DM and VPF are different irrotational solutions; they give rise to different results in nearly every instance except in the case of the limit of very high Reynolds numbers where they tend to the inviscid limit IPF. At finite Reynolds number VPF and VCVPF/DM can give significantly better results, closer to the exact solutions than IPF.

In the sequel, VCVPF means VCVPF/DM. We think that it is possible that either VPF or VCVPF give (in different situations which we presently cannot specify *a priori* with precision) the best possible purely irrotational approximations to the exact solution. The problem of the best purely irrotational approximation of real flows is related to the problem of the optimal specification of the irrotational flow in the Helmholtz decomposition studied in Chapter 4.